



저작자표시-비영리-동일조건변경허락 2.0 대한민국

이용자는 아래의 조건을 따르는 경우에 한하여 자유롭게

- 이 저작물을 복제, 배포, 전송, 전시, 공연 및 방송할 수 있습니다.
- 이차적 저작물을 작성할 수 있습니다.

다음과 같은 조건을 따라야 합니다:



저작자표시. 귀하는 원저작자를 표시하여야 합니다.



비영리. 귀하는 이 저작물을 영리 목적으로 이용할 수 없습니다.



동일조건변경허락. 귀하가 이 저작물을 개작, 변형 또는 가공했을 경우에는, 이 저작물과 동일한 이용허락조건하에서만 배포할 수 있습니다.

- 귀하는, 이 저작물의 재이용이나 배포의 경우, 이 저작물에 적용된 이용허락조건을 명확하게 나타내어야 합니다.
- 저작권자로부터 별도의 허가를 받으면 이러한 조건들은 적용되지 않습니다.

저작권법에 따른 이용자의 권리는 위의 내용에 의하여 영향을 받지 않습니다.

이것은 [이용허락규약\(Legal Code\)](#)을 이해하기 쉽게 요약한 것입니다.

[Disclaimer](#)

공학박사 학위논문

Reversal Dynamics of Magnetic Vortex Core in Soft Magnetic Nanoelements

연자성 나노물질에서의 자기소용돌이 핵의
자화 반전 연구

2015 년 2 월

서울대학교 대학원

재료공학부

유 명 우

Reversal Dynamics of Magnetic Vortex Core in Soft Magnetic Nanoelements

A THESIS

**SUBMITTED TO THE FACULTY OF SEOUL
NATIONAL UNIVERSITY**

BY

Myoung-Woo Yoo

Supervised by

Prof. Sang-Koog Kim

**IN PARTIAL FULFILLMENT OF THE
REQUIREMENTS FOR THE DEGREE OF
DOCTOR OF PHILOSOPHY**

January 2015

Department of Materials Science and Engineering

Graduate School

Seoul National University

Abstract

This thesis addresses dynamics of ultrafast magnetic vortex core switching (≤ 1 ns) in soft magnetic nanoelements by micromagnetic simulations. To find more efficient way to reverse the core magnetization, we used the radial and azimuthal spin-wave modes in thin magnetic nanodisks. We also examined the core switching in three-dimensional magnetic half-spheres.

First, we observed the radial spin-wave mode driven vortex core reversals using oscillating magnetic fields applied perpendicularly to the disk plane. It was found that when the field frequencies are tuned to the eigenfrequencies of radial spin-wave modes of the vortex structure, the threshold field amplitudes required for vortex-core switching are an order of magnitude smaller than those of static perpendicular fields within 1 ns. The reversal mechanism and associated underlying physics are completely different from well-known vortex-antivortex-pair-mediated core reversals.

Next, we also examined the azimuthal spin-wave modes driven vortex-core switching in soft magnetic nano-disks. We addressed the similarities and differences between the asymmetric core reversals in terms of the temporal evolutions of the correlated core-motion speed, locally concentrated perpendicular gyrofield, and magnetization dip near the original vortex core. The core-motion speed and the associated perpendicular gyrofield must reach their threshold values to meet the ultimate core-reversal criterion $m_{z,\text{dip}} \sim -p$, where p is the polarization of the given vortex state. Also, we

determined the perpendicularly bias field strength and direction dependence of the core-switching time and threshold exciting field strength required for the core reversals, which parameters are essential in the application aspect.

Finally, we studied the magnetization-reversal dynamics of soft magnetic half-spheres with vertically non-uniform vortex cores, and found a heretofore-unknown mechanism of vortex-core reversals in cylindrical dots. In the half-sphere geometry, another vortex core, the magnetization of which is opposite to the original core, is formed at the edge of the half-sphere after expulsion of the original core, thereby reversing the core. Core switching occurs either with or without chirality switching. The specific curved three-dimensional geometry of half-spheres can affect the core-reversal mechanisms.

The present studies offer deeper insights into the core switching dynamics as well as imparts further momentum to the realization of information storages based on the vortex structure and its dynamic properties.

Keywords: Magnetism, Spin Dynamics, Magnetic Vortex, Vortex Core Switching

Student Number: 2008-22853

Contents

Chapter 1 Introduction	1
References	8
Chapter 2 Research Background	11
2.1. Magnetic Vortex	11
2.1.1. Magnetic Vortex State	11
2.1.2. Eigenmodes in the Magnetic Vortex	12
2.2. Vector Network Analyzer (VNA)	17
2.2.1. VNA-FMR Measurement	17
2.2.2. Reflection VNA-FMR technique	17
2.2.3. Transmission VNA-FMR technique	18
2.3. Numerical Calculations for Spin Dynamics	21
2.3.1. Micromagnetics	21
2.3.2. Micromagnetic Simulations	28
References	32
Chapter 3 Spin-wave Modes in the Magnetic Vortex State	35
3.1. Introduction	35
3.2. Methods	37
3.2.1. Experimental Method	37
3.2.2. Micromagnetic Simulation Method	37
3.3. Results and Discussion	41

Appendix	45
References	48
Chapter 4 Radial Mode Driven Core Switching in Nanodisks	50
4.1. Introduction	50
4.2. Modeling	51
4.3. Results and Discussion	52
4.3.1. Eigenfrequencies of the Radial Spin-wave Modes	52
4.3.2. Radial Spin-wave Mode Driven Vortex Core Switching	55
4.3.3. Threshold Field and Switching Time	61
References	64
Chapter 5 Azimuthal Mode Driven Core Switching in Nanodisks	66
5.1. Introduction	66
5.2. Modeling	68
5.3. Results and Discussion	70
5.3.1. Azimuthal-mode-driven core reversals	70
5.3.2. Control of core reversals by perpendicular bias field	80
References	91
Chapter 6 Vortex Core Switching in Magnetic Half-spheres	94
6.1. Introduction	94
6.2. Modeling	96
6.3. Results and Discussion	98
6.3.1. Eigenmodes in a Magnetic Half-spheres	98

6.3.2. Gyrotropic Mode Driven Vortex Core Switching	109
References	120
Chapter 7 Summary	123
Publication List	
Presentations in Conferences	
Abstract in Korean	

List of Tables

2.1. Table of material parameters of permalloy (Py).....	31
--	----

List of Figures

1.1. Direct experimental observations of magnetic vortex structures	5
1.2. Schematic of the magnetic vortex core	5
1.3. Magnetic configurations of energetically equivalent vortex-states	6
1.4. Stable magnetic vortex configurations	7
2.1. In-plane and out-of-plane single domain – vortex boundary	16
2.2. Schematics of the gyrotropic and the radial and azimuthal modes	16
2.3. Schematic of the VNA-FMR setup	20
2.4. Schematic of magnetization precession motion	29
2.5. Advantages and disadvantages of FDM and FEM	30
3.1. Photograph of the experimental setup of the probe station	39
3.2. Schematic of the VNA-FMR setup	40
3.3. Frequency Spectra obtained from the VNA-FMR measurement	43
3.4. Plane view images of spatial distributions of FFT power	44
3.5. Arrays of a permalloy nanodisk	47
4.1. Radial spin-wave modes	54
4.2. Snapshot images of temporal evolution of $n = 1$ radial mode	59
4.3. Variation of m_z and Temporal variation of each energy density	60
4.4. Phase diagrams of switching events and switching times	63
5.1. Azimuthal spin-wave modes	69
5.2. Trajectories of vortex-core motions	76
5.3. Snapshot images of magnetizations and gyrofield distributions	77
5.4. Temporal variations of core speed, local gyrofield, and $m_{z,dip}$	78

5.5. Perpendicular field effects	79
5.6 Eigenfrequencies of the azimuthal modes as a function of H_z	85
5.7 Vortex-core gyrations driven by the azimuthal modes	86
5.8. Comparison of vortex-core speed v , gyrofield, and $m_{z,\text{dip}}$	87
5.9. The H_z -dependence of the v_{max} and $ h_z _{\text{max}}$ values	88
5.10. Normalized switching time for different H_z values	89
5.11. H_z -dependence of normalized threshold field strength	90
6.1. Half-spheres	104
6.2. Eigenmodes in half-spheres	105
6.3. Snapshot images of vortex-core motions	106
6.4 θ - and δ -dependences of the eigenmodes and eigenfrequencies	107
6.5 Eigenfrequencies of eigenmodes obtained as function of H_z	108
6.6 Model geometry and Snapshot images of vortex-core motion	115
6.7. Trajectories of vortex-core motions	116
6.8. Phase diagram of polarization and chirality switching events	117
6.9. Snapshot images of the vortex-core switching	118
6.10. Snapshot images of the vortex-core switching	119

Chapter 1

Introduction

Spin dynamics in submicron- and nanometer-sized magnetic elements is an important field of research in nanotechnology [1], owing not only to the fundamental interest in it but also to its possible applications in future devices. Some examples of possible applications include high-density nonvolatile memory storage [2-5] and information processors [6, 7]. In confined ferromagnetic nanoelements, intriguing magnetic phenomena have been observed that differ from those in bulk magnetic systems. For example, unique magnetic configurations are formed in patterned thin films, such as the magnetic vortex structure (see Fig. 1.1) in a circular disk [8, 9]. Moreover, these configurations also have nontrivial dynamics, such as the gyrotropic motion of vortex structures [10].

Over the past decade, such magnetic structures in nanoelements, especially magnetic vortex structures in patterned thin films [8, 9], have attracted much attention. The magnetic vortex shows an in-plane curling of the magnetic configuration along the boundary of the element. In addition, similar to other “vortices” in nature such as water vortices, typhoons, superfluids, and superconducting fluxons, the magnetic vortex configuration has an out-of-plane magnetization that is a few tens of nanometers in size, called a vortex core (see Fig. 1.2). The vortex core is located in the center and avoids a singularity. Because there are four energetically equivalent states corresponding to either

counter-clockwise (CCW, chirality $c = +1$) or clockwise (CW, $c = -1$) in-plane curling of the magnetization as well as upward (polarization $p = +1$) or downward ($p = -1$) out-of-plane magnetizations, all of which have high thermal stability (see Fig. 1.3), the magnetic vortex is considered to be one of the most important candidates for future nonvolatile memory elements [3, 11-14]. However, it is recognized that owing to high stability of the vortex states a large amount of energy is required to control the states; a strong static magnetic field ($> \text{few kiloOersteds}$) is required to switch the vortex core orientation.

However, recently, it has been reported that vortex-core reversals in nanodots can be achieved with relatively low-power consumption ($< \sim 100 \text{ Oe}$). Such a reversal can occur when one of the intrinsic eigenmodes, such as the gyrotropic mode [15] or the radial and azimuthal spin-wave modes [16-18], are resonantly excited in a given nanodot. The gyrotropic-mode-resonant excitation can yield robust core reversals, and the mechanisms [15, 19, 20], criteria [21, 22], and physical origins [21, 23] for this are well known. Gyrotropic-mode-driven core reversals occur through the nucleation and annihilation of a vortex and antivortex pair. The reversal criterion is that the normalized out-of-plane magnetization ($m_z = M_z / M_s$) of a magnetization dip near the original vortex core reaches the value of $m_z = -p$ [24, 25]. This dip formation originates from a highly concentrated perpendicular effective field, the so-called gyrofield, which is induced by an in-plane magnetization deformation that increases with the core-motion speed [21, 23].

Contrary to the above gyrotropic-mode-driven vortex core switching,

the fundamentals of the radial- and azimuthal spin-wave-mode-driven core reversals have been relatively less explored [16, 18]. Just a few papers have reported an energy-efficient and relatively fast vortex-core switching mechanism that utilizes in-plane oscillating fields, the frequencies of which are tuned to the eigenfrequencies of the azimuthal spin-wave modes. The frequencies of the azimuthal spin-waves modes (~ 10 GHz) are an order of magnitude higher than for a typical gyrotropic mode (< 1 GHz) [16-18, 24].

Meanwhile, recent developments in advanced nanofabrication technology allows for the fabrication of complicated three-dimensional (3D) nanostructures with a rich variety of shapes, such as thin or thick dots or disks [26, 27], pyramids [28], spheres [29], spherical caps [30], spherical shells [31, 32], and both closed- and rolled-up nanotubes [33]. In such restricted geometries, the competition between dipolar and exchange interactions leads to 3D magnetization configurations that depend on the dimensions and geometry of a given nano-scaled element (see Fig. 1.4). Thus, it is necessary to reveal additional and/or new underlying physics of their static and dynamic properties. These features could not be obtained from 2D based approaches.

In this thesis, we examine three different vortex-core reversal mechanisms. First, we explore the similarities and differences between the asymmetric dynamics of two different azimuthal-mode (Counter clockwise and clockwise modes) driven core reversals. We pay specific attention to the correlations among the magnetization dip criterion, the core-motion speed, and the perpendicular gyrofield. Next, we report on an alternative means of vortex-

core switching that uses oscillating fields applied perpendicularly to the disk plane. The frequency of these perpendicular fields is tuned to the frequency of the radial spin-wave modes. Finally, we investigate another robust core-reversal in 3D magnetic half-sphere particles with and without simple chirality switching in soft magnetic half-spheres. The reversal mechanism is totally different from the well-known vortex-antivortex pair nucleation and annihilation process that occurs in 2D systems.

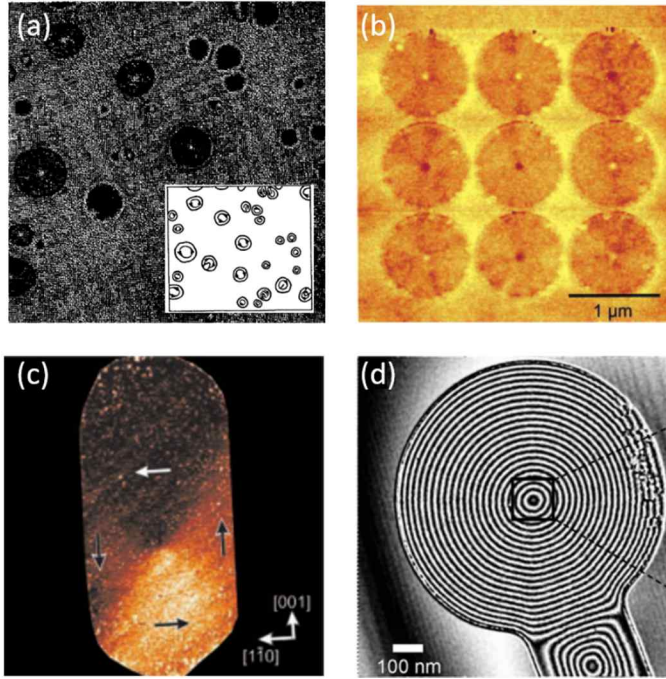


Fig. 1.1. Direct experimental observations of magnetic vortex structures using (a) Lorentz microscopy, (b) magnetic force microscopy (MFM), (c) spin-polarized scanning tunneling microscopy (SP-STM), and (d) electron holography.

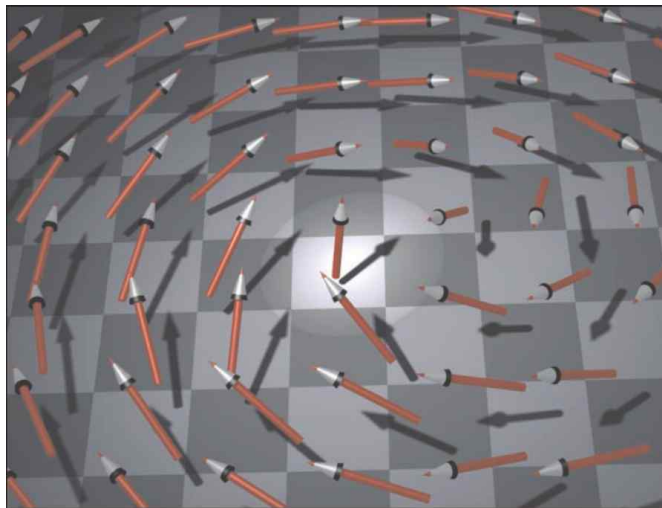


Fig. 1.2. Schematic of the magnetic vortex core. In the center of the core, the magnetization is perpendicular to the plane (highlighted).

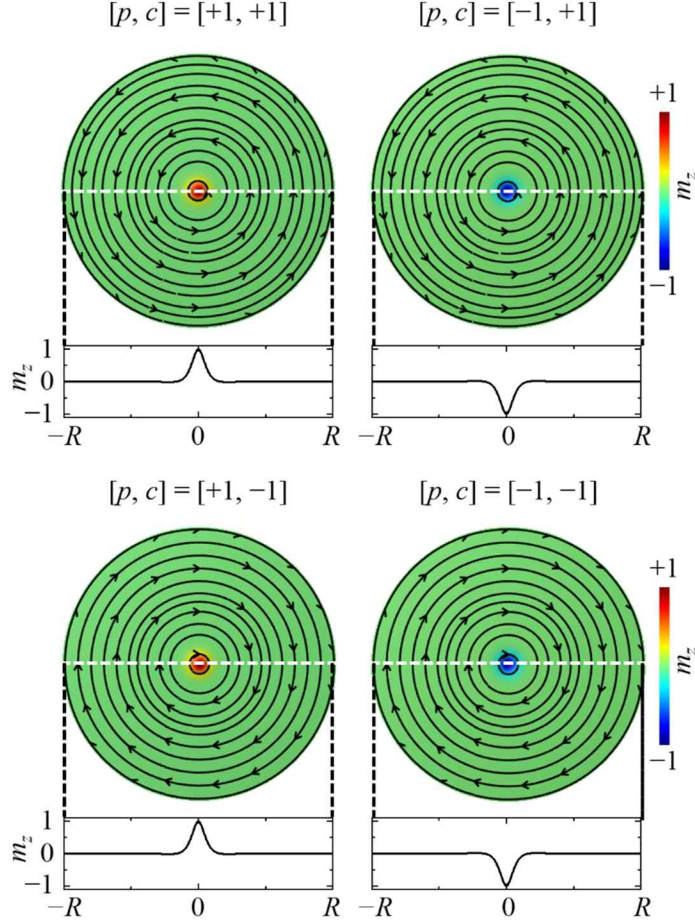


Fig. 1.3. Magnetic configurations of four energetically equivalent vortex-states, $[p, c] = [+1, +1]$, $[-1, +1]$, $[+1, -1]$ and $[-1, -1]$, in permalloy (Py, $\text{Ni}_{80}\text{Fe}_{20}$) magnetic nanodisks with a 300-nm diameter and 20-nm thickness. The in-plane curling magnetization orientations are indicated by the streamlines with the small arrows. Bottom rows of the each state show profiles of the z -component of normalized magnetizations (m_z) crossing the center of the disks.

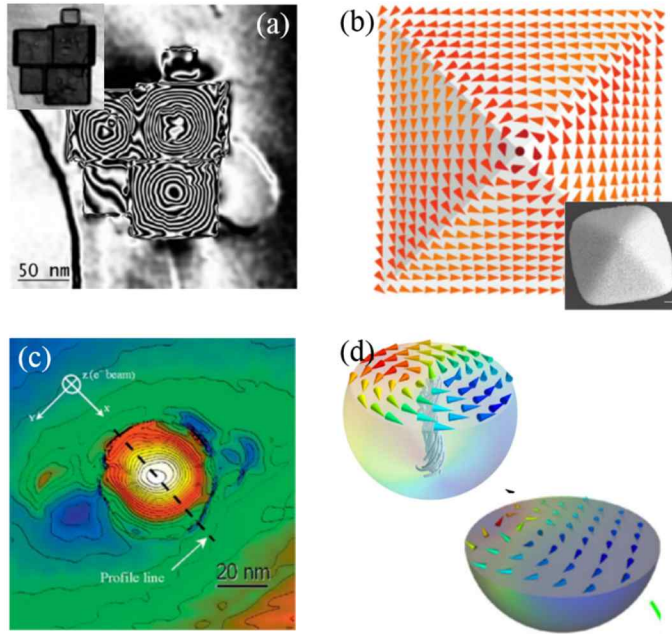


Fig. 1.4. Observed or numerically calculated stable magnetic vortex configurations in various three-dimensional magnetic elements: (a) Cubes, (b) pyramids, (c) spheres, and (d) part-spheres.

References

- [1] A. Hubert and R. Schafer, *Magnetic Domains* (Springer, Berlin, 2000).
- [2] J. C. Slonczewski, *Journal of Magnetism and Magnetic Materials* **159**, L1 (1996).
- [3] J. Thomas, *Nature Nanotechnology* **2**, 206 (2007).
- [4] R. Cowburn and D. Petit, *Nature Materials* **4**, 721 (2005).
- [5] S. S. P. Parkin, M. Hayashi and L. Thomas, *Science* **320**, 190 (2008).
- [6] H. Jung, Y. S. Choi, K. S. Lee, D. S. Han, Y. S. Yu, M. Y. Im, P. Fischer and S. K. Kim, *Acs Nano* **6**, 3712 (2012).
- [7] D. A. Allwood, G. Xiong, C. C. Faulkner, D. Atkinson, D. Petit and R. P. Cowburn, *Science* **309**, 1688 (2005).
- [8] T. Shinjo, T. Okuno, R. Hassdorf, K. Shigeto and T. Ono, *Science* **289**, 930 (2000).
- [9] A. Wachowiak, J. Wiebe, M. Bode, O. Pietzsch, M. Morgenstern and R. Wiesendanger, *Science* **298**, 577 (2002).
- [10] K. Y. Guslienko, B. A. Ivanov, V. Novosad, Y. Otani, H. Shima and K. Fukamichi, *J Appl Phys* **91**, 8037 (2002).
- [11] R. P. Cowburn, *Nature Materials* **6**, 255 (2007).
- [12] S. Bohlens, B. Kruger, A. Drews, M. Bolte, G. Meier and D. Pfannkuche, *Applied Physics Letters* **93**, 142508 (2008).
- [13] S. K. Kim, K. S. Lee, Y. S. Yu and Y. S. Choi, *Applied Physics Letters* **92**, 022509 (2008).
- [14] Y. S. Choi, M. W. Yoo, K. S. Lee, Y. S. Yu, H. Jung and S. K. Kim, *Applied*

Physics Letters **96**, 072507 (2010).

[15] B. Van Waeyenberge, A. Puzic, H. Stoll, K. W. Chou, T. Tyliczszak, R. Hertel, M. Fahnle, H. Bruckl, K. Rott, G. Reiss, I. Neudecker, D. Weiss, C. H. Back and G. Schutz, Nature **444**, 461 (2006).

[16] R. F. Wang and X. W. Dong, Applied Physics Letters **100**, 082402 (2012).

[17] V. P. Kravchuk, D. D. Sheka, Y. Gaididei and F. G. Mertens, J Appl Phys **102**, 043908 (2007).

[18] M. Kammerer, M. Weigand, M. Curcic, M. Noske, M. Sproll, A. Vansteenkiste, B. Van Waeyenberge, H. Stoll, G. Woltersdorf, C. H. Back and G. Schuetz, Nature Communications **2**, 279 (2011).

[19] R. Hertel and C. M. Schneider, Physical Review Letters **97**, 177202 (2006).

[20] K. S. Lee, K. Y. Guslienko, J. Y. Lee and S. K. Kim, Phys Rev B **76**, 174410 (2007).

[21] K. Yamada, S. Kasai, Y. Nakatani, K. Kobayashi, H. Kohno, A. Thiaville and T. Ono, Nature Materials **6**, 269 (2007).

[22] K. S. Lee, S. K. Kim, Y. S. Yu, Y. S. Choi, K. Y. Guslienko, H. Jung and P. Fischer, Physical Review Letters **101**, 267206 (2008).

[23] K. Y. Guslienko, K. S. Lee and S. K. Kim, Physical Review Letters **100**, 027203 (2008).

[24] V. P. Kravchuk, Y. Gaididei and D. D. Sheka, Phys Rev B **80**, 100405 (2009).

[25] M. W. Yoo, K. S. Lee, D. E. Jeong and S. K. Kim, Phys Rev B **82**, 174437 (2010).

- [26] F. Boust and N. Vukadinovic, Phys Rev B **70**, 172408 (2004).
- [27] J. J. Ding, G. N. Kakazei, X. M. Liu, K. Y. Gusliencko and A. O. Adeyeye, Scientific Reports **4**, 4796 (2014).
- [28] A. Knittel, M. Franchin, T. Fischbacher, F. Nasirpour, S. J. Bending and H. Fangohr, New Journal of Physics **12**, 113048 (2010).
- [29] M. Ammar, M. LoBue, E. Snoeck, M. Hytch, Y. Champion, R. Barrue and F. Mazaleyrat, Journal of Magnetism and Magnetic Materials **320**, E716 (2008).
- [30] R. P. Boardman, J. Zimmermann, H. Fangohr, A. A. Zhukov and P. A. J. de Groot, J Appl Phys **97**, 10E305 (2005).
- [31] Q. L. Ye, Y. Kozuka, H. Yoshikawa, K. Awaga, S. Bandow and S. Iijima, Phys Rev B **75**, 224404 (2007).
- [32] R. Streubel, V. P. Kravchuk, D. D. Sheka, D. Makarov, F. Kronast, O. G. Schmidt and Y. Gaididei, Applied Physics Letters **101**, 132419 (2012).
- [33] R. Streubel, J. Lee, D. Makarov, M. Y. Im, D. Karnaushenko, L. Han, R. Schafer, P. Fischer, S. K. Kim and O. G. Schmidt, Advanced Materials **26**, 316 (2014).

Chapter 2

Research Background

2.1. Magnetic Vortex

2.1.1. Magnetic Vortex State

The spin configuration in a ferromagnetic material is determined by the competition between several magnetic energy scales [1]: the exchange energy that results from the Pauli exclusion principle, the magnetostatic energy from the classical dipole-dipole interaction between magnetic moments (the magnetic field energy owing to the magnetic field induced by the magnetic medium itself), the magnetocrystalline anisotropic energy from the spin-orbit interaction, which couples the electron spin system to the lattice and creates orbital magnetism, and additional energies induced by external forces, such as Zeeman energy, which arise from the interactions between the magnetic moments and an external field.

For a soft magnetic nanoelement without any external forces, the spin configurations are determined mainly by the competition between the exchange energy, which favors spins being parallel to their neighbors, and the magnetostatic energy, which favors spins forming a closed structure to prevent free magnetic poles from generating stray magnetic fields outside the nanoelement. In a thin film disk with a sub-micrometer diameter, a thickness of a few tens of nanometers, and the proper aspect ratio between them [2, 3], as shown in Fig. 2.1, the magnetizations are aligned along the circular boundary,

forming an in-plane curling structure around the disk center to avoid a free pole. However, this continuous variation of the in-plane magnetic structure costs exchange energy, which wants variation between adjacent spins. The exchange energy cost increases closer to the disk center. At the disk center, the variation of the magnetization will be infinite and, as a result, the exchange energy will be immeasurable. To avoid this singularity [4, 5], an out-of-plane magnetic structure a few-nm in size develops at the center. This structure is called the vortex core. Due to the stray field from the free poles in the vortex core, the magnetostatic energy is concentrated at the disk center.

2.1.2. Eigenmodes in the Magnetic Vortex

Due to the interactions between magnetic moments in the nanoelements, the magnetic vortex has characteristic eigenmodes in its structure. Understanding the eigenmodes in the magnetic vortex state is of significant fundamental and applied interest because these modes allow for more efficient vortex-core switching [6-9]. The eigenmodes in the magnetic vortex are composed of a relatively low frequency mode (< 1 GHz) [10] and high frequency (~ 10 GHz) azimuthal and radial spin-wave modes [11-13].

A. Gyrotropic Mode (Translational Mode)

The gyrotropic motion of a vortex, in general, can be described by a collective variable theory developed by Thiele [14]. According to the theory, by assuming a magnetic domain is in steady-state motion, the Landau-Lifshitz-

Gilbert (LLG) equation [15], which describes the dynamics of a single magnetic moment, can be transformed into a force balance equation of a solitary magnetic structure, where each term is determined by the initial magnetic configuration and the position vector of the magnetic soliton. Then, Thiele's equation is

$$-\mathbf{G} \times \frac{d\mathbf{X}}{dt} - D \frac{d\mathbf{X}}{dt} - \frac{\partial W}{\partial \mathbf{X}} = 0,$$

where $\mathbf{X} = (X, Y)$ is the position vector of the magnetic soliton. The first term is a gyrotropic force, a Magnus-type force that is perpendicular to the velocity vector of the magnetic soliton. The second term is the damping force. The final term is the restoring force, approximated as the first derivative of the total magnetic energy, W , with respect to the position of the magnetic soliton.

$\mathbf{G} = (0, 0, G)$ and D for magnetic vortex structures have been theoretically estimated for various systems. The first attempt to adopt Thiele's formalism to a magnetic vortex structure was done by D. L. Huber assuming a 3D vortex magnetization in a 2D planar magnetic system. In 2002 and 2006, Guslienko calculated G and D with a simple variational function for the magnetic vortex structure in a cylindrical magnetic disk with a finite thickness and radius [10, 16].

Restoring forces, for a finite structure, are mainly attributed to the magnetostatic interactions induced by the displacement of vortex core from its equilibrium position. The restoring force of a magnetic vortex in a cylindrical disk can be evaluated based on two distinct models that describe the field evolution of the magnetic vortex in the disk: the rigid vortex model [17] and the two-vortex model (side-surface charge free model) [2, 10, 17]. The first

model assumes that the magnetization distribution shifts without a change in their structure. Thus, a magnetic surface charge is induced on the sides of the cylinder. This surface charge is the main contributor of the magnetostatic interaction energy. This model is adequate for describing a static magnetic vortex. In contrast, the two-vortex model assumes a deformation of the magnetization as it shifts from the center of the disk. This deformation avoids the generation of any magnetic surface charge. Then, the magnetostatic interaction is attributed to the magnetic volume charge. This model is more realistic for the dynamic problem than the rigid vortex model.

B. Radial and Azimuthal Spin-wave Modes

The radial and azimuthal modes generate relatively high frequency (~ 10 GHz) spin-waves in circular disks. These spin-wave modes were first reported by Novosad *et al.*[11], and then Buess *et al.*[18] more precisely explored the related dynamics. The spin-wave modes are mostly determined by the dipolar interactions between the magnetizations. The eigenfrequencies of these modes are proportional to the aspect ratio $(L/R)^{1/2}$ for thin soft ferromagnetic disks, such as Py [11, 13, 18].

To theoretically investigate the problem, an ansatz were formulated for spatially and temporally varying magnetization as $m(\rho, t) = m_0(\rho) + \mu(\rho, t)$, where m is a normalized magnetization and ρ is distance from the center of a given disk [8, 13]. The spin-wave modes can be labeled by the number of nodes, n and m along the radial and the azimuthal directions, respectively. For

a fixed n , a splitting of the azimuthal modes occurs for m values with the same absolute value but different sign. The sign denotes the direction of rotation of the dynamical magnetization. For the upward core ($p = +1$), $(-)$ and $(+)$ signs represent CW and CCW propagations of the spin-waves, respectively. The splitting of the modes originates from interactions between the azimuthal spin-wave modes and the vortex core at the center. This was identified in an experiment by Hoffman *et al.*, [19] in which they suppress the splitting by removing the vortex core.

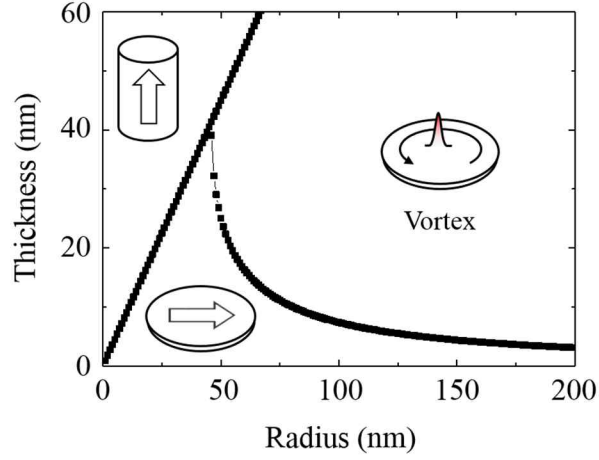


Fig. 2.1. In-plane and out-of-plane single domain – vortex boundary for permalloy nanodisks [3].

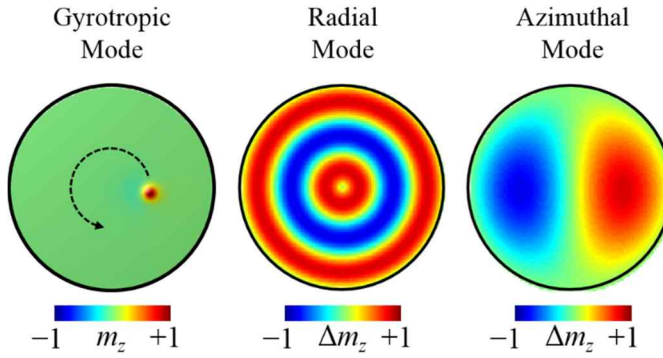


Fig. 2.2. Schematics of the gyrotropic and the radial and azimuthal spin-wave modes in soft magnetic nanodisks. The arrow in the left panel indicates gyration motion of the vortex core. The color in the dots represents m_z and Δm_z for the gyrotropic and spin-wave modes, respectively.

2.2. Vector Network Analyzer (VNA)

2.2.1. Vector Network Analyzer–Ferromagnetic Resonance Measurement

Vector network analyzer–ferromagnetic resonance (VNA-FMR) measurement is another, relatively new, inductive technique that takes advantage of VNA devices and high frequency circuit components. The VNA-FMR technique operates over a wide frequency band (up to several tens of gigahertz) and yields FMR parameters from standard scattering parameter (S -parameters see Appendix for more details) measurements as function of frequency and field. Figure 2.3 shows a diagram of the system. The microwave drive is created by a coplanar waveguide (CWG) excitation structure, with the sample placed faced down on it. The measurements are typically done by sweeping the frequency in the desired range in a fixed magnetic field and by recording the signal. The magnetic field is changed and the sequence is repeated.

As we mentioned, VNA provides the scattering parameters (S -parameters). There are several models that evaluate the permeability or the susceptibility of a magnetic material from S -parameters.

2.2.2. Reflection VNA-FMR technique

One port open circuit reflection measurements have a simplified analysis model that was proposed by Bilzer *et al.* [20]. The measurements are simplified and faster than a two-port measurement. This is because it requires the measurement of only a single reflection parameter and there is a simplified calibration procedure for a single port.

The one port system is composed of the open circuit CWG shown in Figure 2.3.

The expression for χ is a value proportional to the susceptibility of the ferromagnetic film [20]:

$$\chi = \frac{\ln(S_{11,\text{sample}})}{\ln(S_{11,\text{reference}})} - 1$$

The FMR frequency and the line width are extracted from χ . For the two-port measurements, all mentioned evaluation methods provide the resonance within 1% relative error, including the open port technique. At the same time, the relative error in the line width varies between for the methods discussed above. The Kuanr [21] method has the highest relative error, followed by the Kalarickel method, which reaches up to 10% for both methods at low fields (i.e. corresponding to low frequencies) and decreases at high frequencies to around 4% [22]. The open port evaluation method shows a relative error of below 6% in the evaluation of the line width, as reported by Bilzer *et al.* [20].

2.2.3. Transmission VNA-FMR technique

Recently, new evaluation methods for different physical parameters to be obtained from VNA-FMR have been proposed and compared with other extraction methods. Very good examples of such comparisons are presented by Kalarickal *et al.* [23] and Bilzer *et al.* [22]. Below we briefly introduce some of these methods.

Kuanr *et al.* [21] directly evaluated the resonance frequency and the linewidth from the amplitude of the transmitted signal, S_{21} . The contribution from the connections and the substrate were subtracted from a spectrum at a

field where no response was detected.

Kalarickal *et al.*, presented an evaluation of an uncalibrated effective microwave permeability parameter by neglecting reflections. Using only the transmission S_{21} -parameter of the measurements and the measurements in the reference field with parallel pumping, for which no response exists in the case of uniform magnetization, provides the uncalibrated effective microwave permeability parameter, which, according to Kalarickal *et al.* is,

$$U = \pm \frac{i \ln[S_{21,\text{sample}} - S_{21,\text{ref}}]}{\ln[S_{21,\text{ref}}]} = \pm i \left(\frac{\ln[S_{21,\text{sample}}]}{\ln[S_{21,\text{ref}}]} - 1 \right)$$

This equation presents a simplified relation that leads to additional offsets and resonance shape distortions. These distortions can be corrected by introducing additional fitting parameters as shown by Kalarickal *et al.* In this approach $-\text{Im}(U)$ is the loss profile of the resonance and $\text{Re}[U]$ gives the dispersion of the resonance. The sign in the equation of U is chosen so that U is negative around the resonance peak.

Another important approach was made by Bilzer *et al.*, which provides a value proportional to the complex susceptibility and permittivity for the ferromagnetic sample with additional corrections for the sample placement and dimensions. The above approach uses de-embedded scattering parameters (both the reflection and transmission parameters).

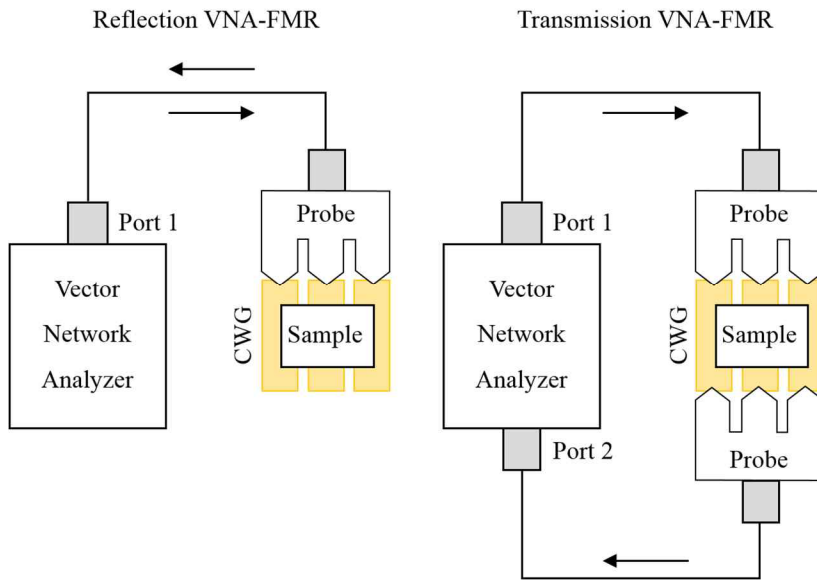


Fig. 2.3. Schematic of the VNA-FMR setup for the reflection and transmission VNA-FMR measurements.

2.3. Numerical Calculations for Spin Dynamics

2.3.1. Micromagnetics

A. Micromagnetic Energy

Ferromagnetic materials exhibit the important property of long range magnetic order. Fundamentally, this arises from a quantum mechanical effect called the exchange interaction, which forces neighboring atomic spins to be aligned in parallel under certain circumstances. From the Heisenberg model [24], the exchange interaction between neighboring atomic spins can be expressed as

$$\mathbf{H}_{\text{ex}} = -2 \sum_{i>j} J_{i,j} \mathbf{S}_i \cdot \mathbf{S}_j, \quad (2.1)$$

where J_{ij} is referred to as the exchange integral, and S_{ij} denotes the spin operator that acts on i^{th} and j^{th} atoms. The sign of J depends on the interatomic distances and can be positive or negative. The sign of J is responsible for parallel or antiparallel spin alignment. Such an exchange integral involves the overlap between wave functions, and its strength decreases very rapidly with increasing distance between ions. Accordingly, this energy, in principle, is only effective on a length scale of sub-nanometers.

The Heisenberg Hamiltonian is isotropic and hence, the magnetic properties should also be isotropic. However, in a real crystal, due to coupling between the electron orbital angular momentum and spin, spins prefer to be aligned in along certain crystallographic axes. Such direction-dependent energy originates from spin-orbit coupling and is called magnetocrystalline anisotropy energy. Meanwhile, there is a classical interaction among dipoles, called the

magnetostatic interaction. In contrast to the exchange interaction, which is dominant only in a short range, the magnetostatic interactions between magnetic dipoles play an important role in long-range characteristics within a ferromagnet.

In a realistic model, since the static and dynamic behavior of magnetic materials is determined by competition between all energy terms, all three energy terms should be taken into account. However, there is a major problem when relating fundamental atomic spin to a macroscopic magnetic moment [25]: for the case of exchange interactions, the atomic spin model is adequate, but, for the case of the magnetostatic interaction, this approach is unsuitable. Micromagnetics provides a way to overcome the gap between two different frameworks, the macroscopic Maxwell theory of electromagnetics and the atomic-level quantum theory, by imagining the atomic spins are a vector magnetization M whose direction varies continuously with position. Then Eq. (2.1) can be written as

$$E_{\text{ex}} = -2JS^2 \sum_{i>j} \phi_{i,j} \quad , \quad (2.2)$$

where $\phi_{i,j}$ is the angle difference between two neighboring magnetizations. Here, if we use the continuous variable $m = M / M_s$ for the magnetization, we get, for small angles

$$|\phi_{i,j}| \approx |m_i - m_j| \approx |(r_i \cdot \nabla) m| \quad . \quad (2.3)$$

Changing the summation over i to an integral over the volume, the exchange interaction can be rewritten as

$$E_{\text{ex}} = \int_V A \left\{ (\nabla m_x)^2 + (\nabla m_y)^2 + (\nabla m_z)^2 \right\} d^3r, \quad (2.4)$$

where A is the exchange constant, which is given as $A = nJS^2 / a$. Here, a is the lattice parameter, and n is 1, 2, and 4 for a simple cubic, body-centered, and face-centered structure, respectively.

There are several kinds of magnetic anisotropies that vary according to their origins. The most common type of anisotropy is magnetocrystalline anisotropy. Magnetocrystalline anisotropy results from spin-orbit coupling, and this, in general, can be expressed in terms of a series expansion of the directional cosine of the local magnetization moment, $\mathbf{m} = (m_x, m_y, m_z)$, relative to the crystalline axis in a lattice. In a hexagonal crystal, for example, the direction of easy magnetization, the easy axis, is the c -axis, and all directions in the basal plane are equally hard. Then, the anisotropy energy depends on only one parameter, the angle, θ , between the magnetization and the c -axis. This type of anisotropy is called uniaxial. In this case, the magnetocrystalline anisotropy of the system can be written as

$$E_{\text{ani}} = \int_V K_0' + K_1' \cos^2 \theta + K_2' \cos^4 \theta dV. \quad (2.5)$$

Using the relation, $\cos^2 \theta = 1 - \sin^2 \theta$, one can rewrite the Eq. (2.5) in the more typical form

$$E_{\text{ani}} = \int_V K_0 + K_1 \sin^2 \theta + K_2 \sin^4 \theta dV. \quad (2.6)$$

Here, K_0 , K_1 , and K_2 are anisotropy constants for particular materials at a given temperature.

In a cubic crystal system, the magnetocrystalline anisotropy energy density is given by

$$E_{\text{ani}} = \int_V K_0 + K_1 (a_1^2 a_2^2 + a_2^2 a_3^2 + a_3^2 a_1^2) + K_2 a_1^2 a_2^2 a_3^2 dV, \quad (2.7)$$

where a_1 , a_2 , and a_3 are the directional cosines of the local magnetization, \mathbf{m} . The magnetostatic interaction can be understood as the interaction of the local magnetization with the magnetic field, called the demagnetizing field, produced by its magnetization distribution. The magnetostatic interaction energy can be derived from the basic differential laws of magnetostatics,

$$\nabla \cdot \mathbf{B} = 0, \quad (2.8)$$

$$\nabla \times \mathbf{H} = \mathbf{J}, \quad (2.9)$$

where \mathbf{J} is current density inside the material. If the current density, \mathbf{J} , vanishes in some finite region, the right side in Eq. (2.9) becomes zero. Then, we can introduce a magnetic scalar potential, $\mathbf{H} = -\nabla \phi$. Substituting the magnetic scalar potential into Eq. (2.9), a magnetostatic Poisson equation analogous to that in electrostatics can be derived as

$$\nabla^2 \phi = -\rho. \quad (2.10)$$

Here, $\rho = -\nabla \cdot \mathbf{M}$ is the magnetic volume charge density. Then, the magnetostatic potential energy is

$$\phi = \frac{1}{4\pi} \int_{\text{all}} \frac{\rho(\mathbf{r}')}{|\mathbf{r} - \mathbf{r}'|} dV'. \quad (2.11)$$

If the system has a finite volume V , the system should satisfy particular boundary conditions at its surfaces. The boundary conditions can be derived from application of the divergence and Stokes theorem to Eq. (2.8) and (2.9),

respectively. This reveals that there are effective magnetic surface charges, defined as $\sigma = \mathbf{n} \cdot \mathbf{M}$, where \mathbf{n} is the unit vector normal to the surface of the element. Then, the total magnetostatic potential energy for the system with a finite volume V and surface S can be expressed as

$$E_{\text{ms}} = \frac{1}{4\pi} \int_V \frac{\rho(\mathbf{r}')}{|\mathbf{r} - \mathbf{r}'|} dV' + \frac{1}{4\pi} \int_S \frac{\sigma(\mathbf{r}')}{|\mathbf{r} - \mathbf{r}'|} dS' . \quad (2.12)$$

Eq. (2.12) reveals that the magnetostatic energy increases with increasing magnetic surface and volume charge density. Therefore, the magnetostatic interactions lead to a state with less magnetic surface and volume charges, as expected from the magnetic charge and pole-avoidance principle.

In the presence of an external magnetic field, \mathbf{H}_a , there is another type of interaction between the magnetic moment, \mathbf{m} , and the field. The applied field makes the magnetic moments align along the applied field direction. This interaction between the external magnetic field and the magnetic moments is called the Zeeman interaction. This type of interaction can be simply expressed as

$$E_{\text{Zeem}} = -\mu_0 \int_V \mathbf{M} \cdot \mathbf{H}_a dV . \quad (2.13)$$

B. Magnetic Equilibrium and Brown's Equations

The magnetic equilibrium state is realized by minimizing the total energy of the system,

$$E_{\text{total}} = \int_V \left[A(\nabla \mathbf{m})^2 + E_{\text{ani}} - \mu_0 \mathbf{M} \cdot \mathbf{H}_a - \frac{1}{2} \mu_0 \mathbf{M} \cdot \mathbf{H}_d \right] dV + \int_S \frac{1}{2} K_s (\mathbf{n} \cdot \mathbf{m})^2 dS \quad (2.14)$$

, where \mathbf{H}_a and \mathbf{H}_d denote the applied magnetic and demagnetizing field, respectively, and E_{ani} is the magnetic anisotropy energy. The second integral on right side in Eq. (2.14) represents the surface anisotropy energy, where \mathbf{n} denotes the surface normal and K_s is the surface anisotropy constant [26].

For the equilibrium state, since the total energy occurs at the stationary point, the functional variation of total energy should be zero. The first-order functional variation of the total energy is

$$\delta E_{\text{total}} = \int_V \left[2\nabla \cdot (A\nabla \mathbf{m}) + \frac{\partial E_{\text{ani}}}{\partial \mathbf{m}} + \mu_0 M_s \mathbf{H}_a - \mu_0 M_s \mathbf{H}_d \right] \cdot \delta \mathbf{m} dV + \int_S \left[2A \frac{\partial \mathbf{m}}{\partial \mathbf{n}} + K_s \mathbf{n} \cdot \mathbf{m} \mathbf{n} \right] \cdot \delta \mathbf{m} dS \quad (2.15)$$

Since the variation $\delta \mathbf{m}$ satisfies the constraint $|\mathbf{m} + \delta \mathbf{m}| = 1$, the possible variations of $\delta \mathbf{m}$ are $\delta \mathbf{m} = \mathbf{m} \times \delta \boldsymbol{\theta}$, where $\delta \boldsymbol{\theta}$ denotes a small vector rotation.

Then, after some simple vector calculus, Eq. (2.15) can be rewritten as

$$\delta E_{\text{total}} = \int_V \mathbf{m} \times \left[2\nabla \cdot (A\nabla \mathbf{m}) + \frac{\partial E_{\text{ani}}}{\partial \mathbf{m}} + \mu_0 M_s \mathbf{H}_a - \mu_0 M_s \mathbf{H}_d \right] \cdot \delta \boldsymbol{\theta} dV + \int_S \mathbf{m} \times \left[-2A \frac{\partial \mathbf{m}}{\partial \mathbf{n}} + K_s \mathbf{n} \cdot \mathbf{m} \mathbf{n} \right] \cdot \delta \boldsymbol{\theta} dS \quad (2.16)$$

For arbitrary $\delta \boldsymbol{\theta}$, Eq. (2.16) can be zero only if

$$\begin{aligned} \mathbf{m} \times \left[2\nabla \cdot (A\nabla \mathbf{m}) - \frac{\partial E_{\text{ani}}}{\partial \mathbf{m}} + \mu_0 M_s \mathbf{H}_a + \mu_0 M_s \mathbf{H}_d \right] &= 0 \quad \text{in } V \\ \mathbf{m} \times \left[-2A \frac{\partial \mathbf{m}}{\partial \mathbf{n}} + K_s \mathbf{n} \cdot \mathbf{m} \mathbf{n} \right] &= 0 \quad \text{in } S \end{aligned} \quad (2.17)$$

From Eq. (2.17), we can define an effective field as

$$\begin{aligned}\mathbf{H}_{\text{eff}} &= \frac{2}{\mu_0 M_s} \nabla \cdot (A \nabla \mathbf{m}) - \frac{1}{\mu_0 M_s} \frac{\partial E_{\text{ani}}}{\partial \mathbf{m}} + \mathbf{H}_a + \mathbf{H}_d \\ \mathbf{H}_{\text{eff}}^S &= -2A \frac{\partial \mathbf{m}}{\partial \mathbf{n}} - K_s \mathbf{n} \cdot \mathbf{m} \mathbf{n}\end{aligned}\quad (2.18)$$

Rewriting Eq. (2.17), finally, we obtain Brown's equation in the form

$$\begin{aligned}\mathbf{m} \times \mathbf{H}_{\text{eff}} &= 0 \quad \text{in } V \\ \mathbf{m} \times \mathbf{H}_{\text{eff}}^S &= 0 \quad \text{on } S\end{aligned}\quad (2.19)$$

C. Equation of Motion of Magnetization

The dynamics of the local magnetization in ferromagnetic materials can be described by

$$\frac{d\mathbf{m}}{dt} = -\gamma \mathbf{m} \times \mathbf{H}_{\text{eff}}, \quad (2.20)$$

where γ is the gyromagnetic ratio, and \mathbf{H}_{eff} is effective field arising from exchange, anisotropic, and dipolar coupling as well as the external field.

If the system reaches its equilibrium state by releasing its internal energy, the local magnetization will be collinear with the effective field direction. Then, the torque on the magnetization vanishes, as described by Eq. (2.19). This dissipative process can be taken into account by adding a dissipative to right-hand side of Eq. (2.20), as proposed Landau and Lifshitz [27]:

$$\frac{d\mathbf{M}}{dt} = -\gamma \mathbf{M} \times \mathbf{H}_{\text{eff}} - \frac{\gamma \lambda}{M_s^2} \mathbf{M} \times (\mathbf{M} \times \mathbf{H}_{\text{eff}}), \quad (2.21)$$

where λ is a dissipation parameter. There are several processes that contribute to dissipative processes in a magnetic material. These processes can have intrinsic origins, i.e. the magnon-phonon interaction, and the interaction between 3d and 4s electrons, as well as extrinsic origins. Gilbert proposed a phenomenological damping term, which combines all damping effects in a damping constant [28]. Finally, the equation of motion, called the Landau-Lifshitz Gilbert (LLG) equation, is

$$\frac{d\mathbf{M}}{dt} = -\gamma \mathbf{M} \times \mathbf{H}_{\text{eff}} - \frac{\alpha}{M_s} \mathbf{M} \times \frac{d\mathbf{M}}{dt}, \quad (2.22)$$

with a dimensionless parameter, $\alpha = \lambda / M_s$.

2.3.2. Micromagnetic Simulations

Spin dynamics in magnetic materials can be described by the Landau-Lifshitz-Gilbert (LLG) equation, introduced in Chapter 2.3.1. The LLG equation is a differential equation that describes the dynamics of individual magnetizations interacting with each other through exchange, dipole coupling, magnetocrystalline anisotropy, and the Zeeman field. In obtaining exact solutions to this equation, one confronts many technical difficulties related to the acquisition of boundary and initial conditions. Fortunately, however, an alternative solution is to use a numerical approximation, for which there are two common approaches: the finite-difference method (FDM) and the finite-element method (FEM). Both approaches lead to a set of simultaneous linear equations. In the present work, we used FDM-based Object Oriented MicroMagnetic Framework (OOMMF) [29] and FEM-based Finite Element

MicorMagnEtics (FEMME) [30] as simulation tools.

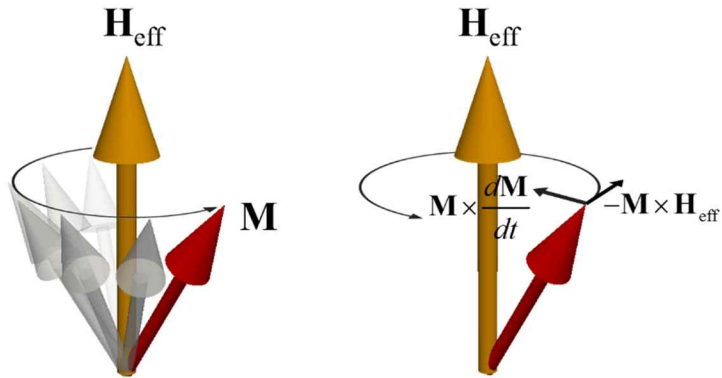


Fig. 2.4. Schematic of magnetization (\mathbf{M}) precession motion with damping around the effective magnetic field (\mathbf{H}_{eff}).

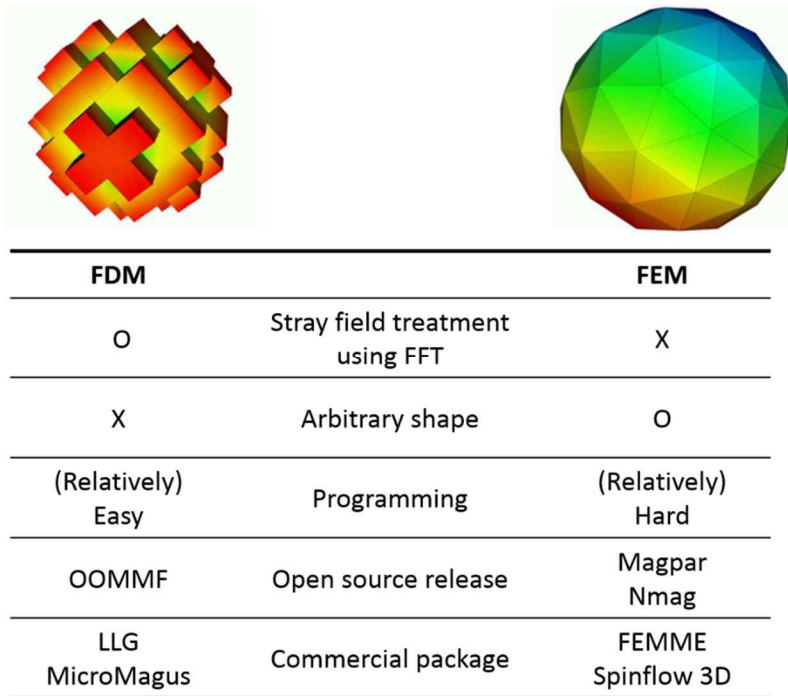


Fig. 2.5. Comparison of advantages and disadvantages between FDM and FEM methods for the micromagnetic simulations

Table 2.1. Table of material parameters of permalloy (Py)

Magnetic Parameters	Symbols	SI Units	CGS Units
Gyromagnetic Ratio	γ	$2.211 \times 10^5 \text{ m/As}$	$2\pi \times 2.8 \text{ MHz/Oe}$
Saturation Magnetization	M_s	$8.6 \times 10^5 \text{ A/m}$	860 emu/cm^3
Exchange Stiffness	A_{ex}	$1.3 \times 10^{-11} \text{ J/m}$	$1.3 \times 10^6 \text{ erg/cm}$
Damping Constant	α	0.01	0.01
Cubic Anisotropy Constant	K_1, K_2	0 J/m^3	0 erg/cm^3

References

- [1] A. Hubert and R. Schafer, Magnetic Domains (Springer, Berlin, 2000).
- [2] K. L. Metlov and K. Y. Guslienکو, Journal of Magnetism and Magnetic Materials **242**, 1015 (2002).
- [3] P. O. Jubert and R. Allenspach, Phys Rev B **70**, 144402 (2004).
- [4] J. Miltat and A. Thiaville, Science **298**, 555 (2002).
- [5] A. Wachowiak, J. Wiebe, M. Bode, O. Pietzsch, M. Morgenstern and R. Wiesendanger, Science **298**, 577 (2002).
- [6] B. Van Waeyenberge, A. Puzic, H. Stoll, K. W. Chou, T. Tyliczszak, R. Hertel, M. Fahnle, H. Bruckl, K. Rott, G. Reiss, I. Neudecker, D. Weiss, C. H. Back and G. Schutz, Nature **444**, 461 (2006).
- [7] R. F. Wang and X. W. Dong, Applied Physics Letters **100**, 082402 (2012).
- [8] M. Kammerer, M. Weigand, M. Curcic, M. Noske, M. Sproll, A. Vansteenkiste, B. Van Waeyenberge, H. Stoll, G. Woltersdorf, C. H. Back and G. Schuetz, Nature Communications **2**, 279 (2011).
- [9] V. P. Kravchuk, D. D. Sheka, Y. Gaididei and F. G. Mertens, J Appl Phys **102**, 043908 (2007).
- [10] K. Y. Guslienکو, B. A. Ivanov, V. Novosad, Y. Otani, H. Shima and K. Fukamichi, J Appl Phys **91**, 8037 (2002).
- [11] V. Novosad, M. Grimsditch, K. Y. Guslienکو, P. Vavassori, Y. Otani and S. D. Bader, Phys Rev B **66**, 052407 (2002).
- [12] B. A. Ivanov and C. E. Zaspel, Physical Review Letters **94**, 027205 (2005).
- [13] K. Y. Guslienکو, W. Scholz, R. W. Chantrell and V. Novosad, Phys Rev B **71**, 144407 (2005).

- [14] A. A. Thiele, Physical Review Letters **30**, 230 (1973).
- [15] L. D. Landau and E. M. Lifshitz, Phy. Z. Sowjetunion 8, 153 (1935); T. L. Gilbert, Phys. Rev. 100, 1243 (1955) [Abstract only; full report, Armor Research Foundation Project No. A059, Supplementary Report, May 1, 1956] (unpublished).
- [16] K. Y. Guslienko, Applied Physics Letters **89**, 022510 (2006).
- [17] K. Y. Guslienko, V. Novosad, Y. Otani, H. Shima and K. Fukamichi, Applied Physics Letters **78**, 3848 (2001).
- [18] M. Buess, R. Hollinger, T. Haug, K. Perzlmaier, U. Krey, D. Pescia, M. R. Scheinfein, D. Weiss and C. H. Back, Physical Review Letters **93**, 077207 (2004).
- [19] F. Hoffmann, G. Woltersdorf, K. Perzlmaier, A. N. Slavin, V. S. Tiberkevich, A. Bischof, D. Weiss and C. H. Back, Phys Rev B **76**, 014416 (2007).
- [20] C. Bilzer, T. Devolder, P. Crozat and C. Chappert, Ieee T Magn **44**, 3265 (2008).
- [21] B. K. Kuanr, R. E. Camley and Z. Celinski, Journal of Magnetism and Magnetic Materials **286**, 276 (2005).
- [22] C. Bilzer, T. Devolder, P. Crozat, C. Chappert, S. Cardoso and P. P. Freitas, J Appl Phys **101**, 074505 (2007).
- [23] S. S. Kalarickal, P. Krivosik, M. Z. Wu, C. E. Patton, M. L. Schneider, P. Kabos, T. J. Silva and J. P. Nibarger, J Appl Phys **99**, 093909 (2006).
- [24] S. Chikazumi, Physics of magnetizm (John Wiley & Sons, Inc., New York,

1964)

[25] W.F. Brown, Jr. Micromagnetics (Wiley, New York, 1963).

[26] G. T. Rado and J. R. Weertman, Journal of Physics and Chemistry of Solids **11**, 315 (1959).

[27] L. D. Landau and E. M. Lifshitz, Phys. Z. Sowjetunion **8**, 153 (1935).

[28] T. L. Gilbert, Ieee T Magn **40**, 3443 (2004).

[29] See <http://math.nist.gov/oommf>.

[30] D. Suess, and T. Schrefl, FEMME: Finite Element MicroMagnEtics 5.0.8 (SuessCo, <http://suessco.com/>).

Chapter 3

Radial and Azimuthal Spin-wave Modes in the Magnetic Vortex State

3.1. Introduction

Vortex magnetization configurations are of growing interest, owing to their potential applications to nonvolatile information storage, nano-oscillators, and information process devices [1-3]. There is also fundamental interest in their nontrivial dynamical characteristics, including gyrotropic [4] and spin-wave modes [5-7], and vortex-core reversals [3, 8-11]. For instance, it is well known that reliable and efficient core switching is achievable through the resonant excitation of the gyration mode when the oscillating frequency of any driving force is tuned to that mode's eigenfrequency [9, 12]. Thus, in the last decade, the gyrotropic mode in the vortex state has been intensively and extensively studied.

Understanding the spin-wave modes of the vortex state in a ferromagnetic disk is also important, because these eigenmodes control the magnetic vortex switching time as well as the threshold field strength. For example, Kammerer *et al.* reported that the azimuthal-mode-driven core reversals have an advantage, from a technological point of view, that the switching time (≤ 1 ns) is an order of magnitude faster than that of the gyrotropic-mode-driven one with a relatively small field amplitude of ~ 10 Oe

($< \sim 10$ ns) [11].

In this chapter, prior to investigating the spin-wave mode driven vortex core reversals, we identify the existence of the azimuthal and radial spin-wave modes in permalloy disks from Vector network analyzer–ferromagnetic resonance (VNA-FMR) experiments and compare the results with simulations. From the experiments and micromagnetic simulations, we observed an azimuthal frequency doublet with one pure radial mode [7, 13].

3.2. Methods

3.2.1. Experimental Method

In this study, we used the VNA-FMR method to observe azimuthal and radial spin-wave modes in permalloy nanodisks. The measurements were carried out using an Agilent E5071B VNA working at frequencies up to 20 GHz. A VNA-FMR inductive technique was used to determine the FMR frequency and the line width. The sample arrays of dots (See the Appendix) were placed face-down on top of the coplanar waveguide (CPW). The measurements were made by sweeping the frequency of an excitation signal, which was provided by VNA port 1 that runs through a CPW creating an RF field component (about 1 Oe), in the sample. This geometry ensures that the precession of the magnetization around the ground vortex state is small. In order to evaluate the eigenfrequencies of each spin-wave mode, we measured the reflection signal in port 1, which is known as S_{11} .

3.2.2. Micromagnetic Simulation Method

For the micromagnetic simulations, we used the OOMMF code [14], which incorporates the Landau-Lifshitz-Gilbert (LLG) equation of motion for the magnetization [15, 16]. We used a Py nanodisk with diameter $2R = 1200$ nm and thickness $L = 40$ nm. The unit cell size was $3 \times 3 \times 40$ nm³. Typical Py material parameters were used: the saturation magnetization $M_s = 8.6 \times 10^5$ A/m, the exchange stiffness constant $A_{\text{ex}} = 1.3 \times 10^{-11}$ J/m, and the Gilbert damping constant $\alpha = 0.01$, with zero magnetocrystalline anisotropy. To search for the

azimuthal and radial spin-wave modes excited in the dots, we applied a sinc-function field along the x - and z -axis, respectively. We then obtained a power spectrum in the frequency domain from a fast Fourier transformation (FFT) of the oscillations in the x -component of the average magnetization, $\langle m_x \rangle$.

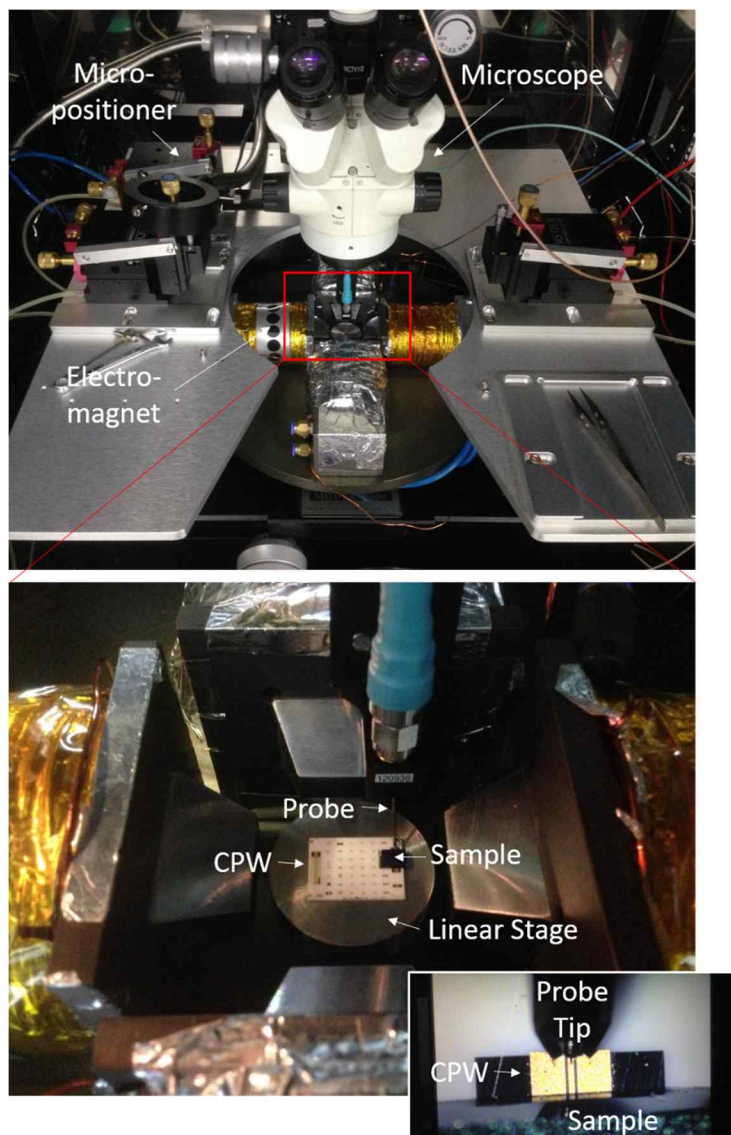


Fig. 3.1. Photograph of the experimental setup of the probe station.

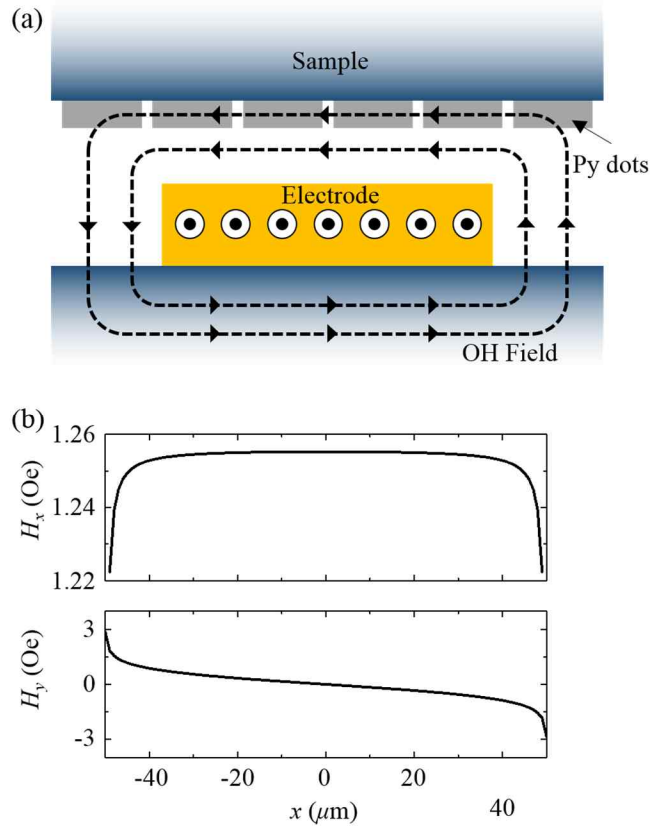


Fig. 3.2. (a) Schematic of the VNA-FMR setup. (b) Spatial distribution of magnitude of magnetic fields generated from 10- μm wide and 100-nm thick Au electrodes. The field strength was obtained 20 nm upper the top surface of the electrode.

3.3. Results and Discussion

Figure 3.3 shows the experimental frequency spectra of the dot array which had a diameter of $2R = 1200$ nm and a thickness of $L = 40$ nm ($\beta = L/R = 0.0667$). We also conducted micromagnetic simulations and compared them to the experimental results. The results are shown in Fig. 3.3. All the curves are normalized by the lowest peak frequencies f_L , which are about 5.2 and 5.8 GHz for the experiments (Fig. 3.3(a)) and the simulations (Figs. 3.3(b), (c)), respectively. The origin of a small difference between the simulated and the measured frequencies could be due to an error in saturation magnetization value used in the simulations ($M_s = 8.6 \times 10^5$ A/m). As shown in the Fig 3.3, the number of peaks and their positions are in good agreements with those of micromagnetic simulations. There are four peaks at $f/f_L = 1, 1.34, 1.58$ and 1.62 .

To classify each peak in the frequency spectra, we calculated the FFT-power spatial distributions of the local m_z in the disk using the micromagnetic simulation results, as shown in Fig. 3.4. From the results of the calculation, we found that the peaks at $f/f_L = 1, 1.34, 1.58$ and 1.62 correspond to the individual modes $(n, m) = (0, -1), (0, +1), (1, 0)$ and $(1, -1)$, respectively. Here, we note that n and m are the number of wave-function nodes in the radial and azimuthal directions. The experimental and numerical results are in good agreements with previous reports. The appearance of a weak 4-fold symmetry of the radial spin-wave patterns is due to the square-shape of the unit cells used in the simulations. The pure radial mode $(n, m) = (1, 0)$, at $f = 9.6$ GHz, can be excited in

experiments by a small perpendicular field component created in the wave guide owing to the finite size of the central conductor, as shown in Fig. 3.2(b).

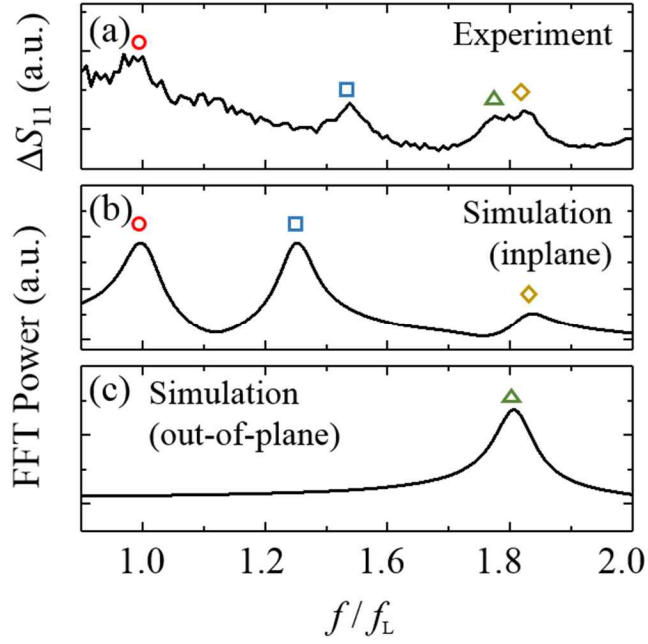


Fig. 3.3. Frequency Spectra obtained from the VNA-FMR measurement (a), and micromagnetic simulations (b, c). The circle, square, and diamond symbols indicate individual azimuthal spin-wave modes of $(n, m) = (0, -1)$, $(0, +1)$, and $(1, -1)$, respectively, and the triangle symbol represents the radial spin-wave modes of $(n, m) = (1, 0)$. To obtain the numerical data in (b) and (c), we applied sinc-function fields in the x - and z - directions, respectively, then calculated FFTs of the oscillations of the x component of averaged magnetizations.

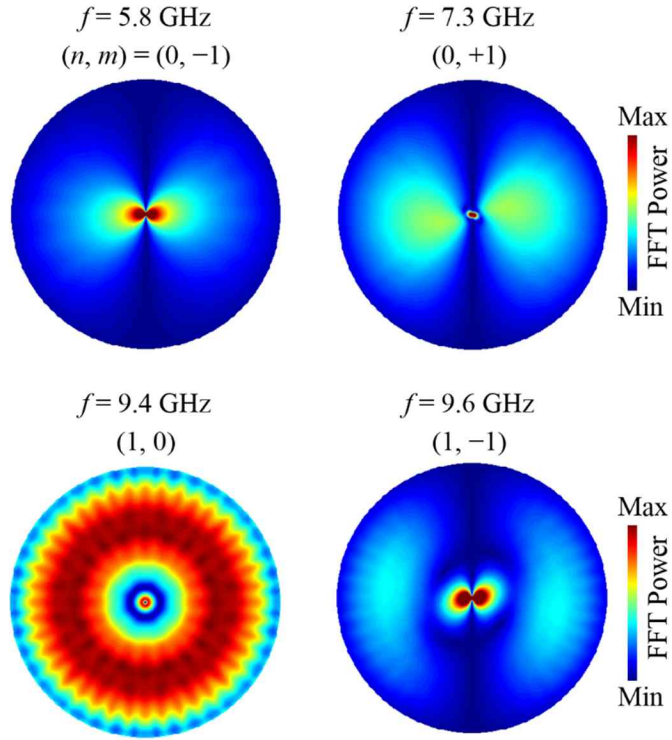


Fig. 3.4. Plane view images of spatial distributions of FFT power for $(n, m) = (0, -1)$, $(0, +1)$, $(1, 0)$, and $(1, -1)$, respectively, which modes correspond to the frequency of $f = 5.8, 7.3, 9.4$ and 9.6 GHz.

Appendix

For this experiment, we prepared square arrays of polycrystalline permalloy (Py) disks with thickness of $L = 40$ nm, and diameter of $2R = 1200$ nm. The center-to-center distance between the disks is about 2400 nm.

In order to fabricate physically and magnetically well-defined samples, we performed a number of fabrication processes in a clean room. The main fabrication processes were carried out at the *Korea Advanced Nano Fab Center* (KANC) in Suwon, Gyeonggi, South Korea. This facility has a cleanliness between class 1,000 and 1.

In this experiment, we used 280 ± 25 nm thick silicon wafers as substrates. Magnetic elements were patterned using typical electron beam lithography (JBX6000, Jeol) and subsequent lift-off processes. The lift-off method is advantageous for the patterning of difficult-to-etch noble metal thin films such as nickel, iron, platinum, and tantalum. Typically, this method proceeds as follows: 1) a pattern is defined on a substrate, 2) a film is deposited over the entire substrate, 3) the resist under the film is removed with solvent.

In this work, we used PMMA A3 950K (Micro. Chem. Corp.) as the resist layer. The PMMA A3 950K was dropped on the wafer and was spin coated at a speed of 3000 rpm for 40 s. Then, it was baked at 170 °C for 300 s on a hotplate. Electron-beam exposure was carried out with a JBX6000 operating at 50 kV and providing beam currents ranging from 100 pA to 5 nA. The exposure dosage was $390 \mu\text{C}/\text{cm}^2$. After e-beam patterning, I immersed the sample in a developer to dissolve the fragments. Methyl isobutyl ketone (MIBK)

/ isopropyl alcohol (IPA) solution was used as developer for PMMA A3 950K. Here, we used a 1:3 concentration of MIBK : IPA = 1 : 3 for narrow patterns. In the developer the sample is rinsed in IPA and de-ionized (DI) water, and is then blown with nitrogen gas.

Magnetic thin films are deposited on the patterned resists through magnetron dc sputtering. After the deposition, we removed the unpatterned area using acetone and AZ300MIF, rinsed and cleaned it using IPA and DI water again (see Fig. 3.5.).

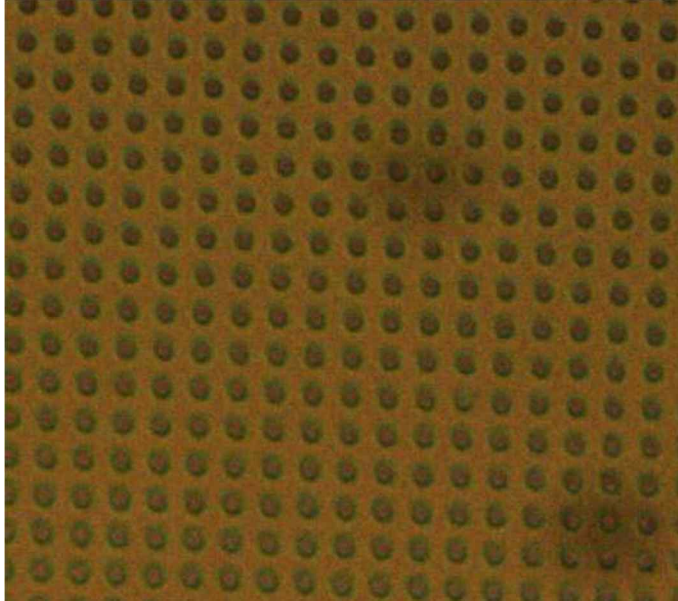


Fig. 3.5. Arrays of a permalloy nanodisk of 1.2- μm diameter and 40-nm thickness on the silicon substrate.

References

- [1] V. S. Pribiag, I. N. Krivorotov, G. D. Fuchs, P. M. Braganca, O. Ozatay, J. C. Sankey, D. C. Ralph and R. A. Buhrman, *Nature Physics* **3**, 498 (2007).
- [2] H. Jung, Y. S. Choi, K. S. Lee, D. S. Han, Y. S. Yu, M. Y. Im, P. Fischer and S. K. Kim, *Acs Nano* **6**, 3712 (2012).
- [3] B. Van Waeyenberge, A. Puzic, H. Stoll, K. W. Chou, T. Tyliczszak, R. Hertel, M. Fahnle, H. Bruckl, K. Rott, G. Reiss, I. Neudecker, D. Weiss, C. H. Back and G. Schutz, *Nature* **444**, 461 (2006).
- [4] K. Y. Gusliencko, B. A. Ivanov, V. Novosad, Y. Otani, H. Shima and K. Fukamichi, *J Appl Phys* **91**, 8037 (2002).
- [5] V. Novosad, M. Grimsditch, K. Y. Gusliencko, P. Vavassori, Y. Otani and S. D. Bader, *Phys Rev B* **66**, 052407 (2002).
- [6] M. Buess, R. Hollinger, T. Haug, K. Perzlmaier, U. Krey, D. Pescia, M. R. Scheinfein, D. Weiss and C. H. Back, *Physical Review Letters* **93**, 077207 (2004).
- [7] K. Y. Gusliencko, W. Scholz, R. W. Chantrell and V. Novosad, *Phys Rev B* **71**, 144407 (2005).
- [8] A. Thiaville, J. M. Garcia, R. Dittrich, J. Miltat and T. Schrefl, *Phys Rev B* **67**, 094410 (2003).
- [9] K. S. Lee, K. Y. Gusliencko, J. Y. Lee and S. K. Kim, *Phys Rev B* **76**, 174410 (2007).
- [10] K. Yamada, S. Kasai, Y. Nakatani, K. Kobayashi, H. Kohno, A. Thiaville and T. Ono, *Nature Materials* **6**, 269 (2007).

- [11] M. Kammerer, M. Weigand, M. Curcic, M. Noske, M. Sproll, A. Vansteenkiste, B. Van Waeyenberge, H. Stoll, G. Woltersdorf, C. H. Back and G. Schuetz, *Nature Communications* **2**, 279 (2011).
- [12] K. S. Lee, S. K. Kim, Y. S. Yu, Y. S. Choi, K. Y. Guslienko, H. Jung and P. Fischer, *Physical Review Letters* **101**, 267206 (2008).
- [13] B. A. Ivanov and C. E. Zaspel, *Physical Review Letters* **94**, 027205 (2005).
- [14] <http://math.nist.gov/oommf>.
- [15] L. D. Landau and E. M. Lifshitz, *Phys. Z. Sowjetunion* **8**, 153 (1935).
- [16] T. L. Gilbert, *Ieee T Magn* **40**, 3443 (2004).

Chapter 4

Radial Spin-wave Mode Driven Vortex Core Switching in Nanodisks

4.1. Introduction

In the magnetic vortex structure, ultrafast vortex-core magnetization reversals have attracted much attention on account of their possible implementation in information storage devices [1-5]. Low-power-driven switching is now known to be achievable possibly through the resonant excitation of a vortex-gyration mode when the oscillating frequency of any driving forces is tuned to that mode's eigenfrequency [4, 6]. However, this type of core reversals lead to the switching times \sim few ns.

In this chapter, we report on an alternative means of vortex-core switching that entails oscillating fields applied *perpendicularly* to the disk plane, the frequency of which is tuned to those of *radial* spin-wave modes.[7] Further, we address the characteristics of radial-mode-assisted vortex-core switching, which differs completely from the familiar vortex-antivortex-pair-mediated mechanism.[8-10]

4.2. Modeling

In the present study, we employed a micromagnetic simulation approach using the OOMMF code,[11] which allows for numerical calculations of the Landau-Lifshitz-Gilbert (LLG) equation[12, 13] for interacting unit cells' dynamic motions. The model system chosen was a soft magnetic Permalloy (Py: $\text{Ni}_{80}\text{Fe}_{20}$) nanodisk of $2R = 160$ nm diameter and $L = 1.0, 7.0$ and 20 nm thicknesses. Note that we show only the results for $L = 7.0$ nm, though we conducted additional simulations for different thicknesses and unit cells. The typical Py material parameters were employed: saturation magnetization $M_s = 8.6 \times 10^5$ A/m, exchange stiffness constant $A_{\text{ex}} = 1.3 \times 10^{-11}$ J/m, and Gilbert damping constant $\alpha = 0.01$, with zero magnetocrystalline anisotropy. To investigate the drastic variation of motion of local magnetizations in the proximity of a single vortex core as well as in the core itself, we used relatively small lateral unit-cell dimensions: $2 \times 2 \times L$ nm³. We also used a finer unit cell of $2 \times 2 \times 1$ nm³ to observe possible creations of the Bloch point typically found in thicker films than the usual exchange length of Py.

4.3. Results and Discussion

4.3.1. Eigenfrequencies of the Radial Spin-wave Modes

We first examined the occurrence of the radial spin-wave modes and determined their eigenfrequencies[14, 15] for the given model and dimensions (Fig. 4.1). These modes can be simply represented by the number of wave-function nodes n ($= 1, 2, 3$, etc.) in the radial direction.[15] The application of a sinc-function field for 10 ns (see Fig. 4.1(b), inset) in the direction normal to the plane of the Py disks allowed us to obtain the temporal oscillations of the m_z ($= M_z/M_s$) component over the entire nanodisk ($\langle m_z \rangle$), as shown in Fig. 4.1(b), where M_z is the out-of-plane magnetization component. The Fast Fourier transform (FFT) of the m_z oscillations of all of the individual cells and their sum over the entire disk yields the resultant FFT power in the frequency domain, as shown in Fig. 4.1(c). There exist a very strong peak at 10.7 GHz, a relatively weak peak at 15.2 GHz, and a medium-size peak at 20.7 GHz, corresponding to the eigenfrequencies of the radial modes, indexed as $n = 1, 2, 3$, respectively. Note that the $n = 2$ mode was excited weakly due to the symmetry of the excitation. The corresponding FFT-power spatial distributions of the local m_z in the disk are shown in Fig. 4.1(d). These patterns indicate that as the quantized number n increases, the eigenfrequency and the number of the wave-function node also increase. The appearance of the weak 4-fold symmetries of the radial spin-wave patterns was due to the square-shape of the unit cells used in the simulations. We confirmed this by conducting additional micromagnetic simulations using the finite-element-mesh-based FEMME

code[16] to avoid square-shaped unit cells: the calculation results showed no such 4-fold symmetries in the radial spin-wave patterns, and were almost equivalent to the results obtained with the OOMMF code [17].

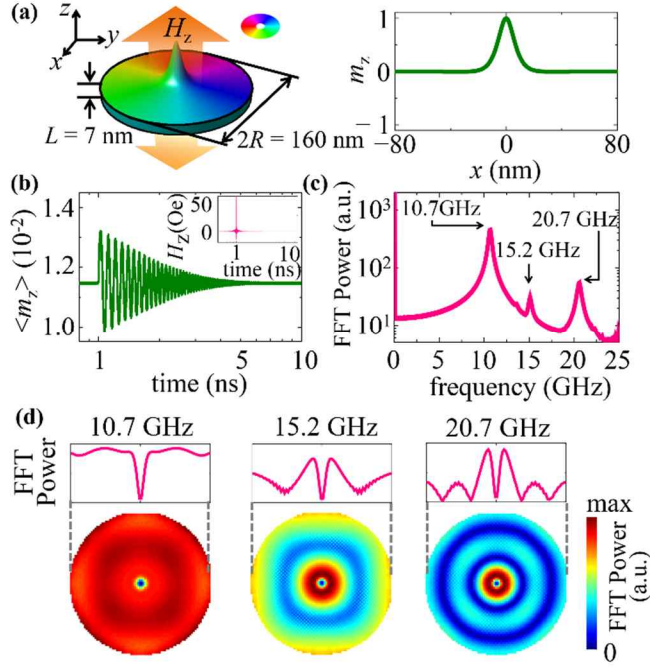


Fig. 4.1. (a) Model geometry of indicated dimensions and initial vortex ground state, wherein vortex-core magnetization is upward and in-plane curling magnetization is counter-clockwise. The orange arrow indicates the oscillating magnetic fields. On the right is the m_z component profile across the core center. (b) Average m_z component, $\langle m_z \rangle$, over entire nanodisk versus time after application of sinc field. The inset shows the sinc function expressed as $H_z = H_0 \sin[2\pi f_H(t - t_0)] / 2\pi f_H(t - t_0)$ with $H_0 = 50$ Oe, $f_H = 100$ GHz and $t_0 = 1$ ns. (c) Power spectrum obtained from method explained in text. The vertical arrows indicate the eigenfrequencies of the radial-mode spin waves. (d) Plane-view images of spatial distributions of FFT powers for $n = 1, 2$, and 3 modes obtained at corresponding eigenfrequencies 10.7, 15.2 and 20.7 GHz, respectively, along with profiles across center position.

4.3.2. Radial Spin-wave Mode Driven Vortex Core Switching

After determining the radial-mode eigenfrequencies in the model disks, we examined the radial spin-wave dynamics up to the assisted vortex-core reversals driven by single harmonic oscillating fields applied in the direction normal to the disk plane, denoted $H_z = H_0 \sin(2\pi f_H t)$, where f_H and H_0 are the field frequency and amplitude, respectively. Figure 4.2 shows serial snapshot images and the corresponding m_z profiles across the core center for the $n = 1$ radial spin-wave excitation and subsequent core reversal driven by the mode resonance frequency of 10.7 GHz along with $H_0 = 350$ Oe. It can be seen that a very weak magnetization dip around the core in the initial state fluctuates markedly around $m_z = 0$ via the resonance excitation of the $n = 1$ radial mode. At time $t = 850$ ps, the dip becomes much lower, and subsequently, the core size becomes smaller while maintaining its initial value, $m_z = +1$, at the core's very center. At time $t = 1.06$ ns, the core diameter is smallest, and then the core m_z value begins to decrease. Immediately thereafter, the vortex-core magnetization is switched to $m_z = -1$ (see the snapshot images of ⑦ and ⑧). Upon such a core-reversal occurrence, high-frequency spin waves are radiated from the core center for a very short time, ~ 0.2 ns, to dissipate the stored highest exchange energy into the area around the core. Later, at around $t = 1.6$ ns, the reversed core is switched back to $m_z = +1$. Such vortex-core switching events occurred repeatedly, as shown in Fig. 4.3(a), when oscillating fields were continuously applied.

This switching mechanism is quite interesting for the fact that it is

entirely different from the well-known vortex-antivortex-pair-mediated one.[8-10] As also noted by Pylypovskyi *et al.*,[18] the radial symmetric spin configuration was maintained during the reversal (see Fig. 4.2), and thus is referred to as symmetric switching, whereas the creation and annihilation of the vortex-antivortex pair reveals the asymmetric spin configuration. In order to elucidate the underlying physics, therefore, we considered the variations of the exchange, demagnetization, and Zeeman energy density terms and their sums during the radial-mode spin-wave excitations and the associated switching (see Fig. 4.3(b)). These local energy densities were calculated over a local area of $r \leq 4$ nm (averaged laterally over 12 cells) around the core center, because the radial-mode spin-wave excitations also modify the exchange energy over the entire disk area during assisted vortex-core reversals. Comparisons of the individual energy terms revealed that the external oscillating field excites the radial spin-wave mode through the Zeeman energy, and that subsequently, the demagnetization energy induced by the radial mode excitation is transferred to the exchange energy, as evidenced by the mutual transfer between the demagnetization and exchange energies (see Fig. 4.3(c)). The radial-mode resonant excitation assists dynamic fluctuations of both the magnetization dip around the core and the core size, thus yielding the deeper magnetization dip and the narrower core. The large gradient of the m_z component of the core reflects the increased exchange energy strongly localized in the core region. Figures 4.3(a) and 4.3(b) evidence that whenever the exchange energy density at the core reaches its maximum value, here $E_{\text{ex}}^{\text{max}} = 2.54 \times 10^6$ J/m³, the

vortex-core magnetization is reversed at the cost of the achieved maximal exchange energy. Interestingly, the maximal value was close to the maximum exchange energy density, $E_{\text{ex,static}}^{\text{max}} = 2.62 \times 10^6 \text{ J/m}^3$, obtained just before a vortex-core switching event in the same model disk, but as driven by a static field of $H_{\text{static}}^{\text{cri}} = -5.29 \text{ kOe}$ applied perpendicularly to the disk plane. The negative sign of the field indicates a field direction opposite to the initial vortex-core magnetization.

In the works of Thiaville *et al.* [19] and Hertel and Schneider, [20] creation and injection of the Bloch point were addressed. In order to elucidate the role of these mechanisms in core reversals, we compared the reversal events for two cases, $2 \times 2 \times 1 \text{ nm}^3$ and $2 \times 2 \times L \text{ nm}$. For $2 \times 2 \times L \text{ nm}^3$, where the cell was not divided along the z-axis (thickness), we could not observe any Bloch point injection. In further simulations with the finer $2 \times 2 \times 1 \text{ nm}^3$ cell and with the 20 nm thickness, the Bloch point creation and injection were clearly observed, whereas with the 7 nm thickness, only a part of the Bloch point was created, not the entire structure, because the exchange interaction was strong enough to prevent formation of the full structure. The exchange energy density required for the core reversal with the 7 nm thickness was almost equal for the different cell sizes, whereas with the 20 nm thickness, the creation and injection of the full Bloch point structure lead to reductions of the exchange energy density; thus, the threshold energy density with the 1 nm cell size in the z-direction was reduced by 12% compared with the thicker cell size. This was owed to the fact that formation of the complete Bloch point structure yields an

exchange energy reduction. Regardless of whether the Bloch point is formed completely or not, the core reversals assisted by the radial-mode excitation occur whenever the exchange energy densities reach the corresponding threshold values. In order to define the critical exchange energy required for the radial-mode-assisted reversals, it would be necessary to use finer, less-than-exchange-length cell sizes.

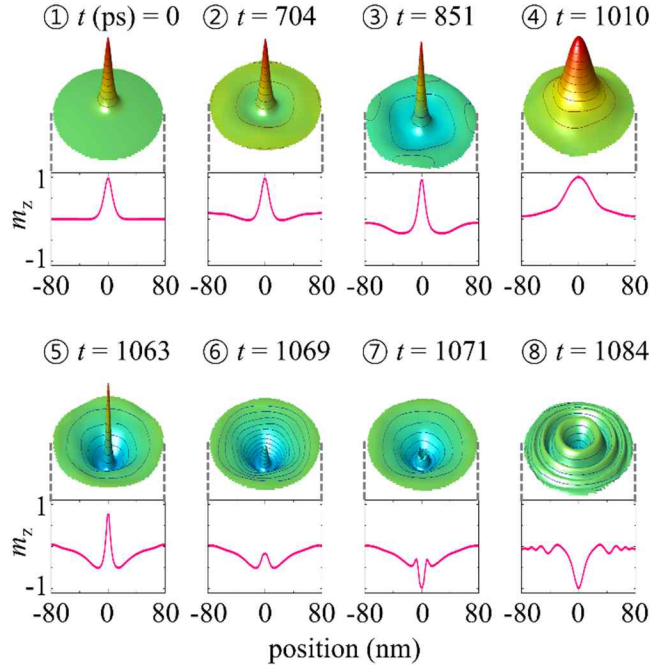


Fig. 4.2. Snapshot images of temporal evolution of $n = 1$ radial mode excitation up to vortex-core reversal, with corresponding m_z profiles. The field applied was a single harmonic sine-wave field of $H_0 = 350$ Oe and $f_H = 10.7$ GHz.

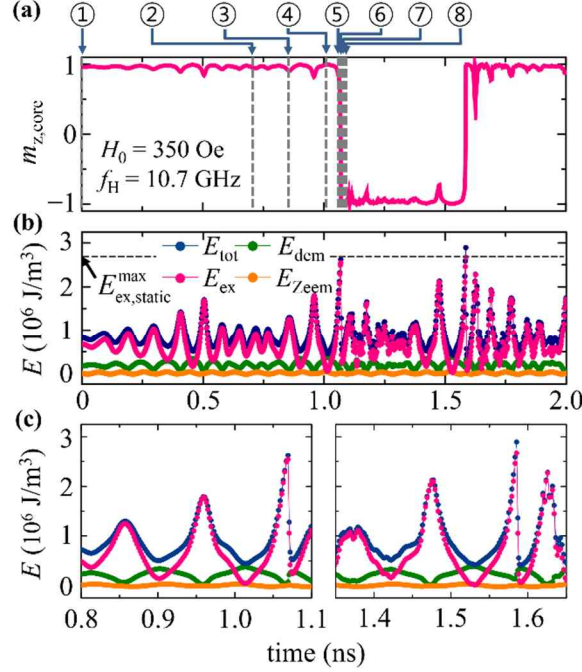


Fig. 4.3. (a) Variation of m_z component averaged over core region (i.e. averaged over 4 cells) during excitation of $n = 1$ radial mode up to vortex-core reversal. (b) Temporal variation of each energy density and sum averaged over core region ($r \leq 4$ nm). The gray dashed line shows the maximum exchange energy density, $E_{\text{ex,static}}^{\text{max}} = 2.62 \times 10^6$ J/m³, obtained during the vortex-core reversal driven by a perpendicular bias static field, $H_{z,\text{static}}^{\text{cri}} \approx -5.29$ kOe. The numbers on the top of the panel in (a) indicate the times at which the snapshot images shown in Fig. 4.2 were taken. (c) Same as (b), but for time ranges spanning occurrence of switching events.

4.3.3. Threshold Field and Switching Time for the Core Reversals

Figure 4.4(a) shows the result for additional micromagnetic simulations on a switching phase diagram with respect to both H_0 and f_H in the $H_0 = 100 - 1400$ Oe (interval: 100 Oe) and $f_H = 8 - 21$ GHz (interval: 1 GHz) ranges. Whether vortex-core switching took place or not was monitored by referencing the variation of the core m_z component versus time and the subsequent exchange-energy-density variation. The open circles represent the occurrence of vortex-core reversals for the indicated H_0 and f_H values, in which cases the maximum exchange energy density $E_{\text{ex}}^{\text{max}}$ is always larger than $E_{\text{ex,static}}^{\text{max}} = 2.62 \times 10^6 \text{ J/m}^3$. Otherwise, no vortex-core switching event occurs, because $E_{\text{ex}}^{\text{max}}$ is less than $E_{\text{ex,static}}^{\text{max}}$. We confirmed that, in cases of radial-spin-wave-mode-assisted core reversals, the switching event occurs whenever $E_{\text{ex}}^{\text{max}}$ reaches $E_{\text{ex,static}}^{\text{max}}$, independently of H_0 , f_H and the dimensions of the Py disk, as revealed by additional simulations with different dimensions (data not shown here). Thus, $E_{\text{ex,static}}^{\text{max}}$ can be used as a criterion for the occurrence of the radial-spin-wave-mode-assisted core-reversal mechanism.

The phase diagram also shows that the local minima (10, 14 and 19 GHz) of the threshold field strength (solid line) versus f_H coincide with the corresponding eigenfrequencies of the $n = 1, 2$ and 3 radial modes, respectively. Such a remarkable reduction of the threshold field, down to 200 Oe for 10 GHz, originates from the assistance of the strong resonant excitation of the $n = 1$ radial mode, as noted above. This strength is an order of magnitude smaller than

the value of $H_{z,\text{static}}^{\text{cri}} \approx -5.29$ kOe. And note that the reason for the no-switching event at the $n = 2$ mode eigenfrequency is likely that this mode's spin-wave excitation is much weaker than that of the other, $n = 1$ and $n = 3$ modes. We also provide, in Fig. 4.4(b), the times required to complete switching after application of the oscillating field. The higher the field strength, the faster the switching time, which, in the case of the present model, ranged from 0.15 ns to 1.4 ns. This is comparable to or slightly faster than the switching events assisted by the resonance of the vortex-core translation mode.[21]

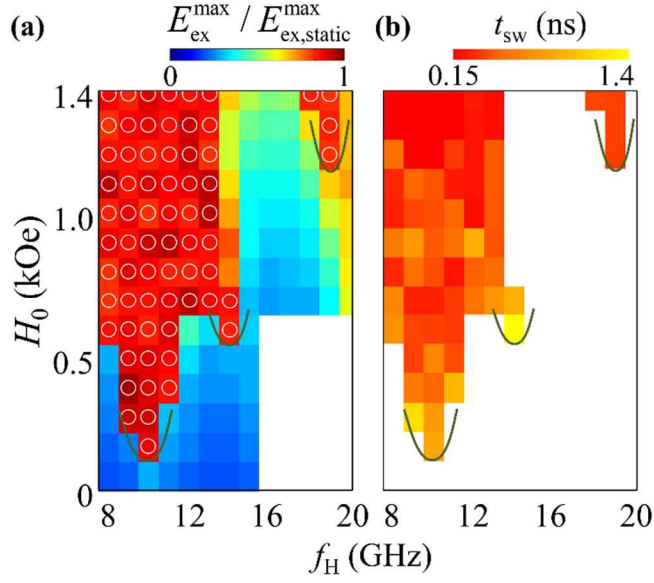


Fig. 4.4. Phase diagrams of (a) switching events and (b) switching times with respect to H_0 and f_H . In (a), the large open circles represent the occurrence of vortex-core-reversal events at the indicated H_0 and f_H values. The colors, according to the color bar scale (top), represent the $E_{\text{ex}}^{\text{max}} / E_{\text{ex,static}}^{\text{max}}$ values. The solid curves indicate the threshold fields near the radial-mode eigenfrequencies. In (b), the colors in the vortex-core-reversal region, according to the color bar scale (top), correspond to the switching times.

References

- [1] J. Thomas, *Nature Nanotechnology* **2**, 206 (2007).
- [2] R. P. Cowburn, *Nature Materials* **6**, 255 (2007).
- [3] S. Bohlens, B. Kruger, A. Drews, M. Bolte, G. Meier and D. Pfannkuche, *Applied Physics Letters* **93**, 142508 (2008).
- [4] S. K. Kim, K. S. Lee, Y. S. Yu and Y. S. Choi, *Applied Physics Letters* **92**, 022509 (2008).
- [5] Y. S. Choi, M. W. Yoo, K. S. Lee, Y. S. Yu, H. Jung and S. K. Kim, *Applied Physics Letters* **96**, 072507 (2010).
- [6] K. Yamada, S. Kasai, Y. Nakatani, K. Kobayashi, H. Kohno, A. Thiaville and T. Ono, *Nature Materials* **6**, 269 (2007).
- [7] R. F. Wang and X. W. Dong, *Applied Physics Letters* **100**, 082402 (2012).
- [8] B. Van Waeyenberge, A. Puzic, H. Stoll, K. W. Chou, T. Tyliczszak, R. Hertel, M. Fahnle, H. Bruckl, K. Rott, G. Reiss, I. Neudecker, D. Weiss, C. H. Back and G. Schutz, *Nature* **444**, 461 (2006).
- [9] K. S. Lee, K. Y. Guslienko, J. Y. Lee and S. K. Kim, *Phys Rev B* **76**, 174410 (2007).
- [10] R. Hertel, S. Gliga, M. Fahnle and C. M. Schneider, *Physical Review Letters* **98**, 117201 (2007).
- [11] M. J. Donahue, (National Institute of Standards and Technology, 2002).
- [12] L. D. Landau and E. M. Lifshitz, *Phys. Z. Sowjetunion* **8**, 153 (1935).
- [13] T. L. Gilbert, *Ieee T Magn* **40**, 3443 (2004).
- [14] M. Buess, R. Hollinger, T. Haug, K. Perzlmaier, U. Krey, D. Pescia, M. R.

- Scheinfein, D. Weiss and C. H. Back, Physical Review Letters **93**, 077207 (2004).
- [15] K. Y. Guslienko, W. Scholz, R. W. Chantrell and V. Novosad, Phys Rev B **71**, 144407 (2005).
- [16] T. Schrefl and J. Fidler, Journal of Magnetism and Magnetic Materials **155**, 389 (1996).
- [17] See <http://math.nist.gov/oommf>.
- [18] O. V. Pylypovskiy, D. D. Sheka and Y. Gaididei, Phys Rev B **85**, 224401 (2012).
- [19] A. Thiaville, J. M. Garcia, R. Dittrich, J. Miltat and T. Schrefl, Phys Rev B **67**, 094410 (2003).
- [20] R. Hertel and C. M. Schneider, Physical Review Letters **97**, 177202 (2006).
- [21] K. S. Lee, S. K. Kim, Y. S. Yu, Y. S. Choi, K. Y. Guslienko, H. Jung and P. Fischer, Physical Review Letters **101**, 267206 (2008).

Chapter 5

Azimuthal Spin-wave Mode Driven

Vortex Core Switching in Nanodisks

5.1. Introduction

In the chapter 4, we examined the means of vortex-core switching assisted by the resonance of the radial spin-wave modes, and found that the mechanism differs from the well-known vortex-antivortex (V-AV) mediated core switching [1-4]. In chapter 5, we explore the azimuthal spin-wave driven vortex-core switching.

The fundamentals of the azimuthal-mode-driven core reversals have been relatively less explored than the gyrotropic mode driven core switching so far. Just a few reports reveal that the reversal mechanism is the same as the nucleation and annihilation process of the V-AV pair, and that the magnetization dip, as in gyrotropic-mode-driven reversals, also plays a key role as the reversal criterion [5-8]. However, the maximum core-motion speed and perpendicular gyrofield necessary to meet the $m_z = -p$ criterion differ between the $m = -1$ and $m = +1$ azimuthal-modes-driven core reversals, because they are also associated with the $m = -1$ and $m = +1$ azimuthal modes themselves [6]. The azimuthal-mode-driven core reversals have the advantage, from a technological point of view, that the switching time (≤ 1 ns) is an order of magnitude faster than that ($< \sim 10$ ns) driven by the gyrotropic-mode excitation similar to the radial spin-

wave mode mediated core switching [9, 10].

In this work, we explored, on the basis of micromagnetic numerical calculations, the similarities and differences between the asymmetric dynamics of the $m = -1$ and $m = +1$ mode-driven core reversals, specifically in terms of the correlations among the magnetization dip criterion, the core-motion speed, and the perpendicular gyrofield. We also studied the effect of perpendicular bias field, not only on those correlations but also on the consequent switching time and threshold exciting field strength required for the vortex-core reversals. Our numerical calculations and quantitative interpretations elucidate the fundamentals of the azimuthal-mode-driven core reversals and, in so doing, provide valuable knowledge on the manipulation of those events from a technological point of view.

5.2. Modeling

In order to numerically calculate magnetization dynamics on a few nm spatial and ps temporal scales, we utilized a well-established and optimized tool, namely the OOMMF code [11] based on the Landau-Lifshitz-Gilbert equation [12, 13]. The model system used was a Permalloy (Py: $\text{Ni}_{80}\text{Fe}_{20}$) soft ferromagnetic circular disk of diameter $2R = 300$ nm and thickness $L = 20$ nm (see Fig. 5.1(a)). The Py material parameters applied were as follows: saturation magnetization $M_s = 8.6 \times 10^5$ A/m, exchange stiffness constant $A_{\text{ex}} = 1.3 \times 10^{-11}$ J/m, Gilbert damping constant $\alpha = 0.01$, and zero magnetocrystalline anisotropy. The lateral dimensions of the unit cells were intended to be as small as $1 \times 1 \times L$ nm³ in order to determine the core position in small deviations (< 20 nm) from the disk's center in azimuthal-mode excitations. The vortex structure in the initial state is the CCW in-plane curling magnetization around the upward core magnetization, as indicated in Fig. 5.1(a). To excite the intrinsic modes in the given disk, we applied a sinc-function field expressed as $H\hat{\mathbf{x}} = \hat{\mathbf{x}}H_0 \sin[\omega_H(t - t_0)]/[\omega_H(t - t_0)]$ with $H_0 = 10$ Oe, $\omega_H = 2\pi \times 50$ GHz and $t_0 = 1$ ns, during a period of $t = 10$ ns. The results obtained from the fast Fourier transform (FFT) of the temporal oscillations of $m_x = M_x/M_s$ averaged over the entire nano-disk are plotted in Fig. 5.1(b). Three distinct peaks were found at 0.6, 8.6 and 10.5 GHz, respectively, which corresponded to the eigenfrequencies of the gyrotropic and $m = -1$ and $m = +1$ azimuthal modes, respectively [6].

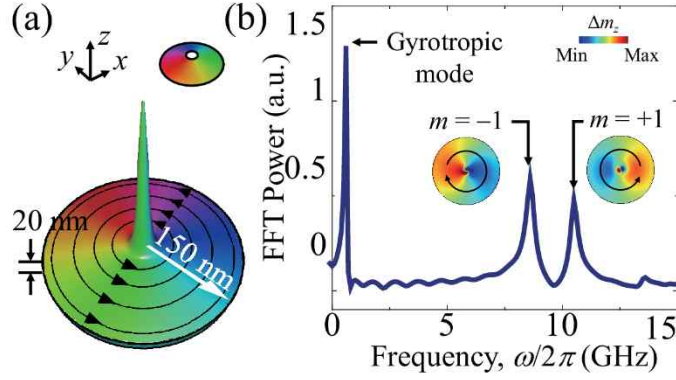


Fig. 5.1. (a) Geometry and dimensions of cylindrical nanodot used as model system. The colors display the in-plane components of local magnetizations, as indicated by the color wheel. The height of the surface represents the out-of-plane component of the local magnetization. The spike at the center corresponds to the upward core. (b) FFT power spectrum including all excited modes up to 15 GHz. The inset shows schematic images of the local $\Delta m_z (= m_z(t) - m_z(t=0))$ distributions by the excitations of the $m = -1$ and $m = +1$ azimuthal modes. The CW and CCW arrows inside the disks indicate the propagation directions of the $m = -1$ and $m = +1$ azimuthal spin-waves, respectively.

5.3. Results and Discussion

5.3.1. Azimuthal-mode-driven core reversals

According to the information on the eigenfrequencies of the three distinct modes from the FFT power spectrum, we applied a CCW circular-rotating field for the resonant excitation of each of the gyrotropic and $m = +1$ modes as well as a CW circular-rotating field for the $m = -1$ mode excitation, along with the corresponding resonant field frequency ω_H [5, 6, 14]. For the gyrotropic mode, we specifically used $[\omega_H/2\pi, H_0] = [580 \text{ MHz}, 15 \text{ Oe}]$, and for the $m = -1$ and $m = +1$ mode-resonant excitations, $[8.4 \text{ GHz}, 90 \text{ Oe}]$ and $[10.0 \text{ GHz}, 130 \text{ Oe}]$, respectively, where H_0 is the field strength of the circular-rotating fields [15]. Figure 5.2 compares the resultant trajectories of the vortex-core motions around the disk's center, as excited by the corresponding modes just before the core-reversal occurrences. For the gyrotropic mode, the core motion is in the CCW rotation sense with increasing orbit radius $|\mathbf{X}|$, because the upward core magnetization ($p = +1$) has a CCW-gyration eigenmode (Fig. 5.2(a)) [14, 16]. When the $|\mathbf{X}|$ reaches $\sim 98.7 \text{ nm}$, the core magnetization switches just after the core-motion speed reaches its threshold value, $\sim 330 \pm 37 \text{ m/s}$ for Py [17]. The oscillations of the x - and y -components of the core (here X and Y) show that the gyration frequency is equal to the eigenfrequency of that mode, $\sim 0.6 \text{ GHz}$.

In contrast to gyrotropic-mode excitation, core motions driven by the excitation of each of the azimuthal modes are totally different, as seen in Figs.

5.2(b) and 5.2(c). The maximum orbiting radii of those core motions are as small as ~ 15.6 nm and ~ 9.8 nm for the $m = -1$ and $m = +1$ modes, respectively, which are much smaller than that of the gyrotropic mode, ~ 98.7 nm here. Also, the opposite rotation senses of the $m = -1$ and $m = +1$ modes result in CW and CCW core gyrations of much higher frequency, about 8.3 GHz and 9.7 GHz, respectively. Here we note that the CW rotation sense of the core motion is opposite to the gyration sense of the up core [14, 16], and that the core motion's frequencies coincide exactly with those of the $m = -1$ and $m = +1$ azimuthal spin-wave modes. Thus, these asymmetric core motions are not caused by gyrotropic eigenmode excitation, but rather by the excited azimuthal modes through their interaction with the given upward core [6]. We also note here that the azimuthal-mode-driven core reversals occur much faster than the gyrotropic-mode-driven ones, because the azimuthal modes' eigenfrequencies are one order of magnitude higher than the gyrotropic mode's [5, 6, 9, 10].

In order to elucidate additional details on the core-reversal mechanism, we display snapshot images of the spatial distributions of the out-of-plane magnetization component m_z and the perpendicular gyrofield h_z for the gyrotropic- and $m = -1$ and $m = +1$ azimuthal-mode-driven core reversals (see Fig. 5.3). The gyrofield is expressed as $h_z = -1/(\gamma M_s^2) [\mathbf{M} \times (d\mathbf{M}/dt)]_z$, and is known to be produced by the deformation of the in-plane magnetizations and to be strongly concentrated in proximity to a magnetization dip of a magnetization opposite to that of the original core [18, 19]. In the case of the gyrotropic-mode excitation, the magnetization dip, as indicated by the white

circles in the second row of Fig. 5.3(a), is increased in the $-z$ direction, because the local h_z is concentrated on the dip in the negative ($-z$) direction (see the bottom row of Fig. 5.3(a)). Figures 5.3(b) and 5.3(c) illustrate the dip formation and the V-AV pair nucleation and subsequent annihilation processes for both of the azimuthal-mode-driven core reversals. Unlike the highly localized m_z distributions in the gyrotropic-mode case, the azimuthal spin-wave modes show relatively broad positive and negative m_z regions in the m_z spatial distribution. Somewhere, the local minimum m_z of the negative region is lower than that of the magnetization dip, $m_{z,\text{dip}}$, for the $m = +1$ mode excitation (see the images at $t = 0.600$ ns), but the deeper m_z region does not transform into a V-AV pair required for core reversal, because they are relatively far from the position of the original core (> 40 nm). Since the magnetization dip acts as the core-reversal criterion, the underlying physics of the magnetization dip formation, and the effect of the excited azimuthal modes on it, should be more clearly identified. Kravchuk *et al.* explained that the physical origin of the dip creation is the softening of the dipole magnon mode [20]. While this adequately accounts for the development of the magnetization dip, it does not explain why the dip positions differ between the $m = -1$ and $m = +1$ modes. On the other hand, Kammerer *et al.* argued that the dip formation and position can be understood in terms of the combination of the gyrofield and excited azimuthal spin waves [6].

In order to better understand the quantitative correlations among the magnetization dip, h_z and core-gyration speed v for the three different mode-

driven core reversals, we compared the temporal evolution of the correlations among the v , the local minimum h_z , and the dip magnetization component $m_{z,\text{dip}}$ during the period from each mode's excitation to the first core-switching event, as shown in Fig. 5.4. For the gyrotropic-mode-driven core reversal, the v , $|h_z|$ and $|m_{z,\text{dip}}|$ monotonically increase with time except when near the core-reversal occurrence [19]. Thus, when the $m_{z,\text{dip}}$ value reaches the reversal criterion $m_{z,\text{dip}} = -p$, upon which the core immediately switches, the v and resultant $|h_z|$ are maximized to ~ 340 m/s and ~ 4.0 kOe, respectively. As seen in the bottom rows of Figs. 5.4(b) and 5.4(c), the criterion for the core reversals driven by the azimuthal-mode excitations is, similarly to the gyrotropic mode excitation, still maintained to be $m_{z,\text{dip}} = -p$. However, dissimilarly to the gyrotropic mode, the maximum v reaches ~ 370 m/s for the $m = -1$ mode and ~ 800 m/s for the $m = +1$ mode [21], which speeds are much higher than that of the gyrotropic mode's threshold core-motion, ~ 330 m/s [17], despite the core's orbit radii being much smaller than those in the gyrotropic-mode excitation. Thus, in the case of azimuthal-mode-driven core switching, the v no longer acts as a measurable core-reversal criterion [6]. Also the temporal evolutions of the h_z values for the azimuthal modes show more complicated behavior than those for the gyrotropic mode, and neither, now, do they show any correlation with v , as seen in Figs. 5.4(b) and 5.4(c). Moreover, for the $m = +1$ mode, the criterion $m_{z,\text{dip}} = -p$ cannot be achieved, even though $|h_z|$ attains its maximum value, ~ 10.8 kOe. This complicated nonlinear effect seems to be caused by the excited azimuthal modes that generate additional in-plane magnetization deformation and modify

the ground magnetization level of the dip near the original core. The azimuthal spin-waves can change the starting m_z level (m_z^g) of the magnetization dip and, thereby, affect how efficiently the magnetization dip near the core reaches its reversal criterion, $m_{z,\text{dip}} = -p$ [6].

Therefore, in order to elucidate the effect of azimuthal-spin-wave-mode-induced m_z variations on the formation of the magnetization dip, we intended to estimate the quantitative correlations of the h_z , $m_{z,\text{dip}}$ and m_z^g [22]. However, since direct estimation of m_z^g in azimuthal-mode-induced core reversals is not straightforward, we investigated the m_z^g variation instead with varying perpendicular bias fields applied to gyrotropic-mode-driven core reversals[23, 24][25]. Figures 5.5(a) and 5.5(b) show the initial m_z distributions and profiles across the core position according to H_z varying within the $-4 - +5$ kOe range at intervals of 1 kOe, with the corresponding m_z^g plotted in Fig. 5.5(c). For different m_z^g values, the evolutions of h_z and $m_{z,\text{dip}}$ were obtained from the gyrotropic-mode-driven core reversals using a CCW circular-rotating field of $H_0 = 30$ Oe (Fig. 5.5(d)) [22]. As plotted in Fig. 5.5(d), the simulation results clearly show the distinct $m_{z,\text{dip}}$ and h_z correlation according to m_z^g that varies with H_z . These results make clear that the level of m_z^g modifies the local minimum h_z to meet the criterion $m_{z,\text{dip}} = -p$, that is, the deeper the level of m_z^g , the smaller the $|h_z|$. Based on those results, we found that the h_z is related to not only v but also the ground m_z level of the magnetization dip, and the h_z

influenced by excited spin-waves and the azimuthal modes themselves affect the dynamic evolution of the magnetization dip formation for core-reversal events.

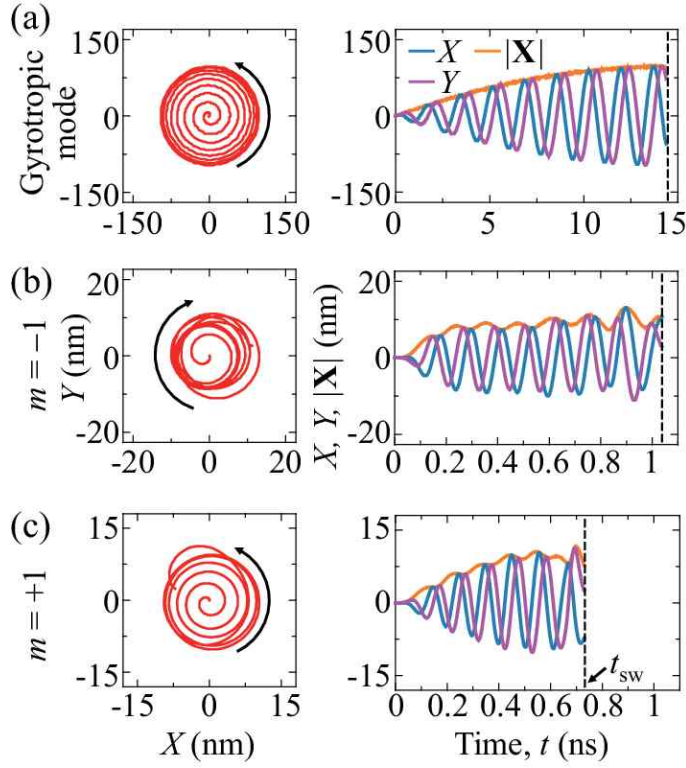


Fig. 5.2. Left column: Trajectories of vortex-core motions of (a) gyrotropic mode, (b) $m = -1$ and (c) $m = +1$ azimuthal spin-wave modes just before vortex-core reversal events. Right column: Corresponding temporal evolutions of x - and y -components and displacement of vortex-core positions from each disk center. The dotted vertical lines correspond to the moments when core reversals occur.

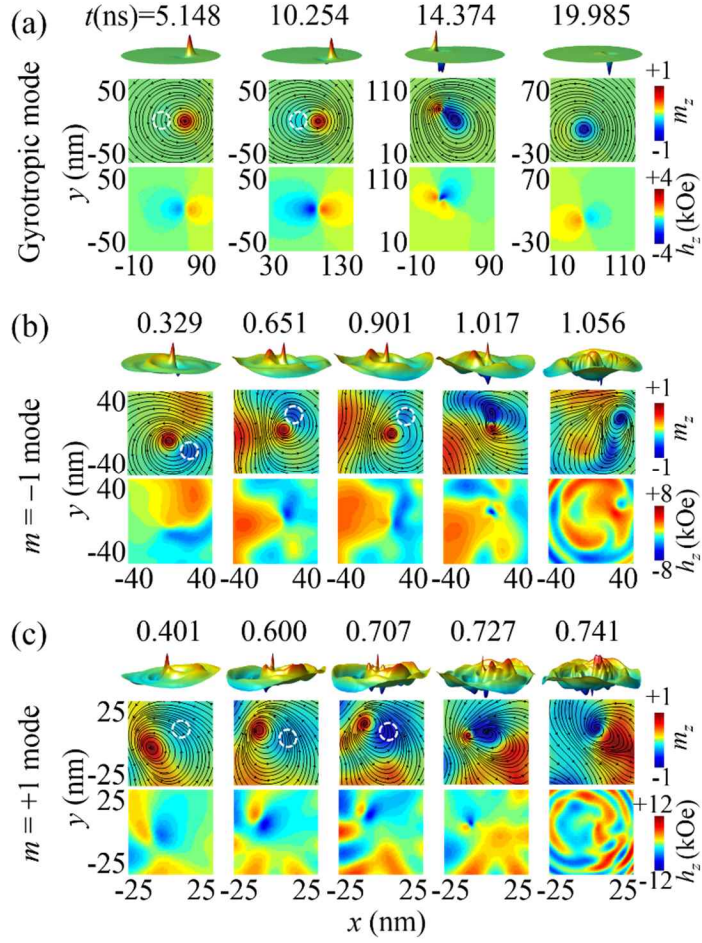


Fig. 5.3. Snapshot images of local magnetizations' distributions in perspective view (top), in-plane view (middle) and corresponding perpendicular gyrofields (bottom) during vortex-core reversals driven by (a) gyrotropic mode and (b) $m = -1$ and (c) $m = +1$ azimuthal mode excitations. The white circles in each middle row indicate the magnetization dips of negative m_z values.

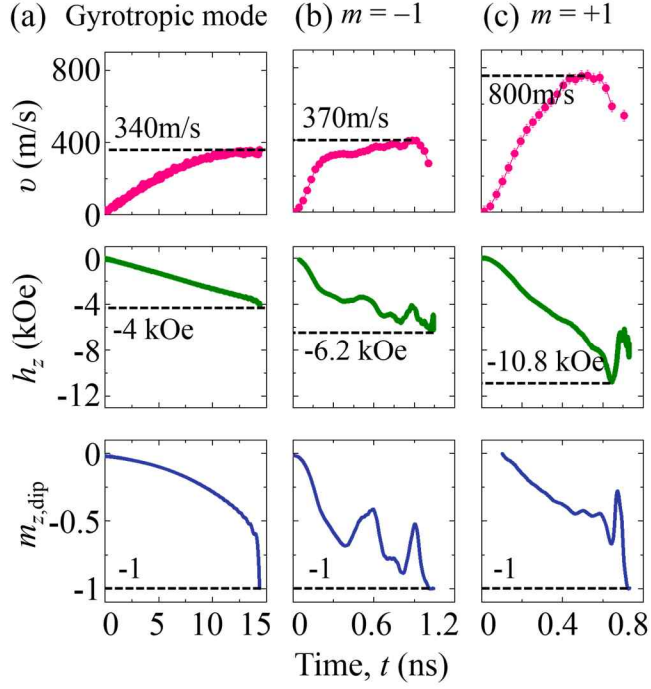


Fig. 5.4. Temporal variations of core motion's speed v , local minimum gyrofield h_z , and m_z component of magnetization dip, compared for (a) gyrotropic mode, (b) $m = -1$ and (c) $m = +1$ azimuthal spin-wave-mode-driven core reversals. The horizontal dashed lines display each of the maximum values of v , $|h_z|$, and $|m_{z,dip}|$.

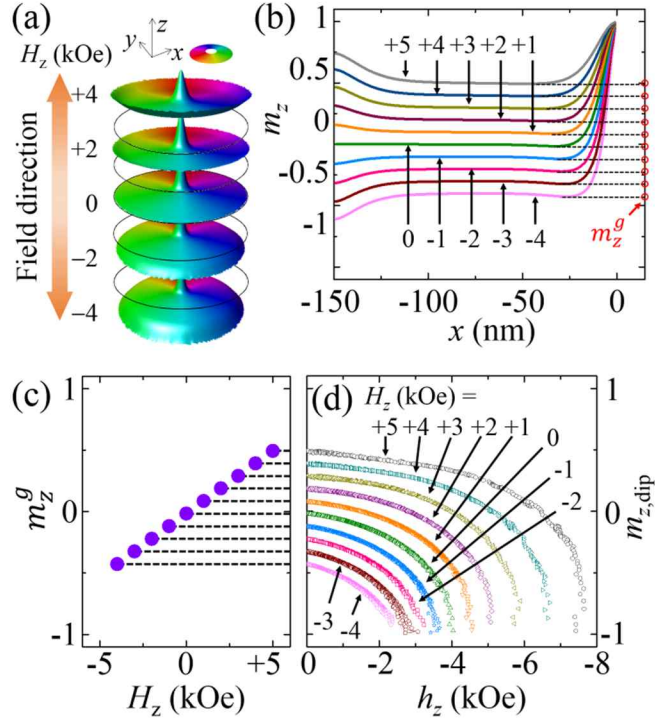


Fig. 5.5. (a) Local magnetization distributions of initial ground states of magnetizations inside disk according to perpendicular magnetic field with indicated field strength H_z . The black circles correspond to the $m_z = 0$ level. (b) H_z -dependent m_z profiles across each disk center from left edge to core center. The horizontal dashed lines indicate the ground (starting) m_z level of the dip near the core, m_z^g . (c) H_z -dependence of m_z^g . (d) Temporal evolution of $m_{z,\text{dip}}$ according to h_z temporal evolution during core gyration up to switching event by gyrotropic-mode-resonant excitation under different H_z values as indicated.

5.3.2. Control of core reversals by perpendicular bias field

Next, on the basis of the correlation of h_z and $m_{z,\text{dip}}$ with H_z , we examined the effect of H_z on the azimuthal-mode-driven core reversals. We carried out further micromagnetic simulations on Py nano-disks of larger dimensions, for example, $2R = 1200$ nm and $L = 40$ nm with a unit cell size of $3 \times 3 \times 40$ nm³. Such large disk dimensions were intended to allow for a smaller threshold strength of exciting field for core switching [10]. According to the fact that the eigenfrequencies of the $m = -1$ and $m = +1$ azimuthal modes vary with the H_z strength [26], we first examined those modes' eigenfrequency variation with H_z at 1 kOe intervals within the $H_z = -3 - +3$ kOe range. To find the eigenfrequency of the azimuthal modes, we applied a sinc-function field of $H_0 = 10$ Oe, $t_0 = 1$ ns and $\omega_H/2\pi = 50$ GHz during a period of 10 ns. Figure 5.6(a) shows the resultant FFTs of the temporal oscillations of $\langle m_x \rangle$ for different H_z values, indicating that the $m = -1$ and $m = +1$ modes' eigenfrequencies are largely split and are also varying with H_z . The H_z -versus-eigenfrequency curves (Fig. 5.6(b)) reveal their asymmetric concave-down shapes as well as smaller eigenfrequency splitting with increasing H_z . Such H_z -dependences originate from the modification of the vortex's magnetization configuration effected by application of H_z [26].

With the aforementioned information, we resonantly excited the individual $m = -1$ (+1) mode under H_z by applying a CW (CCW) circular-rotating field of $H_0 = 30$ Oe and the corresponding resonant frequencies. Figure

5.7 shows the x -, y -components and the displacement of the vortex-core position before the first core-reversal occurrences for the indicated values of $H_z = -1, 0$ and $+1$ kOe. Note that for the case of the $m = -1$ mode and $H_z = +1$ kOe with $H_0 = 30$ Oe, the core does not switch, because the exciting field strength $H_0 = 30$ Oe is smaller than its threshold value, ~ 45 Oe. The other cases in Fig. 5.7 correspond to core switching after the relevant core gyrations. The asymmetric $m = -1$ and $m = +1$ modes show contrasting maximum orbit radii $|\mathbf{X}|_{\max}$, 13.9 and 14.3 nm at $H_z = 0$, respectively. However, for the two modes, $|\mathbf{X}|_{\max}$ increases up to 14.6 and 17.7 nm at $H_z = +1$ kOe and decreases to 12.1 and 12.3 nm at $H_z = -1$ kOe, respectively, indicating that $|\mathbf{X}|_{\max}$ is proportional to H_z .

From the temporal evolution of v , h_z , and $m_{z,\text{dip}}$ for the different H_z values, as shown in Fig. 5.8, we also found that all of the core switching occurs when $m_{z,\text{dip}}$ reaches $-p$, regardless of H_z . However, as indicated by the horizontal dashed lines in Fig. 5.8, the threshold values of v and $|h_z|$ (noted as v_{\max} and $|h_z|_{\max}$, respectively), similarly to the gyrotropic-mode case, generally increase with increasing H_z , though they do not show the monotonic relation, due to the complex nonlinear interaction in the azimuthal-modes-driven core switching [6-8]. In Fig. 5.9, the v_{\max} and $|h_z|_{\max}$ values are plotted as a function of H_z for different H_0 values. It is found that H_0 almost does not affect the v_{\max} and $|h_z|_{\max}$ values for the given mode and H_z , and that both values can be reduced with further negative values of H_z . This remarkable reduction in both

v_{\max} and $|h_z|_{\max}$ is due to the H_z -dependence of the initial m_z level of the magnetization dip, as addressed in the following. For the gyrotropic mode, the v_{\max} varies as

$$v_{\max} / v_{\max}^0 = (\rho / \rho_0) |\Delta m_z|, \quad (5.1)$$

where ρ is the core radius under H_z , and v_{\max}^0 and ρ_0 are the v_{\max} and ρ at $H_z = 0$ kOe, respectively [22]. Here we note that $|\Delta m_z| = |-p - m_z^g|$ [22]. The solid lines in Fig. 5.9 are the results of the numerical calculations of Eq. (5.1) for both azimuthal modes, and agree well with the simulation results.

The H_z -dependences of v_{\max} and $|h_z|_{\max}$ shown above imply that the essential parameters for faster recording and lower power-consumption memory storage can be manipulated by the strength and direction of H_z . Figures 5.10(a) and 5.11(a) compare the remarkable asymmetries in the switching time t_{sw} and the threshold field strength H_0^{th} between the $m = -1$ and $m = +1$ modes, relative to those values for the gyrotropic mode excitation. As seen in the left panel of Fig. 5.10(b), since the v of the vortex core's gyration is proportional to the angular eigenfrequency ω of the gyration, both v_{\max} and ω are proportional to H_z . Thus, for the case of the gyrotropic mode, both v_{\max} and ω influences t_{sw} , so that t_{sw} can be almost constant versus H_z . By contrast, for both azimuthal modes, t_{sw} drastically varies with H_z for the given H_0 values. At $H_z = -3$ kOe, for example, t_{sw} decreases to about 80 (30) % with

respect to the value at $H_z = 0$ for the $m = -1$ (+1) mode (see the middle and right panels of Fig. 5.10(a)), because the variations of the ω 's of the $m = -1$ and $m = +1$ modes are relatively much smaller than those of the gyrotropic mode. As shown in Fig. 5.10(b), for the gyrotropic-mode case, the eigenfrequency decreases to $\sim 30\%$ at $H_z = -3$ kOe, whereas for the $m = -1$ and $m = +1$ modes, the eigenfrequencies decrease only to ~ 12 and $\sim 4\%$, respectively. As a result, the t_{sw} increases with increasing H_z , as shown in the middle and right panels of Fig. 5.10(a). These results establish that t_{sw} for the azimuthal-modes-driven core switching is controllable with H_z , which behavior has not been observed in gyrotropic-mode-driven core switching.

We also obtained the H_z -dependence of H_0^{th} , as shown in Fig. 5.11(a), because the smaller the H_0^{th} , the lower the power consumption in core switching. H_0^{th} can be further reduced owing to the reduction of the $|h_z|_{\text{max}}$ necessary for the core reversals, when the initial ground level m_z^g is closer to the criterion $m_{z,\text{dip}} = -p$. Since m_z^g becomes more negative with increasing negative H_z , as seen in Fig. 5.5(c), the $|h_z|_{\text{max}}$ also can be reduced by applying negative H_z , as shown in Fig. 5.11(b). In this work, drastic reduction of H_0^{th} for all of the modes were obtained with a negative H_z value, which is to say, for the case where the H_z direction is antiparallel with the initial core magnetization. This means that more efficient core switching can be achieved by controlling m_z^g and $|h_z|_{\text{max}}$ by applying H_z for azimuthal-modes-driven core switching.

Therefore, in the technological aspect, faster and lower power consumption can be obtained by applying a sufficiently strong perpendicular field that is opposite to the core magnetization. Such a perpendicular field effect also can be obtained by using underlayer thin films of strong perpendicular magnetic anisotropy.

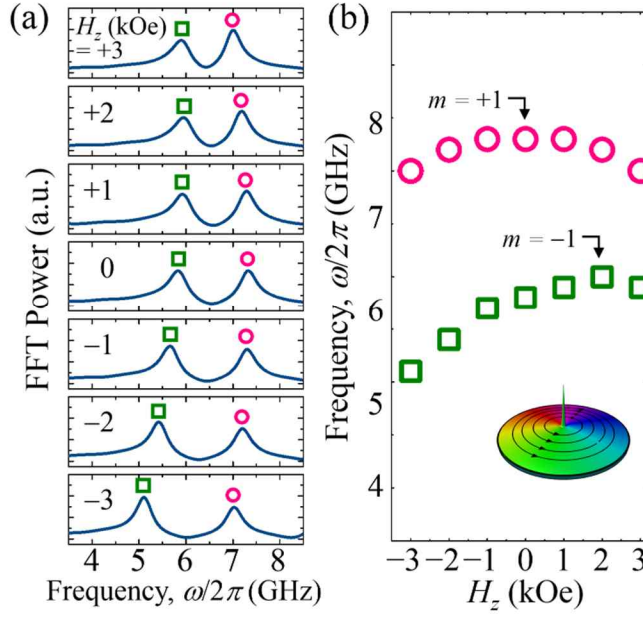


Fig. 5.6. (a) FFT power spectra for different H_z values. The green squares and red circles indicate the eigenfrequencies of the $m = -1$ and $m = +1$ modes, respectively. (b) Eigenfrequencies of $m = -1$ and $m = +1$ modes as a function of H_z . The inset shows the initial ground state of a Py disk of diameter $2R = 1200$ nm and thickness $L = 40$ nm.

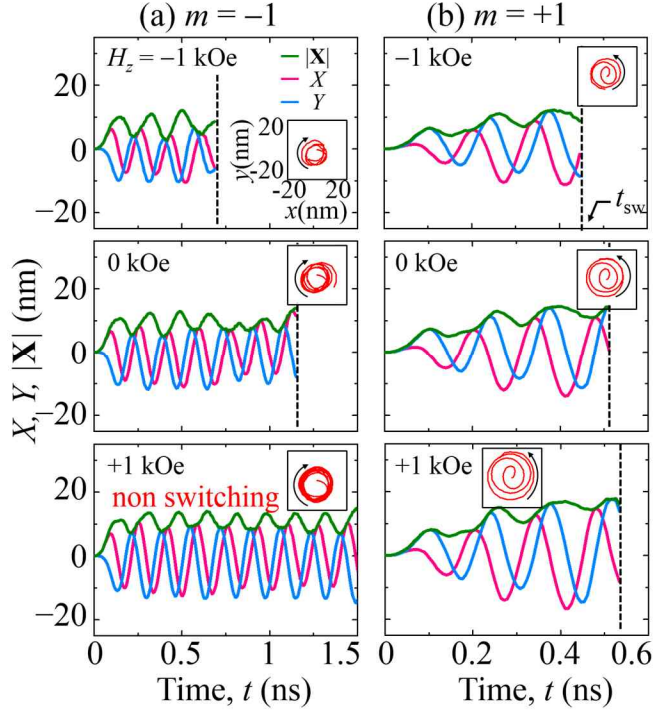


Fig. 5.7. Comparison of vortex-core gyrations driven by (a) $m = -1$ and (b) $m = +1$ azimuthal modes under indicated different H_z values: trajectories (inset) and oscillations of x - and y -components and displacements of vortex-core positions from disk center just before core-switching event. The vertical dashed lines indicate the switching time t_{sw} at which core-reversal events occur. In the case of $H_z = 1$ kOe with the $m = -1$ mode excitation, core switching does not take place.

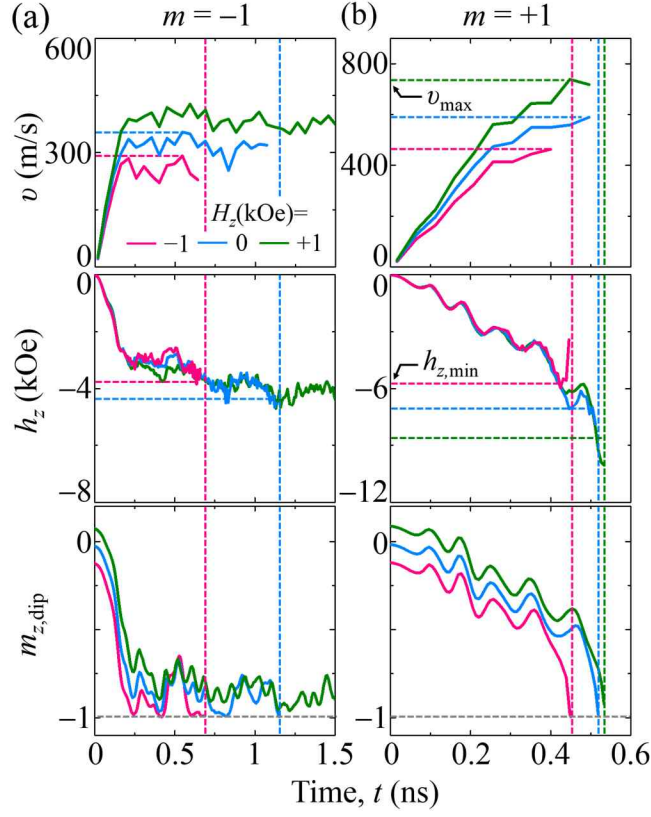


Fig. 5.8. Comparison of vortex-core motion speed v , associated gyrofield h_z , and m_z component of the magnetization dip, as obtained from (a) $m = -1$ and (b) $m = +1$ mode-resonant excitations with $H_0 = 30$ Oe for application of different H_z values, here $H_z = -1, 0, +1$ kOe. The horizontal dashed lines indicate the maximums of v , $|h_z|$, and $|m_{z,\text{dip}}|$. The vertical dashed lines indicate the switching time t_{sw} , defined as the moments at which core-reversal events occur.

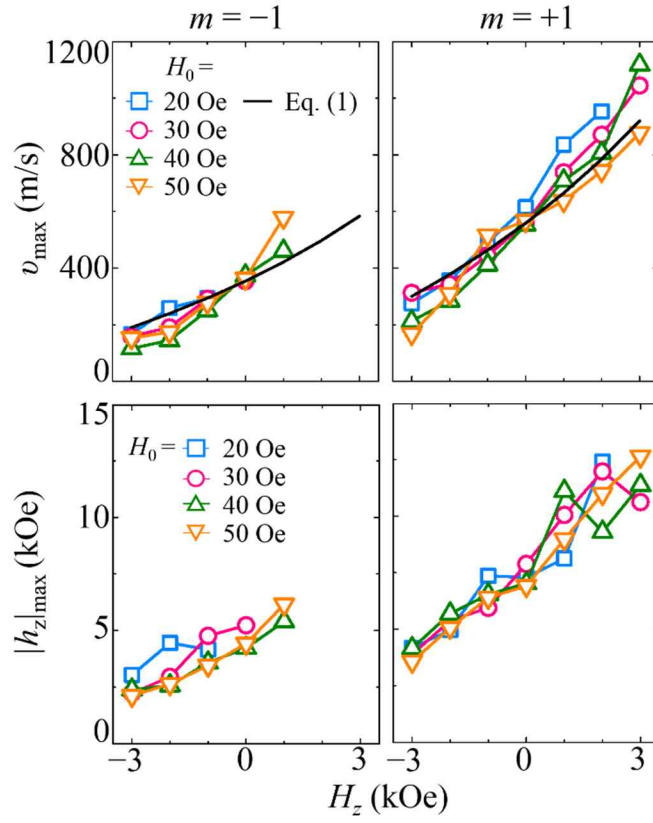


Fig. 5.9. The H_z -dependence of the v_{\max} and $|h_z|_{\max}$ values for the $m = -1$ and $+1$ azimuthal-modes-driven core switching for the indicated different values of resonant exciting field strength H_0 . The black solid lines shown in the v_{\max} versus H_z indicate the analytic calculation of Eq. (5.1).

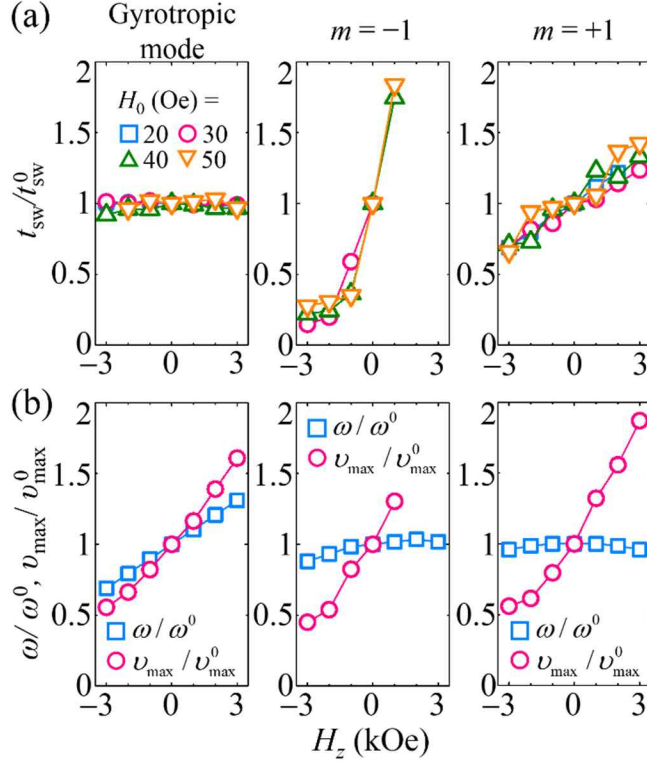


Fig. 5.10. (a) Normalized switching time t_{sw}/t_{sw}^0 for different H_z values, which reversals occur through resonant excitations of the gyrotropic mode and $m = -1$ and $+1$ azimuthal spin-wave modes with different rotating field strengths $H_0 = 20, 30, 40$ and 50 Oe. (b) H_z -dependence of normalized eigenfrequency ω/ω^0 and threshold core-motion speed v_{max}/v_{max}^0 for core switching by each mode-resonant excitation with $H_0 = 30$ Oe. Here we note that t_{sw}^0 , ω^0 and v_{max}^0 are the core-switching time, eigenfrequency and threshold core-motion speed at $H_z = 0$ kOe, respectively.

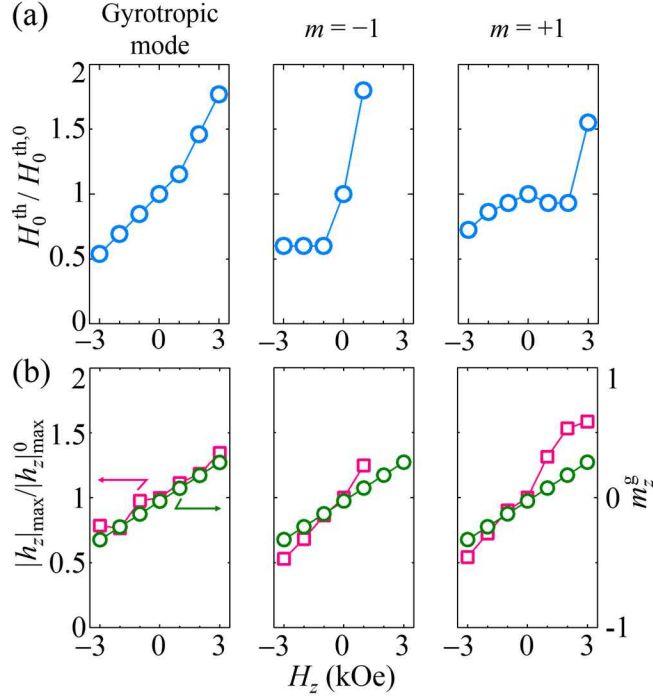


Figure 5.11. (a) H_z -dependence of normalized threshold field strength $H_0^{\text{th}} / H_0^{\text{th},0}$ for the resonant excitations of the gyrotropic mode, $m = -1$ and $+1$ azimuthal spin-wave modes. (b) Initial ground-state magnetization dip m_z^g and normalized maximum gyrofield strength $|h_z|_{\text{max}}^0 / |h_z|_{\text{max}}$ required for core switching with $H_0 = 30$ Oe. Here we note that $H_0^{\text{th},0}$ and $|h_z|_{\text{max}}^0$ are the threshold field strength and gyrofield strength at $H_z = 0$ kOe, respectively.

References

- [1] R. Hertel and C. M. Schneider, Physical Review Letters **97**, 177202 (2006).
- [2] B. Van Waeyenberge, A. Puzic, H. Stoll, K. W. Chou, T. Tyliczszak, R. Hertel, M. Fahnle, H. Bruckl, K. Rott, G. Reiss, I. Neudecker, D. Weiss, C. H. Back and G. Schutz, Nature **444**, 461 (2006).
- [3] K. S. Lee, K. Y. Guslienko, J. Y. Lee and S. K. Kim, Phys Rev B **76**, 174410 (2007).
- [4] A. Vansteenkiste, K. W. Chou, M. Weigand, M. Curcic, V. Sackmann, H. Stoll, T. Tyliczszak, G. Woltersdorf, C. H. Back, G. Schutz and B. Van Waeyenberge, Nature Physics **5**, 332 (2009).
- [5] V. P. Kravchuk, D. D. Sheka, Y. Gaididei and F. G. Mertens, J Appl Phys **102**, 043908 (2007).
- [6] M. Kammerer, M. Weigand, M. Curcic, M. Noske, M. Sproll, A. Vansteenkiste, B. Van Waeyenberge, H. Stoll, G. Woltersdorf, C. H. Back and G. Schuetz, Nature Communications **2**, 279 (2011).
- [7] M. Sproll, M. Noske, H. Bauer, M. Kammerer, A. Gangwar, G. Dieterle, M. Weigand, H. Stoll, G. Woltersdorf, C. H. Back and G. Schutz, Applied Physics Letters **104**, 012409 (2014).
- [8] H. G. Bauer, M. Sproll, C. H. Back and G. Woltersdorf, Physical Review Letters **112**, 077201 (2014).
- [9] M. Kammerer, H. Stoll, M. Noske, M. Sproll, M. Weigand, C. Illg, G. Woltersdorf, M. Fahnle, C. Back and G. Schutz, Phys Rev B **86**, 134426 (2012).
- [10] M. Noske, A. Gangwar, H. Stoll, M. Kammerer, M. Sproll, G. Dieterle, M.

Weigand, M. Fahnle, G. Woltersdorf, C. H. Back and G. Schutz, Phys Rev B **90**, 104415 (2014).

[11] <http://math.nist.gov/oommf>.

[12] L. D. Landau and E. M. Lifshitz, Phys. Z. Sowjetunion **8**, 153 (1935).

[13] T. L. Gilbert, Ieee T Magn **40**, 3443 (2004).

[14] K. S. Lee and S. K. Kim, Phys Rev B **78**, 014405 (2008).

[15] The field frequencies are somewhat different from those shown in Fig. 5.1(b). We chose the resonant frequencies at which the threshold field strength H_0 required for the core reversal driven by each mode excitation has its minimum value.

[16] K. Y. Guslienko, B. A. Ivanov, V. Novosad, Y. Otani, H. Shima and K. Fukamichi, J Appl Phys **91**, 8037 (2002).

[17] K. S. Lee, S. K. Kim, Y. S. Yu, Y. S. Choi, K. Y. Guslienko, H. Jung and P. Fischer, Physical Review Letters **101**, 267206 (2008).

[18] K. Yamada, S. Kasai, Y. Nakatani, K. Kobayashi, H. Kohno, A. Thiaville and T. Ono, Nature Materials **6**, 269 (2007).

[19] K. Y. Guslienko, K. S. Lee and S. K. Kim, Physical Review Letters **100**, 027203 (2008).

[20] V. P. Kravchuk, Y. Gaididei and D. D. Sheka, Phys Rev B **80**, 100405 (2009).

[21] We conducted further micromagnetic simulations using the smaller cell size of $3 \times 3 \times 4 \text{ nm}^3$. The maximum velocities of core gyrations were estimated to be ~ 350 and $\sim 876 \text{ m/s}$ for the $m = -1$ and $+1$ modes, respectively (compared

with ~ 370 and ~ 800 m/s obtained with the cell size of $1 \times 1 \times 20$ nm³). We concluded that in such thin-film dots, the maximum velocity of core gyration does not change with the number of cells divided in the thickness direction.

[22] M. W. Yoo, K. S. Lee, D. E. Jeong and S. K. Kim, Phys Rev B **82**, 174437 (2010).

[23] A. V. Khvalkovskiy, A. N. Slavin, J. Grollier, K. A. Zvezdin and K. Y. Guslienko, Applied Physics Letters **96**, 022504 (2010).

[24] G. de Loubens, A. Riegler, B. Pigeau, F. Lochner, F. Boust, K. Y. Guslienko, H. Hurdequint, L. W. Molenkamp, G. Schmidt, A. N. Slavin, V. S. Tiberkevich, N. Vukadinovic and O. Klein, Physical Review Letters **102**, 177602 (2009).

[25] Because the eigenfrequency of the gyrotropic mode changes with Hz, we also changed the field angular frequency according to Hz in this calculation.

[26] B. A. Ivanov and C. E. Zaspel, Physical Review Letters **94**, 027205 (2005).

Chapter 6

Gyrotropic Mode Driven Vortex Core Switching in Magnetic Half-spheres

6.1. Introduction

In the previous Chapters 5 and 6, we studied the magnetization-reversal dynamics in two-dimensional (2D) soft magnetic disks. One of the vortex-core-reversal mechanisms found thus far is the creation of a vortex-antivortex (V-AV) pair with magnetizations opposite to the initial core magnetization, followed by annihilation of the original core together with the newly formed antivortex [1-4]. This reversal mechanism can be achieved with low power consumption by resonant excitation of one of the vortex-gyration and azimuthal spin-wave modes. The annihilation process of V-AV pairs is in principle accompanied by an exchange-energy explosion and subsequent spin-wave emission. On the contrast, the radial spin-wave-mode-driven vortex-core reversals by perpendicularly oscillating magnetic fields have been found that represent the nucleation of a Bloch point at one surface of the disk, followed by its displacement along the thickness [5, 6].

However, those earlier studies were mainly restricted to 2D planar dots. Recent advances in nano fabrication technologies are now enabling fabrication of more complicated three dimensional (3D) nanostructures of a rich variety of shapes, such as spheres [7, 8], half-spheres [9] and spherical shells [10, 11]. In

addition, those 3D magnetic elements have attracted growing interest, due to their characteristic properties that originate from 3D curved geometries and their potential applications to memory devices.

We found, as reported in this chapter, a robust core-reversal mechanism either with or without simple chirality switching in soft magnetic half-spheres. In an excited gyrotropic mode, the original core is expelled from a given half-sphere, upon which two vortex cores of opposite polarizations are nucleated at different edges between the top and bottom surfaces. Then, one of those nucleated vortex cores remains while the other is expelled from the half-sphere. The core orientations that are nucleated are determined by the inward or outward in-plane magnetization direction at the nucleation sites near the edge. Notably, this robust magnetic soliton formation, as mediated by curved-surface geometrical confinements, is distinguished from the nucleation and annihilation processes of a V-AV pair or edge-soliton-mediated core-reversal process found in soft magnetic planar dots. Uniquely, this reversal mechanism provides a reliable and efficient means of controlling both the vortex core and chirality switching in media composed of periodic arrays of half-spheres.

6.2. Modeling

In the present study, we used a 3D model object, a half-sphere of diameter $2R = 100$ nm and height $h = R$ (see Fig. 6.1(a)). To explore the vortex-core-reversal dynamics of a given Permalloy (Py: $\text{Ni}_{80}\text{Fe}_{20}$) half-sphere of curved surfaces, micromagnetic numerical calculations using 3D finite element meshes are necessary. To that end, we discretized the curved surfaces into triangles of roughly equal area using Hierarchical Triangular Mesh (HTM) [12], thereby preventing irregularity-incurred numerical errors. The dynamic motions of the magnetizations of the individual nodes (mesh size: ~ 4 nm) at the zero temperature were solved using the FEMME code (version 5.0.8) [13], which incorporates the Landau-Lifshitz-Gilbert equation [14, 15]. The chosen Py material parameters were as follows: saturation magnetization $M_s = 8.6 \times 10^5$ A/m, exchange stiffness $A_{\text{ex}} = 1.3 \times 10^{-11}$ J/m, damping constant $\alpha = 0.01$, and zero magnetocrystalline anisotropy.

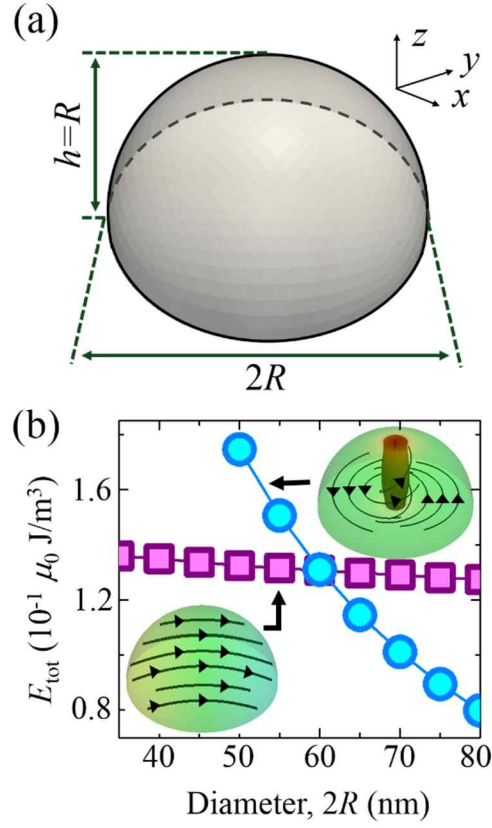


Fig. 6.1. (a) Model geometry of half-sphere of diameter $2R = 100$ nm and $h = 50$ nm. (b) Magnetic energy density versus diameter $2R$ for two possible onion and vortex states. For half-spheres of $2R > 60$ nm, a vortex state with upward core magnetization and CCW in-plane curling magnetization is formed in its ground state.

6.3. Results and Discussion

6.3.1. Eigenmodes in a Magnetic Half-spheres

First, we searched for ground states energetically stable in half-spheres of given diameter $2R$ (with $h = R$) by comparing the total magnetic energy densities E_{tot} of two possible onion and vortex states versus $2R$, as shown in Fig. 6.1(b). The onion and vortex states were obtained through free relaxation from the magnetization saturation in the $+x$ - and $+z$ -directions, respectively. Figure 6.1(b) reveals that for half-spheres of $2R \leq 60$ nm, the onion state is more stable than the vortex state, whereas for cases of $2R > 60$ nm, vortex configurations are favorable. Next, in order to search for all of the eigenmodes excited in half-spheres having only vortex ground states, we chose a half-sphere of dimensions $2R = 100$ nm and $h = R = 50$ nm. Then, we applied a sinc-function field along the x -axis, $H\hat{\mathbf{x}}$, where $H = H_0 \sin[2\pi f_H(t - t_0)] / [2\pi f_H(t - t_0)]$ with $H_0 = 1$ Oe, $f_H = 50$ GHz, and $t_0 = 1$ ns for a period of $t = 10$ ns. From fast Fourier transformations (FFTs) of the oscillations of the x component of magnetizations averaged over the volume of the half-sphere, $\langle m_x \rangle = \langle M_x \rangle / M_s$, a power spectrum in the frequency domain was obtained, as shown in Fig. 6.2(a). The four distinct peaks were found at 1.5, 5.4, 11.3 and 14.8 GHz, which are indicative of all of the individual eigenmodes excited in the given half-sphere. To identify the individual peaks' origins, we also obtained the corresponding FFT-power spatial distributions of the local m_x , as shown in Fig. 6.2(b). The first (1.5 GHz)

and second (5.4 GHz) peaks correspond to the zeroth- and first-order gyrotropic modes, where the node numbers are $n = 0$ and $n = 1$, respectively, along the height axis (here the z -axis) [16-22]. The FFT power profiles along the z -axis posited at $x = 0$ and $y = 0$ clearly show the position and number of nodes, as denoted by the red-color arrows. Here we note that the 50 nm height in the model is not sufficient to allow for additional higher-order gyrotropic modes that reportedly had been found in a thick cylindrical dot.²² In addition to the zeroth- and first-order gyrotropic modes in the half-sphere, two different azimuthal spin-wave modes were found at 11.3 and 14.8 GHz, corresponding to the $m = -1$ and $m = +1$ eigenmodes [23-25], respectively, where m is the number of nodes of the azimuthal spin waves in the azimuthal direction, and the $- (+)$ sign of m denotes the CW (CCW) rotation sense of the azimuthal spin waves for the upward core magnetization.

In order to more clearly identify the aforementioned individual eigenmodes, we resonantly excited them by applying in-plane oscillating magnetic fields along the x -axis, $H\hat{\mathbf{x}} = H_0 \sin(2\pi f_H t) \hat{\mathbf{x}}$, with a sufficiently high field amplitude, $H_0 = 100$ Oe. The field frequency f_H was varied to the eigenfrequencies of the four different eigenmodes. The resultant simulations reveal vortex-core profiles, which are displayed in Fig. 6.3 according to the m_z values (denoted as the red-colored isosurface at $m_z = 0.9$) and the Δm_z components at the bottom flat surfaces, where $\Delta m_z = m_z(t) - m_z(0)$. Under resonant excitation using $f_H = 1.5$ GHz, the vortex core on the top curved surface is in large-amplitude motion in the counter-clockwise (CCW) rotation sense, as

induced by the zeroth-order gyrotropic mode with no node along the z axis. As emphasized earlier, the special advantage of this 3D numerical calculation is its provision of such 3D fine features. The single vortex core is vertically bending, indicating that the orbiting core radius is larger at the top curved surface than at the bottom flat surface (precisely, almost at the center of the bottom surface). The first-order gyration excited by $f_H = 5.4$ GHz characterizes the same CCW rotation sense, but, contrastingly, the core's oscillation is 180° out of phase between the top and bottom surfaces, thus yielding one node at $h/2$ along the z -axis [19-22].

Relative to the zeroth- and first-order gyrations, the $m = -1$ and $m = +1$ azimuthal spin-wave modes excited by $f_H = 11.3$ and 14.8 GHz, respectively, give rise to small-amplitude core motions on both the top curved and bottom flat surfaces. The core-gyration sense and frequency, however, coincide with those of the $m = -1$ and $m = +1$ azimuthal modes, indicating that the gyration motions are caused by the interaction between the azimuthal modes and the given core [26]. Note that for the case of the upward core, the $m = -1$ ($+1$) mode has the CW (CCW) rotation sense of the azimuthal spin waves. It is well known that in thin cylindrical dots, the first-order ($|m| = 1$) azimuthal modes are split into two different frequencies [23, 24, 27], which contrast according to the rotation sense of the azimuthal modes relative to the vortex polarization p (core orientation). Thus, the $m = \pm 1$ azimuthal modes induce contrasting core gyrations by their asymmetric interactions with a given core orientation.¹⁷ In the half-sphere, the asymmetric azimuthal modes can be recognized also by the

contrasting gyration motions, as shown in Fig. 6.2(b) and Fig. 6.3. For the $m = -1$ mode (11.3 GHz), the FFT power distribution in the core region is very similar to that of the zeroth-order gyrotropic mode. For the $m = +1$ mode (14.8 GHz) contrastingly, the FFT power profile at the core axis shows two distinguishable nodes, which profile looks similar to the FFT power distribution of the second-order gyrotropic mode found in thick cylindrical dots.

We also conducted further simulations on spherical caps with different contact angles [7, 9], as shown in Fig. 6.4(a). The contact angle θ is the angle between the normal vectors at the top and bottom surfaces. For spherical caps of $h < R$, θ is related to the ratio of the height to radius, $\delta = h/R$, as $\sin \theta = 2\delta / (1 + \delta^2)$. In given spherical caps, the competition between the dipolar and exchange interactions determines the corresponding magnetization configurations. For cases of $\theta < 30^\circ$, onion states without a single vortex core were obtained as ground states. By contrast, for cases of $\theta \geq 30^\circ$, a single magnetic vortex core, and the curling magnetization around it, was well formed. The contrasting core profiles for different values of θ are shown in Fig. 6.4(a). As θ decreases from $\theta = 90^\circ$, the m_z profile in the core region becomes uniform along the core axis; for $\theta = 30^\circ$, the m_z profile is close to that of cylindrical dots in a single-vortex state.

For spherical caps with a single vortex (i.e., within $90^\circ \geq \theta \geq 30^\circ$ range), we determined the variation of the eigenfrequencies of the individual modes, as shown in Fig. 6.4(b). For relatively small contact angles (i.e., $30^\circ \leq \theta < 60^\circ$),

only the zeroth-order gyrotropic mode and the two $m = \pm 1$ azimuthal spin-wave modes were observed. As shown in Fig. 6.4(c), for $\theta = 30^\circ$, the uniform FFT power distributions along the height axis for the three eigenmodes are similar to those in thin disks. Also, the three modes' eigenfrequencies increase with increasing θ and $\delta (= h/R)$, as indicated by the linear fits in Fig. 6.4(b). These trends are similar to that in thin cylindrical dots, wherein the eigenfrequencies of the zeroth-order gyrotropic mode $\omega_0^{0\text{th}}$ and $m = \pm 1$ azimuthal modes $\omega_0^{m=\pm 1}$ depend on δ and $\delta^{1/2}$, respectively [24, 28], because the exchange energy contribution is negligible in cases of thin dots. On the other hand, starting from $\theta = 60^\circ$ ($h = \sim 28.9$ nm), an additional first-order gyrotropic mode, as observed in thick cylindrical dots [19-22], starts to appear. In fact, for the first-order gyrotropic mode, the FFT power profiles along the core axis clearly show a distinct single-node appearance. The eigenfrequency of that mode decreases with further increasing θ and δ , as it is proportional to $1/h^2$ in thick cylindrical dots, because such higher-order modes are dominantly determined by the exchange interaction [20]. After the appearance of the first-order gyrotropic mode, the eigenfrequency of the zeroth-order gyrotropic mode increases slightly with increasing θ and δ , while those of the $m = -1$ and $+1$ modes slightly decrease; hence their maximum around $\theta = 60^\circ$. The reduction of the eigenfrequencies of the $m = \pm 1$ modes cannot be explained, by 2D theory, in terms of $\omega_0^{m=\pm 1} \propto h^{1/2}$ (Ref. [23, 24]). We assumed that this unexpected reduction of the azimuthal modes' frequency is caused by the appearance of the

first-order gyrotropic mode and its interaction with the azimuthal modes.

In studies of vortex-core dynamics, the application of perpendicular bias field H_z is known to be an efficient means of controlling dynamic parameters such as the gyro-constant G , due to the presence of a vortex core and the stiffness coefficient κ of the given potential [29, 30]. Thus, a fundamental understanding of the H_z dependence of the eigenmodes excited in half-spheres would be very useful in the above-addressed control of vortex-core gyration dynamics. Here then, we further explored the effect of H_z on all of the eigenmodes excited in a half-sphere of $2R = 100$ nm and $h = 50$ nm. In our simulations, we varied H_z within the $-2 \sim 3$ kOe range at intervals of 1 kOe. The positive (negative) sign of H_z corresponds to the field direction applied in the $+z$ ($-z$) direction, being parallel (antiparallel) to the core magnetization direction for the upward core. The m_z distributions on the cross-section of the half-sphere in the initial ground states under H_z ranging from -2 to $+2$ kOe are displayed in Fig. 6.5(a). These m_z images manifest a remarkable change of the core's magnetization with H_z . The region where the out-of-plane magnetizations are close to $m_z = +1$ is much larger for $H_z = +2$ kOe than for $H_z = -2$ kOe. Such core-magnetization variations can affect the individual excited eigenmodes. In thin-film cylindrical disks, the eigenfrequency of the zeroth-order gyrotropic mode is proportional to H_z , as expressed $\omega^{0\text{th}} = \omega_0^{0\text{th}}(1 + H_z / H_s)$ for the upward core,³² where $\omega_0^{0\text{th}}$ is the angular eigenfrequency at $H_z = 0$, and H_s is the field for saturation of a given system's magnetization.⁴² This linear dependence of $\omega^{0\text{th}}$ on H_z , can be simply

explained, on the basis of $\omega^{0\text{th}} = \kappa / G$ [16], by the H_z dependence of two dynamic parameters, $G = G_0(1 - H_z / H_s)$ and $\kappa = \kappa_0[1 - (H_z / H_s)^2]$ [29]. From further micromagnetic simulations, we also obtained the linear dependence of the eigenfrequency of the zeroth-order gyration mode on H_z with a slope of $\omega^{0\text{th}} / 2\pi$ of ~ 0.59 GHz/kOe in the half-sphere, as shown in Fig. 6.5(b), while the eigenfrequency of the first-order gyrotropic mode was proportional linearly to H_z , with a slope of ~ 0.39 GHz/kOe, which value is $\sim 34\%$ smaller than that of the zeroth-order gyration mode. Since the non-uniformity of the core m_z profile in the half-sphere increases with increasing H_z , the gap between the zeroth- and first-order gyration's eigenfrequencies decreases, although, in thick dots, those mode eigenfrequencies slightly increase with H_z and their gap is nearly constant, as reported in Ref. [19]. Unlike the linear dependence of the gyrotropic modes' frequency on H_z , the two azimuthal spin-wave modes are concave down in overall shape, owing to the H_z -induced out-of-plane component variations of the magnetizations [23, 24]. The frequency splitting between the $m = -1$ and $+1$ azimuthal spin-wave modes decreases with increasing H_z . These fine dynamic processes can be discovered only in 3D numerical calculations.

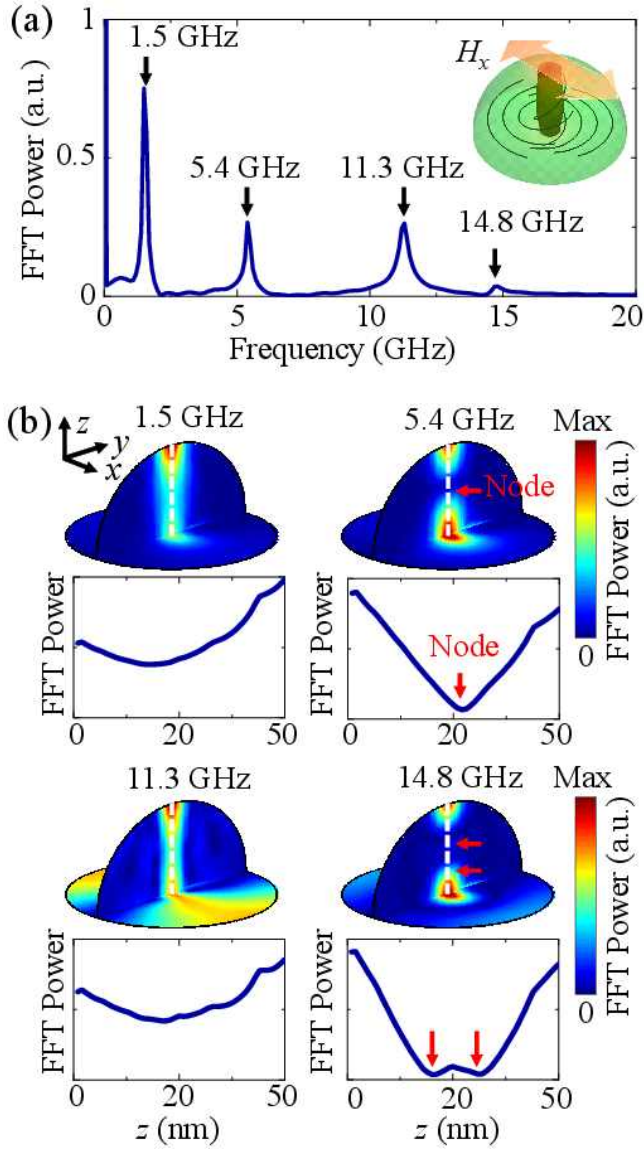


Fig. 6.2. (a) FFT power spectrum for characteristic excited modes in half-sphere of $2R = 100$ nm and $h = 50$ nm and spin configuration indicated in inset. (b) FFT power distributions of local m_z for four eigenmodes along with corresponding power profiles along z -axis positioned at $x = y = 0$. The nodes at the vortex-core axis are marked by the red arrows.

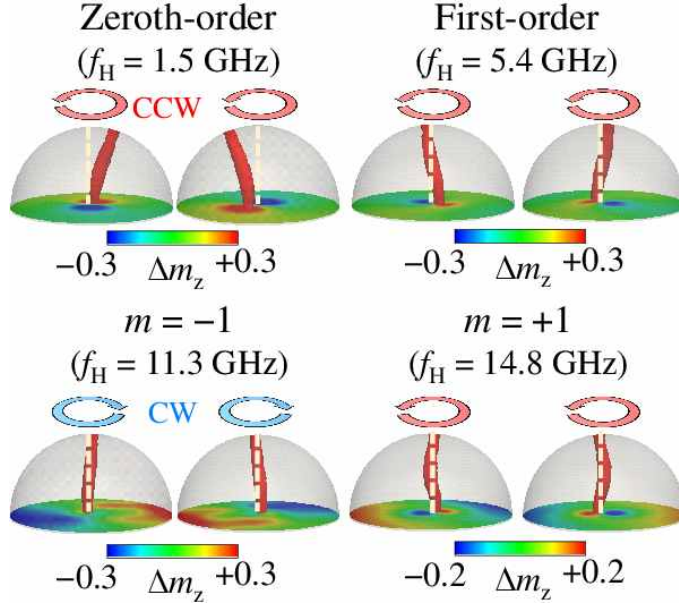


Fig. 6.3. Snapshot images of vortex-core motions by resonant excitations of individual modes. The red pillars are displaced by the isosurface at $m_z = 0.9$. The red and blue wide arrows above each half-sphere indicate the rotation senses of the vortex-core motions. The colors at the bottom surfaces represent the local values of $\Delta m_z = m_z(t) - m_z(0)$.

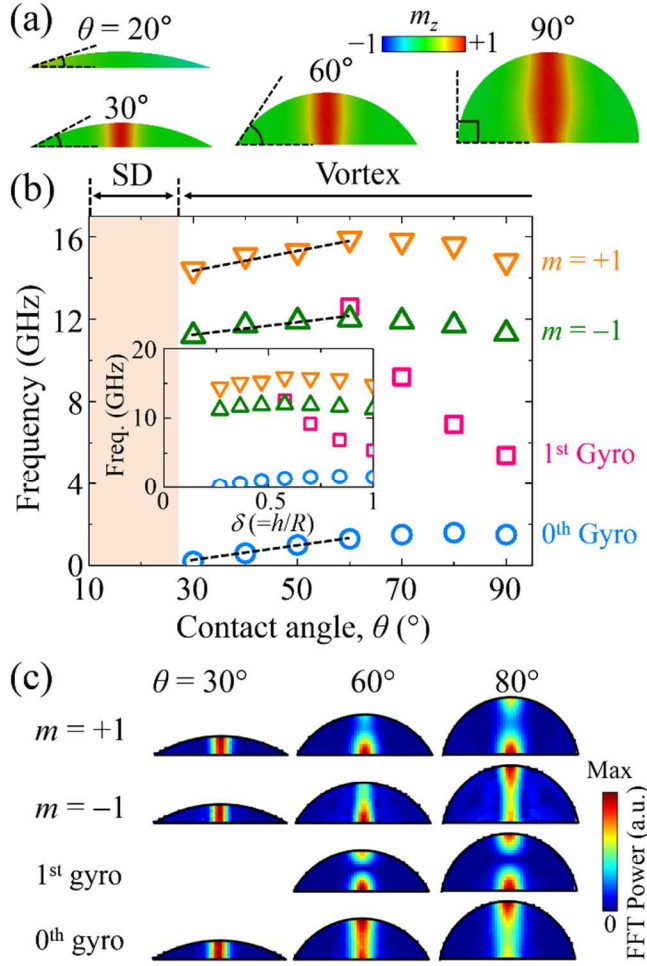


Fig. 6.4. (a) m_z components in core region on y - z plane in spherical caps of indicated contact angles θ . (b) θ - and δ -dependences of the eigenfrequencies of zeroth- and first-order gyrotropic modes and $m = -1$ and $+1$ azimuthal spin-wave modes. For the cases of $\theta < 30^\circ$, the vortex structure does not exist. The dashed lines represent linear fits to the data for $\theta \leq 60^\circ$. (c) FFT power distributions of local m_x at cross-section of spherical caps with different values of θ ($= 30^\circ, 60^\circ$ and 80°) for characteristic eigenmodes.

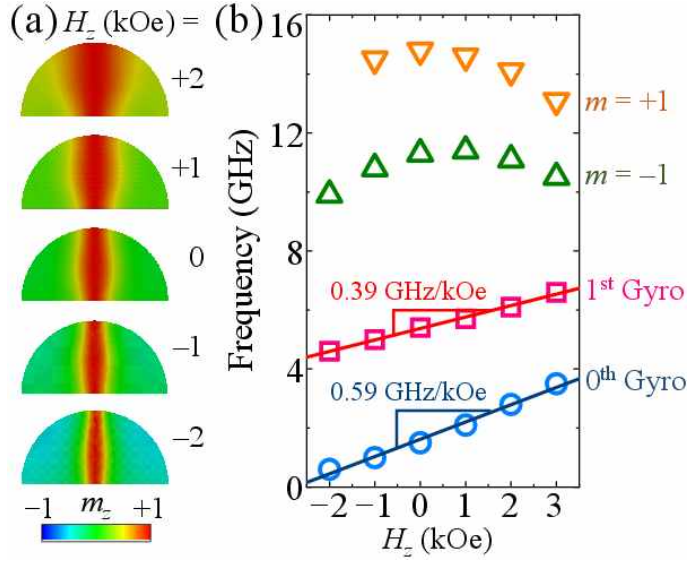


Fig. 6.5. (a) m_z components in half-sphere of $2R = 100$ nm and $h = 50$ nm on y - z plane for applications of indicated perpendicular fields. (b) Eigenfrequencies of zeroth- and first-order gyrotropic modes and $m = -1$ and $+1$ azimuthal spin-wave modes, obtained as function of H_z . The solid lines indicate linear fits to the corresponding data for the zeroth- and first-order gyrotropic modes.

6.3.2. Gyrotropic Mode Driven Vortex Core Switching

We investigated the vortex-core dynamics in the half-sphere driven by resonant excitation of the zeroth-order gyrotropic mode, which is one of excited modes in the half-sphere. First, to resonantly excite the gyrotropic mode, we applied CCW circular-rotating fields $\mathbf{H} = H_0[\cos(\omega_H t)\hat{\mathbf{x}} + \sin(\omega_H t)\hat{\mathbf{y}}]$ of field frequency $\omega_H / 2\pi$ and field amplitude H_0 (see Fig. 6.6(a)). The value of $\omega_H / 2\pi$ used equals the eigenfrequency of the gyrotropic mode, $\omega_0 / 2\pi = 1.5$ GHz. The applied value of $H_0 = 100$ Oe does not lead to core switching, because it is lower than the threshold field amplitude. We noted that clockwise (CW) rotational fields could not lead to switching of the upward core [31]. Core motions represented by the red-colored isosurface at $m_z = 0.9$ are displayed in Fig. 6.6(b).

The resultant trajectories of the resonantly excited gyration on the curved top and flat bottom surfaces are plotted in Fig. 6.7(a). The vortex-core position on the bottom surface was extracted by the maximum m_z value on the flat surface, while that on the top surface was extracted with the maximum value of $\mathbf{m} \cdot \hat{\mathbf{r}}$, $\hat{\mathbf{r}}$ being the unit vector normal to the local surface. Both the top and bottom trajectories show the same CCW rotation sense of the up-core gyration, with a large difference in their orbit radii. The orbit radius at the top surface is about two times larger than that at the bottom surface, consequently leading to the vertical core bending as noted above.

A further increase of H_0 , to 150 Oe, yields a core-reversal event. The trajectories of the vortex-core position on the curved top and flat bottom

surfaces are shown in Fig. 6.7(b). Comparing Figs. 6.7(a) and 6.7(b), it is clear that core-reversal events take place according to the field amplitude at a given resonant frequency. Figure 6.8(a) shows the core-switching events as a function of H_0 for the case of $\omega_H / 2\pi = 1.5$ GHz, represented by the maximum orbit radius ($|\mathbf{X}_t|_{\max}$) at the top surface. In a region of small H_0 values (i.e., < 150 Oe), $|\mathbf{X}_t|_{\max}$ monotonically increases with increasing H_0 , without any core-switching events. However, for cases of high H_0 values (i.e., ≥ 150 Oe), the core reaches the edge of the half-sphere (see Fig. 6.7(b)), and, immediately thereafter, its magnetization orientation is reversed. Here we note that the edge is the boundary between the top and bottom surfaces. Interestingly, along with the vortex polarization switching, another switching, that from the CCW to CW chirality, occurs in the specific range of $H_0 = 150 - 250$ Oe and at 325 Oe in the given H_0 range. Thus, above $H_0 = 150$ Oe, vortex polarization and chirality switching (marked in Fig. 6.8(a) by the circle symbols) or only-polarization switching (marked by the triangle symbols) takes place.

According to the results shown in Fig. 6.8(a), we further displayed vortex polarization and/or chirality switching versus both the frequency and amplitude of circular-rotating fields (Fig. 6.8(b)). In such a phase diagram, the minimum H_0 required for core switching is ~ 75 Oe at $\omega_H / 2\pi = \sim 1.7$ GHz, which value is not the same but close to $\omega_0 / 2\pi = 1.5$ GHz. An additional interesting feature, unlike the core-reversal dynamics in 2D cylindrical dots driven by circular-rotating fields, is the simultaneous switching of both the

chirality and polarization that occurs under some conditions, such as the fields above the dashed lines and under about $H_0 \sim 200$ Oe, as shown in Fig. 6.3(b). As reported of our earlier work, both polarization and chirality switching can occur in 2D cylindrical dots in cases where out-of-plane dc currents only of extremely high current density are applied [32].

In order to examine the difference and similarity of the underlying core switching mechanism, we plot details of the subprocesses of the polarization and chirality switching. Upon application of the rotating magnetic field, the original core (V_{CCW}^{\uparrow}) shows its gyration motion with increasing orbit radius ($t = 0 - 0.90$ ns). The core disappears at $t = 0.90$ ns when it reaches the half-sphere edge, resulting in a *C*-like magnetization configuration (see the images at $t = 0.93$ ns). At that moment, the exchange (E_{ex}) and magnetostatic energies (E_{ms}) are at the local minimum and maximum, respectively, as shown by the exchange and magnetostatic energy evolutions (see Fig. 6.9(b)). Then, at $t = 1.00 - 1.10$ ns, a new core of downward magnetization and CW chirality (V_{CW}^{\downarrow}) is nucleated in a different region opposite to the annihilation point, just after the original core is expelled from the half-sphere. However, at this moment, the overall chirality does not reverse (see the images at $t = 1.10$ ns). Immediately after the nucleation of the new downward core with CW chirality (V_{CW}^{\downarrow}) (i.e., at $t = 1.16$), another new vortex core, of upward magnetization and CCW rotation sense (V_{CCW}^{\uparrow}), starts to form. Thus, at this moment, there are two vortex cores of opposite polarization and chirality on the top surface (see the

image taken at $t = 1.25$ ns), resulting in the highest value of E_{ex} , and consequently reaching the maximum total energy. However, the new upward core is rapidly expelled to the opposite side ($t = 1.33$ ns), finally, only the downward core remains in the half-sphere with CW chirality ($V_{\text{CW}}^{\downarrow}$), and the polarization and chirality switching is completed. (see $t = 3.00$ ns). This core reversal is achieved with a relatively low field strength, ~ 100 Oe, for the case of $\omega_{\text{H}} \sim \omega_0$.

These subprocesses of “polarization plus chirality switching” in half-spheres are quite different from those of edge-soliton-mediated core reversals in cylindrical disks driven by out-of-plane dc currents; in this case, E_{ex} and E_{tot} drop markedly when the original core is expelled from the disks and the edge-soliton pair must overcome an E_{ex} barrier for formation of the reversed new core inside the disk.¹² By contrast, in the case of the half-sphere, such E_{ex} and E_{tot} drops by annihilation of the original core is not observed ($t = 0.93$ ns), because of the half-spheres’ geometrical characteristics. Both E_{ex} and E_{tot} reach their maximum values when two opposite vortex cores are formed inside the half-sphere; thus they are of extremely high energies, as shown in Fig. 6.9(b). Additionally, the origin of the formation of new cores’ orientation also differs from the case of edge-soliton-mediated core switching, wherein the core orientation is determined by the gyrofield at the nucleation site. By contrast, in the case of half-spheres, the magnetization direction at the nucleation site results, due to their geometrical characteristics, in the nucleated core’s orientation: the inward ($\mathbf{m} \cdot \hat{\mathbf{r}} \sim -1$, marked as ‘p1’ in Fig. 6.9(a)) and outward

($\mathbf{m} \cdot \hat{\mathbf{r}} \sim +1$, marked as ‘p2’) magnetization directions at the edge correspond to the nucleation points of the downward and upward magnetization cores, respectively, in order to reduce the energy barrier to vortex-core formation. Thus, in the case of half-spheres, new vortex cores are always formed at those points where the condition of $|\mathbf{m} \cdot \hat{\mathbf{r}}| \sim 1$ is satisfied, and the formation of new cores is not caused by gyrofields, but rather by the magnetization direction at the edge of the half-spheres, which mechanism is driven by a specific nano-scale geometrical confinement. These fine dynamic processes can be revealed only by 3D numerical calculations.

We also found that, in contrast to the above switching mechanism, multiple chirality switching added to the polarization switching can take place under the $H_0 > \sim 200$ Oe condition, as shown in Fig. 6.8(b). Figure 6.10 provides an example of the switching at $\omega_H / 2\pi = 1.5$ GHz and with $H_0 = 300$ Oe. The overall switching mechanism is almost the same as that of polarization plus chirality switching, except for the inclusion of subprocesses ⑤ and ⑥, as shown in Fig. 6.5. As in the case of the polarization plus chirality switching, we observed an additional nucleation of the downward core with opposite chirality (V_{CCW}^\downarrow), after which the earlier V_{CW}^\downarrow was expelled from the half-sphere, and finally, the V_{CCW}^\downarrow remained as a new core without switching of the original CCW chirality (compare $t = 3.00$ ns in Fig. 6.9(a) and 5(a)). In the case of only-polarization switching, the reversal process is more complex than that

in polarization plus chirality switching in the $H_0 < \sim 200$ Oe region, though the mechanisms of all of the formations of the newly formed core's magnetization at the edge are the same as those shown in Fig. 6.9. Here we note that the reversal process in Fig. 6.10 is an example of the only-polarization reversal mechanism for reversal cases by $H_0 > \sim 200$ Oe; for reversal processes by relatively high H_0 values, it is difficult to predict if chirality switching occurs or not, because of multiple chirality switching and complex nonlinear effect. However, from a technological point of view, the only-polarization reversal mechanism is also important, because each vortex state, that is, of polarity and chirality, can be switched to any of the other states through two different processes of “polarization plus chirality switching” and “only-polarization switching” or their combinations, as is similar to the case of out-of-plane-current-controlled switching in 2D cylindrical dots [32]. As further study, it is necessary to find a way to prohibit such multiple chirality switching or manipulate one-time switching to obtain another designated chirality.

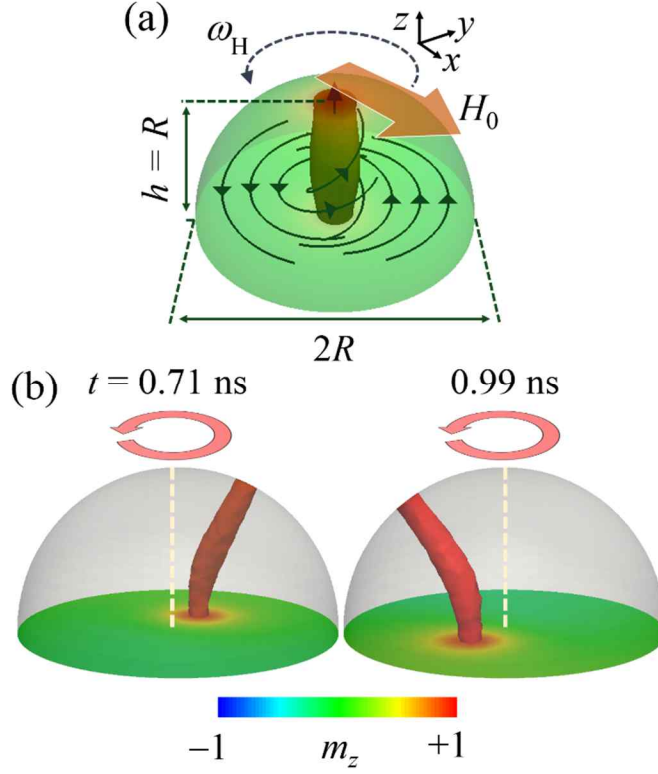


Fig. 6.6. (a) Model geometry of half-sphere of diameter $2R = 100$ nm and $h = 50$ nm, having vortex state of upward core magnetization and CCW in-plane curling magnetization in ground state. (b) Snapshot images of vortex-core motion by resonant excitation of a gyration mode using circular-rotating field of CCW rotation sense, $\mathbf{H} = H_0[\cos(\omega_H t)\hat{\mathbf{x}} + \sin(\omega_H t)\hat{\mathbf{y}}]$ with $H_0 = 100$ Oe and $\omega_H/2\pi = 1.5$ GHz at the indicated times. The red pillars are displaced by the isosurface of $m_z = 0.9$, and the red arrows above each half-sphere indicate the rotation senses of the vortex-core motion. The colors at the bottom surfaces represent the local m_z distributions.

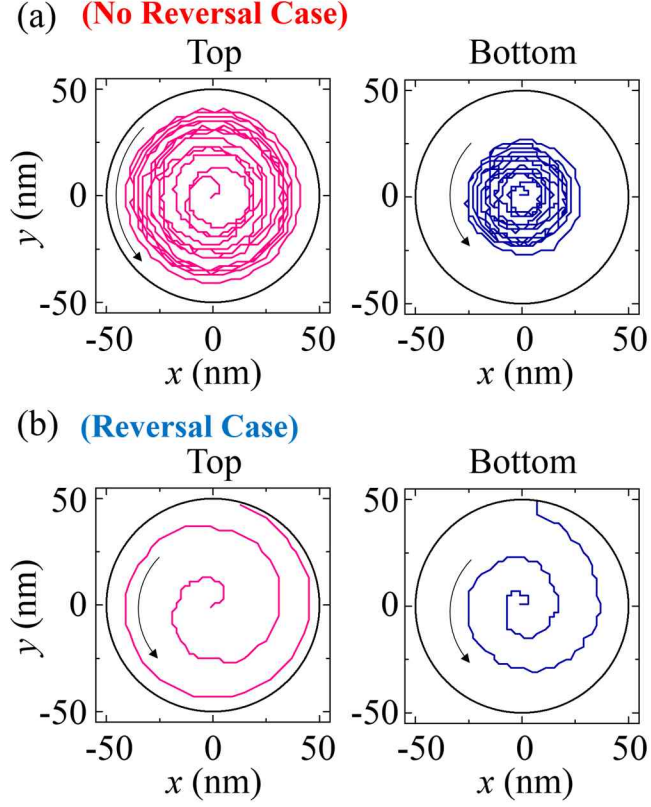


Fig. 6.7. (a) Trajectories of vortex-core motions at top curved (left) and bottom flat (right) surfaces, excited resonantly by circular-rotating field of (a) $[H_0, \omega_H/2\pi] = [100 \text{ Oe}, 1.5 \text{ GHz}]$ and (b) $[150 \text{ Oe}, 1.5 \text{ GHz}]$, where $\omega_H/2\pi = 1.5 \text{ GHz}$ equals gyrotropic-mode eigenfrequency. The core orientation is switched by $H_0 = 150 \text{ Oe}$ but not by $H_0 = 100 \text{ Oe}$.

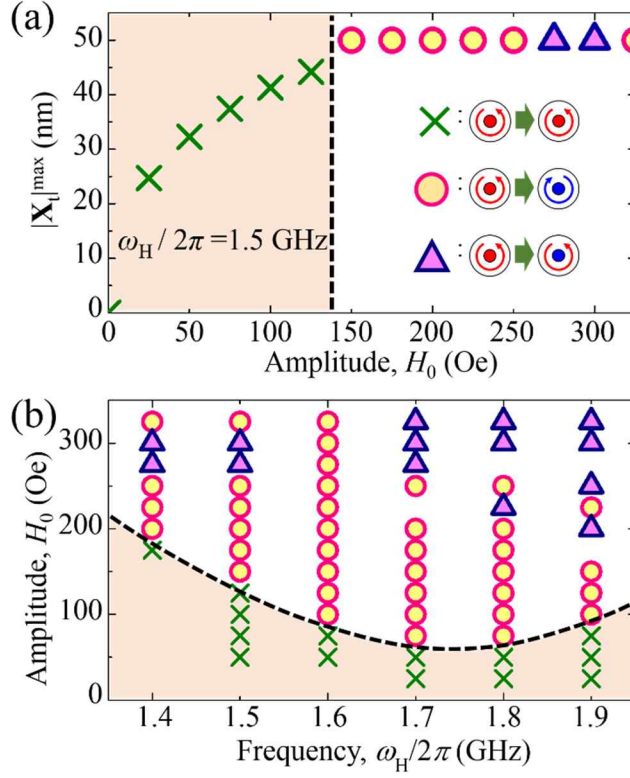


Fig. 6.8. (a) Dependence of maximum displacement $|X_t|_{\max}$ of core position on top surface on rotating-field amplitude H_0 (with resonant field frequency $\omega_H / 2\pi = 1.5$ GHz). The crosses, circles and triangles represent the values for non-switching, polarization plus chirality switching and only-polarization switching, respectively. (b) Phase diagram of polarization and chirality switching events with respect to both H_0 and $\omega_H / 2\pi$. In (a) and (b), the shaded regions correspond to the non-switching cases. In (b), the dashed line is provided as a guide to the eye.

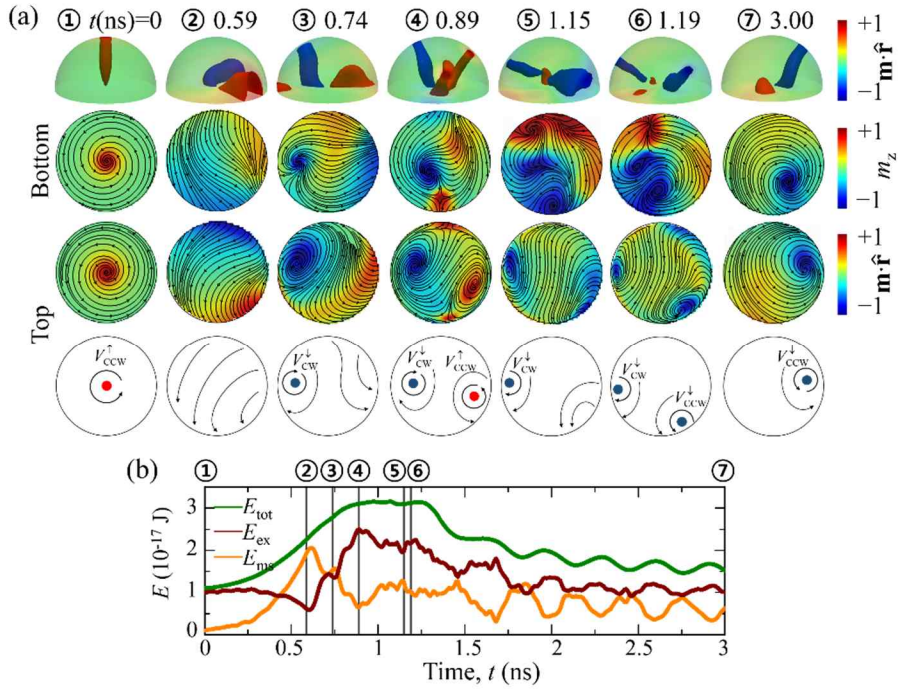


Fig. 6.10. Same as those in Fig. 6.9: only difference is circular-rotating field amplitude, $H_0 = 300$ Oe, for resonant excitation

References

- [1] R. Hertel and C. M. Schneider, Physical Review Letters **97**, 177202 (2006).
- [2] B. Van Waeyenberge, A. Puzic, H. Stoll, K. W. Chou, T. Tylliszczak, R. Hertel, M. Fahnle, H. Bruckl, K. Rott, G. Reiss, I. Neudecker, D. Weiss, C. H. Back and G. Schutz, Nature **444**, 461 (2006).
- [3] K. S. Lee, K. Y. Guslienko, J. Y. Lee and S. K. Kim, Phys Rev B **76**, 174410 (2007).
- [4] A. Vansteenkiste, K. W. Chou, M. Weigand, M. Curcic, V. Sackmann, H. Stoll, T. Tylliszczak, G. Woltersdorf, C. H. Back, G. Schutz and B. Van Waeyenberge, Nature Physics **5**, 332 (2009).
- [5] A. Thiaville, J. M. Garcia, R. Dittrich, J. Miltat and T. Schrefl, Phys Rev B **67**, 094410 (2003).
- [6] R. F. Wang and X. W. Dong, Applied Physics Letters **100**, 082402 (2012).
- [7] R. P. Boardman, H. Fangohr, S. J. Cox, A. V. Goncharov, A. A. Zhukov and P. A. J. de Groot, J Appl Phys **95**, 7037 (2004).
- [8] M. Ammar, M. LoBue, E. Snoeck, M. Hytch, Y. Champion, R. Barrue and F. Mazaleyrat, Journal of Magnetism and Magnetic Materials **320**, E716 (2008).
- [9] R. P. Boardman, J. Zimmermann, H. Fangohr, A. A. Zhukov and P. A. J. de Groot, J Appl Phys **97**, 10E305 (2005).
- [10] Q. L. Ye, Y. Kozuka, H. Yoshikawa, K. Awaga, S. Bandow and S. Iijima, Phys Rev B **75**, 224404 (2007).
- [11] R. Streubel, V. P. Kravchuk, D. D. Sheka, D. Makarov, F. Kronast, O. G. Schmidt and Y. Gaididei, Applied Physics Letters **101**, 132419 (2012).

- [12] A. S. Szalay, J. Gray, G. Fekete, P. Z. Kunszt, P. Kukol, and A. Thakar, Indexing the Sphere with the Hierarchical Triangular Mesh, (Microsoft, <http://arxiv.org/ftp/cs/papers/0701/0701164.pdf>, 2007).
- [13] D. Suess, and T. Schrefl, FEMME: Finite Element MicroMagnEtics 5.0.8 (SuessCo, <http://suessco.com/>).
- [14] L. D. Landau and E. M. Lifshitz, Phys. Z. Sowjetunion **8**, 153 (1935).
- [15] T. L. Gilbert, Ieee T Magn **40**, 3443 (2004).
- [16] K. Y. Gusliencko, B. A. Ivanov, V. Novosad, Y. Otani, H. Shima and K. Fukamichi, J Appl Phys **91**, 8037 (2002).
- [17] K. Y. Gusliencko, Applied Physics Letters **89**, 022510 (2006).
- [18] J. P. Park, P. Eames, D. M. Engebretson, J. Berezovsky and P. A. Crowell, Phys Rev B **67**, 020403 (2003).
- [19] F. Boust and N. Vukadinovic, Phys Rev B **70**, 172408 (2004).
- [20] J. J. Ding, G. N. Kakazei, X. M. Liu, K. Y. Gusliencko and A. O. Adeyeye, Scientific Reports **4**, 4796 (2014).
- [21] G. Lv, H. Zhang, X. C. Cao, F. Gao and Y. W. Liu, Applied Physics Letters **103**, 252404 (2013).
- [22] M. Yan, R. Hertel and C. M. Schneider, Phys Rev B **76**, 094407 (2007).
- [23] V. Novosad, M. Grimsditch, K. Y. Gusliencko, P. Vavassori, Y. Otani and S. D. Bader, Phys Rev B **66**, 052407 (2002).
- [24] B. A. Ivanov and C. E. Zaspel, Physical Review Letters **94**, 027205 (2005).
- [25] M. Buess, R. Hollinger, T. Haug, K. Perzlmaier, U. Krey, D. Pescia, M. R. Scheinfein, D. Weiss and C. H. Back, Physical Review Letters **93**, 077207

(2004).

[26] M. Kammerer, M. Weigand, M. Curcic, M. Noske, M. Sproll, A. Vansteenkiste, B. Van Waeyenberge, H. Stoll, G. Woltersdorf, C. H. Back and G. Schuetz, *Nature Communications* **2**, 279 (2011).

[27] A. A. Awad, K. Y. Gusliencko, J. F. Sierra, G. N. Kakazei, V. Metlushko and F. G. Aliev, *Applied Physics Letters* **96**, 012503 (2010).

[28] K. Y. Gusliencko, W. Scholz, R. W. Chantrell and V. Novosad, *Phys Rev B* **71**, 144407 (2005).

[29] G. de Loubens, A. Riegler, B. Pigeau, F. Lochner, F. Boust, K. Y. Gusliencko, H. Hurdequint, L. W. Molenkamp, G. Schmidt, A. N. Slavin, V. S. Tiberkevich, N. Vukadinovic and O. Klein, *Physical Review Letters* **102**, 177602 (2009).

[30] M. W. Yoo, K. S. Lee, D. S. Han and S. K. Kim, *J Appl Phys* **109**, 063903 (2011).

[31] K. S. Lee, Y. S. Yu, Y. S. Choi, D. E. Jeong and S. K. Kim, *Applied Physics Letters* **92**, 192513 (2008).

[32] Y. S. Choi, M. W. Yoo, K. S. Lee, Y. S. Yu, H. Jung and S. K. Kim, *Applied Physics Letters* **96**, 072507 (2010).

Chapter 7

Summary

In this thesis, we studied three different vortex core switching mechanism in soft magnetic nanoelements using excitations of the intrinsic eigenmodes.

Prior to investigate the core switching, we detected the $m = -1$ and $+1$ azimuthal and $n = 1$ radial spin-wave modes in the thin Permalloy nanodisks using the VNA-FMR technique. We also have conducted micromagnetic simulations and compared the results with our experimental data. Consequently, we have identified the azimuthal and radial spin-wave modes of the given system.

Next, we studied vortex-core reversals driven by excitations of the $m = -1$ and $m = +1$ azimuthal spin-wave modes, and interpreted the similarities and differences in the asymmetric spin-wave-mode-driven core reversals. Criterion for the core reversal is the magnetization dip that reaches $m_{z,\text{dip}} = -p$. To meet this criterion for core-reversal events, the threshold core-motion speed and perpendicular gyrofield that are variable for different core-switching mechanisms and controllable with externally applied perpendicular field H_z must be achieved. Here we also examined the effect of H_z on the switching time and threshold field strength required for the core reversals. These two essential parameters, calculated according to the strength and direction of H_z , are

presented as well. This work offers deeper insights into the azimuthal spin-wave driven core-reversal dynamics as well as an efficient means of controlling the azimuthal spin-wave modes and, thereby, the associated core reversals.

In the next chapter, we found an additional, efficient means of ultrafast vortex-core switching assisted by the resonance of radial-mode spin waves, which mechanism differs completely from the familiar vortex-antivortex-pair-mediated core switching. The core reversal reduces the maximized exchange energy that is introduced through the fluctuation of the magnetization dip around the core and the consequently narrowed core. The reversal process resonantly occurs with the help of radial-mode spin-wave excitations.

Finally, we studied the vortex-core-reversal dynamics of a 3D vortex structure in soft magnetic half-spheres using 3D micromagnetic numerical calculations. We discovered additional unknown mechanisms of vortex-core reversals. Finally, we observed fast core reversals along with chirality switching driven by resonant excitations of a gyrotropic mode, and then clarified the reversal process details according to the energy variations. The specific geometry of half-spheres affects the core-reversal mechanism. Such detailed 3D dynamic features, unobtainable from 2D numerical calculations, offer both additional details on and new underlying physics of vortex-core reversals in specific restricted geometries.

Publications

1	Y.-S. Choi, J.-Y. Lee, <u>M.-W. Yoo</u> , K.-S. Lee, K. Y. Guslienko, and S.-K. Kim, <i>Critical nucleation size of vortex core for domain wall transformation in soft magnetic thin film nanostrips</i> , Phys. Rev. B 80, 012402 (2009).
2	Y.-S. Choi, M.-W. Yoo, K.-S. Lee, Y.-S. Yu, H. Jung, and S.-K. Kim, <i>Out-of-plane current controlled switching of the fourfold degenerate state of a magnetic vortex in soft magnetic nanodots</i> , Appl. Phys. Lett. 96, 072507 (2010).
3	<u>M.-W. Yoo</u> , K.-S. Lee, D.-E. Jeong, and S.-K. Kim, <i>Origin, criterion, and mechanism of vortex-core reversals in soft magnetic nanodisks under perpendicular bias fields</i> , Phys. Rev. B 82, 174437 (2010).
4	<u>M.-W. Yoo</u> , K.-S. Lee, D.-S. Han, and S.-K. Kim, <i>Perpendicular-bias-field-dependent vortex-gyration eigenfrequency</i> , J. Appl. Phys. 109, 063903 (2011).
5	K.-S. Lee, <u>M.-W. Yoo</u> , Y.-S. Choi, and S.-K. Kim, <i>Edge-Soliton-Mediated Vortex-Core Reversal Dynamics</i> , Phys. Rev. Lett. 106, 147201 (2011).
6	Y.-S. Yu, K.-S. Lee, H. Jung, Y.-S. Choi, <u>M.-W. Yoo</u> , D.-S. Han, M.-Y. Im, P. Fischer, and S.-K. Kim, <i>Polarization-selective vortex-core switching by tailored orthogonal Gaussian-pulse currents</i> , Phys. Rev. B 83, 174429 (2011).

7	<u>M.-W. Yoo</u> , J. Lee, and S.-K. Kim, <i>Radial-spin-wave-mode-assisted vortex-core magnetization reversals</i> , Appl. Phys. Lett. 100, 172413 (2012).
8	Y.-S. Yu, D.-S. Han, <u>M.-W. Yoo</u> , K.-S. Lee, Y.-S. Choi, H. Jung, J. Lee, M.-Y. Im, P. Fischer, and S.-K. Kim, Resonant amplification of vortex-core oscillations by coherent magnetic-field pulses, Sci. Rep. 3, 1301; DOI:10.1038/srep01301 (2013).
9	M.-K. Kim, P. Dhak, H.-Y. Lee, J.-H. Lee, <u>M.-W. Yoo</u> , J. Lee, K. Jin, A. Chu, K. T. Nam, H. S. Park, S. Aizawa, T. Tanigaki, D. Shindo, M. Kim and S.-K. Kim, <i>Self-assembled magnetic nanospheres with three-dimensional magnetic vortex</i> , Appl. Phys. Lett. 105 , 232402 (2014).
11	<u>M.-W. Yoo</u> , J.-H. Lee and S.-K. Kim, Excited eigenmodes in magnetic vortex states of soft magnetic half-spheres and spherical caps, J. Appl. Phys. 116, 223902 (2014).
12	<u>M.-W. Yoo</u> , and S.-K. Kim, J. Appl. Phys. (in press).

Presentations in Conferences

[International Conferences]

1	<p>53rd Annual Conference on Magnetism and Magnetic Materials (MMM 2008), Texas, USA, Nov. 10 – 14, 2008.</p> <p>S.-K. Kim, Y.-S. Choi, J.-Y. Lee, and <u>M.-W. Yoo</u></p> <p>“Critical vortex core size required for nucleation of stable vortex or antivortex during domain wall motion in magnetic thin-film nanostripes”</p>
2	<p>Asian Magnetism Conference 2008 (AMC 2008), Busan, Korea, Dec. 10 – 13, 2008.</p> <p>S.-K. Kim, Y.-S. Choi, J.-Y. Lee, K. Y. Guslienko, K.-S. Lee, and <u>M.-W. Yoo</u></p> <p>“Universal Criterion for Formation of Stable Vortex or Antivortex in Domain Wall Motions in Magnetic Thin-film Nanostripes: Two Dimensional Soliton Model”</p>
3	<p>IEEE 7th International Symposium on Metallic Multilayers, Berkeley, USA, Sep. 19 – 24, 2010.</p> <p>Y.-S. Yu, K.-S. Lee, H. Jung, Y.-S. Choi, J.-Y. Lee, <u>M.-W. Yoo</u>, D.-S. Han, M.-Y. Im, P. Fischer, and S.-K. Kim</p> <p>“Lower-Power Consumption And Nonvolatile Vortex-Core Random Access Memory”</p>
4	<p>55th Annual Conference on Magnetism & Magnetic Materials (MMM 2010), Atlanta, USA, Nov. 14 – 18, 2010.</p> <p><u>M.-W. Yoo</u>, K.-S. Lee, D.-E. Jeong and S.-K. Kim</p> <p>“Reversal dynamics of magnetic vortex polarization in soft magnetic nanodots under perpendicular magnetic fields”</p>
5	<p>55th Annual Conference on Magnetism & Magnetic Materials (MMM 2010), Atlanta, USA, Nov. 14 – 18, 2010.</p> <p>K.-S. Lee, <u>M.-W. Yoo</u>, Y.-S. Choi, D.-E. Jeong, and S.-K. Kim</p> <p>“Exploring underlying physics of edge-soliton mediated vortex-core switching dynamics”</p>

6	<p>55th Annual Conference on Magnetism & Magnetic Materials (MMM 2010), Atlanta, USA, Nov. 14 – 18, 2010.</p> <p>Y.-S. Yu, K.-S. Lee, H. Jung, Y.-S. Choi, J.-Y. Lee, <u>M.-W. Yoo</u>, D.-S. Han, M.-Y. Im, P. Fischer, and S.-K. Kim</p> <p>“Unipolar Gaussian-Pulse Current Driven Vortex Core Switching in Cross-Point Architecture”</p>
7	<p>International Conference of AUMS (ICAUMS 2010), Jeju Island, Korea, Dec. 5 – 8, 2010.</p> <p>Y.-S. Choi, <u>M.-W. Yoo</u>, K.-S. Lee, Y.-S. Yu, H. Jung, and S.-K. Kim</p> <p>“Switching of vortex fourfold ground states by out-of-plane pulse currents”</p>
8	<p>International Conference of AUMS (ICAUMS 2010), Jeju Island, Korea, Dec. 5 – 8, 2010.</p> <p><u>M.-W. Yoo</u>, K.-S. Lee, D.-E. Jeong, and S.-K. Kim</p> <p>“Reversal Dynamics of Magnetic Vortex Polarization in Soft Magnetic Nanodots Under Perpendicular Magnetic Fields”</p>
9	<p>Moscow International Symposium on Magnetism 2011 (MISM 2011), Moscow, Russia, Aug. 20 – 25, 2011.</p> <p>S.-K. Kim, <u>M.-W. Yoo</u>, and Y.-S. Choi</p> <p>“Edge-soliton-mediated vortex-core reversal dynamics”</p>
10	<p>56th Annual Conference on Magnetism and Magnetic Materials (MMM 2011), Arizona, USA, Oct. 30 – Nov. 3, 2011.</p> <p><u>M.-W. Yoo</u>, J. Lee, and S.-K. Kim</p> <p>“Radial-spin-wave-mode-assisted vortex-core magnetization reversals”</p>
11	<p>56th Annual Conference on Magnetism and Magnetic Materials (MMM 2011), Arizona, USA, Oct. 30 – Nov. 3, 2011.</p> <p>Y.-S. Yu, K.-S. Lee, H. Jung, Y.-S. Choi, J.-Y. Lee, <u>M.-W. Yoo</u>, D.-S. Han, M.-Y. Im, P. Fischer, and S.-K. Kim</p> <p>“Reliable energy-efficient information recording by tailored orthogonal pulse currents in vortex-core cross-point architecture”</p>

12	<p>19th International Conference on Magnetism (ICM 2012), Busan, Korea, Jul. 8 – 13, 2012.</p> <p><u>M.-W. Yoo</u>, J. Lee, and S.-K. Kim</p> <p>“Switching dynamics of vortex cores in nanodots by azimuthal-spinwave-mode excitation”</p>
13	<p>19th International Conference on Magnetism (ICM 2012), Busan, Korea, Jul. 8 – 13, 2012.</p> <p>Y.-S. Yu, K.-S. Lee, H. Jung, Y.-S. Choi, D.-S. Han, <u>M.-W. Yoo</u>, M.-Y. Im, P. Fischer and S.-K. Kim</p> <p>“Energy-efficient control of vortex-core polarizations by tailored orthogonal pulse currents in cross-point architecture”</p>
14	<p>Magnonics 2013, Varberg, Sweden, Aug. 4 – 8, 2013.</p> <p><u>M.-W. Yoo</u>, and S.-K. Kim</p> <p>“Reversal dynamics of magnetic vortex cores by azimuthal spin wave excitation”</p>
15	<p>58th Annual Conference on Magnetism and Magnetic Materials (MMM 2013), Denver, USA, Nov. 4 – 8, 2013.</p> <p><u>M.-W. Yoo</u>, and S.-K. Kim</p> <p>“Reversal dynamics of single vortex core driven by azimuthal spin-wave-mode excitations in soft magnetic disk”</p>
16	<p>58th Annual Conference on Magnetism and Magnetic Materials (MMM 2013), Denver, USA, Nov. 4 – 8, 2013.</p> <p>J. Lee, <u>M.-W. Yoo</u>, D.-S. Han, H. Lee, and S.-K. Kim</p> <p>“Size-dependent resonant excitation of magnetic nano-sphere particles of three-dimensional magnetic vortex”</p>
17	<p>8th international conference on advanced materials and devices (ICAMD 2013), Jeju Island, Korea, Dec. 11 – 13, 2014.</p> <p>M.-K. Kim, H.-Y. Lee, K. Jin, P. Dhak, J.-H. Lee, <u>M.-W. Yoo</u>, J. Lee, A. Chu, M. Kim, K. T. Nam, and S.-K. Kim</p> <p>“Interacting magnetic nanoparticles of three dimensional magnetic vortex in geometrically different configurations”</p>

18	<p>8th international conference on advanced materials and devices (ICAMD 2013), Jeju Island, Korea, Dec. 11 – 13, 2014.</p> <p><u>M.-W. Yoo</u>, and S.-K. Kim</p> <p>“Reversal dynamics of single vortex core driven by azimuthal spin-wave-mode excitations in soft magnetic disk”</p>
19	<p>Skymag 2014, Paris, France, Apr. 9 – 11, 2014.</p> <p>J. Kim, D.-S. Han, <u>M.-W. Yoo</u>, and S.-K. Kim</p> <p>“Skyrmion quasi-crystals in dynamic transient states in soft magnetic nano-disks”</p>
20	<p>18th international microscopy congress (IMC 2014), Prague, Czech, Sep. 7 – 12, 2014.</p> <p>M.-K. Kim, H.-Y. Lee, K. Jin, P. Dhak, J.-H. Lee, <u>M.-W. Yoo</u>, J. Lee, A. Chu, M. Kim, K. T. Nam, and S.-K. Kim</p> <p>“Interparticle interactions for assemblies of magnetic nanoparticles with three-dimensional magnetic vortex”</p>
21	<p>The 3rd International Conference of AUMS (ICAUMS 2014), Haikou, China, Oct. 28 – Nov. 2, 2014.</p> <p>S.-K. Kim, <u>M.-W. Yoo</u>, J. Lee, and D.-S. Han</p> <p>“Dynamics of nanoscale soft magnetic spheres and half-spheres”</p>
22	<p>59th Annual Conference on Magnetism and Magnetic Materials (MMM 2014), Nov. 3 – 7, 2014.</p> <p><u>M.-W. Yoo</u>, J. Lee, and S.-K. Kim</p> <p>“Size-specific resonant excitation of soft magnetic nano-spheres of three dimensional magnetic vortex”</p>

[Domestic Conferences]

1	<p>한국자기학회 2010년도 하계학술연구발표회, Jun. 10 – 12, 2010.</p> <p>Y.-S. Yu, K.-S. Lee, H. Jung, Y.-S. Choi, J.-Y. Lee, <u>M.-W. Yoo</u>, D.-S. Han, M.-Y. Im, P. Fischer, and S.-K. Kim</p> <p>“Controlled vortex -core switching in micron-size Permalloy disks by orthogonal and unipolar Gaussian-pulse currents”</p>
2	<p>한국자기학회 2010년도 하계학술연구발표회, Jun. 10 – 12, 2010.</p> <p>Y.-S. Choi, <u>M.-W. Yoo</u>, K.-S. Lee, Y.-S. Yu, H. Jung, and S.-K. Kim</p> <p>“Controllable Switching of the Fourfold Ground State of a Magnetic Vortex in Nanodots by Out-of-Plane Currents”</p>
3	<p>한국자기학회 2011년도 하계학술연구발표회, Jun. 9 – 11, 2011.</p> <p>Y.-S. Yu, K.-S. Lee, H. Jung, Y.-S. Choi, <u>M.-W. Yoo</u>, D.-S. Han, M.-Y. Im, P. Fischer, and S.-K. Kim</p> <p>“Memory bit selection and recording by tailored pulse fields in vortex-core cross-point architecture”</p>
4	<p>한국자기학회 2011년도 하계학술연구발표회, Jun. 9 – 11, 2011.</p> <p><u>M.-W. Yoo</u>, J. Lee, and S.-K. Kim</p> <p>“Spin-wave radial-mode resonant vortex-core magnetization reversals”</p>
5	<p>한국자기학회 2011년도 하계학술연구발표회, Jun. 9 – 11, 2011.</p> <p>K.-S. Lee, <u>M.-W. Yoo</u>, Y.-S. Choi, and S.-K. Kim</p> <p>“Edge-soliton-mediated vortex-core reversal dynamics”</p>
6	<p>한국자기학회 2013년도 하계학술연구발표회, May 30 – Jun. 1, 2013.</p> <p><u>유명우</u>, 김상국</p> <p>“방위각 방향 스핀파를 이용한 자기소용돌이 핵 자화 반전에 대한 정량적 연구”</p>

7	<p>한국자기학회 2013년도 하계학술연구발표회, May 30 – Jun. 1, 2013.</p> <p>유영상, 한동수, <u>유명우</u>, 이기석, 최윤석, 정현성, 이제현, 임미영, Peter Fischer, 김상국</p> <p>“결맞은 자기펄스를 이용한 자기소용돌이 회전운동 증폭 방법 연구”</p>
8	<p>2013년도 대한금속·재료학회 추계학술대회, Oct. 24 – 25, 2013.</p> <p><u>유명우</u>, 김상국</p> <p>“Reversal Dynamics of Single Vortex Core Driven by Azimuthal Spin-wave-mode Excitations in Soft Magnetic”</p>
9	<p>한국자기학회 2013년도 동계학술연구발표회, Dec. 5 – 7, 2013.</p> <p><u>유명우</u>, 김상국</p> <p>“Reversal dynamics of single vortex core driven by azimuthal spin-wave-mode excitations in soft magnetic disk”</p>
10	<p>한국자기학회 2013년도 동계학술연구발표회, Dec. 5 – 7, 2013.</p> <p>M.-K. Kim, H.-Y. Lee, K. Jin, P. Dhak, J.-H. Lee, <u>M.-W. Yoo</u>, J. Lee, A. Chu, M. Kim, K. T. Nam, and S.-K. Kim</p> <p>“Interacting magnetic nanoparticles of three dimensional magnetic vortex in geometrically different configurations”</p>
11	<p>한국물리학회 2014년 봄학술논문발표회, Apr. 9 – 11, 2014.</p> <p>J. Kim, D.-S. Han, <u>M.-W. Yoo</u>, S.-K. Kim</p> <p>“Dynamic transient states of skyrmion in soft magnetic nano-disks”</p>
12	<p>한국물리학회 2014년 봄학술논문발표회, Apr. 9 – 11, 2014.</p> <p><u>M.-W. Yoo</u>, J. Lee, D.-S. Han, H. Lee, and S.-K. Kim</p> <p>“Dynamics of magnetic nano-spheres with a three-dimensional magnetic vortex”</p>

13	<p>한국물리학회 2014년 봄학술논문발표회, Apr. 9 – 11, 2014.</p> <p>M.-K. Kim, H.-Y. Lee, K. Jin, P. Dhak, J.-H. Lee, <u>M.-W. Yoo</u>, J. Lee, A. Chu, M. Kim, K. T. Nam, and S.-K. Kim</p> <p>“Building blocks for assembly of magnetic nanoparticles with three-dimensional magnetic vortex”</p>
14	<p>한국자기학회 2014년 하계학술논문발표회, May 29 – 31, 2014.</p> <p><u>M.-W. Yoo</u>, J. Lee, D.-S. Han, H.-Y. Lee and S.-K. Kim</p> <p>“Size-specific dynamic properties of magnetic nano-spheres with a three-dimensional magnetic vortex”</p>
15	<p>한국자기학회 2014년 하계학술논문발표회, May 29 – 31, 2014.</p> <p>M.-K. Kim, H.-Y. Lee, K. Jin, P. Dhak, J.-H. Lee, <u>M.-W. Yoo</u>, J. Lee, A. Chu, M. Kim, K. T. Nam, and S.-K. Kim</p> <p>“Vortex-state nanoparticles as building blocks of magnetic particle assembles”</p>
16	<p>한국자기학회 2014년 하계학술논문발표회, May 29 – 31, 2014.</p> <p>J. Kim, D.-S. Han, <u>M.-W. Yoo</u>, S.-K. Kim</p> <p>“Vortex quasi-crystal formation in dynamic transient states in soft magnetic nano-disks”</p>
17	<p>한국자기학회 2014년 동계학술논문발표회, Nov. 27 – 29, 2014.</p> <p>S.-K. Kim, <u>M.-W. Yoo</u>, and J.-H. Lee</p> <p>“Excited eigenmodes in soft magnetic half- and partspheres with three-dimensional magnetic vortex”</p>
18	<p>한국자기학회 2014년 동계학술논문발표회, Nov. 27 – 29, 2014.</p> <p>김보성, <u>유명우</u>, 이제현, 김상국</p> <p>“Vortex-core reversal dynamics at elevated temperatures”</p>

국문 초록

본 논문은 연자성 나노 물질에 형성된 자기소용돌이 구조와 자기소용돌이 핵의 초고속 자화 반전($< 1\text{ns}$)을 미소자기 전산모사를 통해 살펴보았다. 보다 빠르고 효율적인 핵 자화 반전을 위하여 2 차원 원반모양 자성박막에 존재하는 자기소용돌이 구조의 반지름 방향, 방위각 방향의 스핀과 모드를 이용하였다. 또한 3 차원의 반구 구조에서의 자기소용돌이 핵 자화 반전에 대해서도 살펴보았다.

우선 자기소용돌이 구조가 형성된 원반 평면에 수직방향으로 진동하는 교류자기장을 인가하여 자기소용돌이의 핵을 반전시켜 보았다. 이를 통해 우리는 인가 자기장의 진동수를 반지름방향 스핀과 모드의 고유진동수와 유사하게 맞출 경우 1ns 이내에 핵 자화 반전이 일어나며 핵 자화 반전을 위한 임계 자기장 세기가 수직방향 직류자기장을 이용하는 경우보다 10 배 가까이 감소하는 것을 확인하였다. 또한 이 때의 반전 메커니즘은 기존에 잘 알려진 소용돌이-반소용돌이에 의한 메커니즘과 전혀 다름을 확인하였다.

다음으로 선택적 핵 자화 반전을 위하여 방위각 방향의 스핀파를 이용하여 핵의 자화를 반전시키고 이 때 핵의 이동속도와 이에 의한 자이로필드(gyrofied), 그리고 핵 주변에 형성된 자기 웅덩이(magnetization dip)와의 관계를 살펴보았다. 그 결과 핵 자화 반전은 항상 자기 웅덩이가 $m_{z,\text{dip}} \sim -p$ 에 도달할 때 일어남을 확인할 수 있었다. 여기서 p 는 자기소용돌이 핵의 자화 방향을 나타내며 $+1$ 은 위, -1 은 아래로의 핵 자화 방향을 나타낸다. 또한 수직 직류자기장을 동시에 인가할 경우 실제 정보 저장장치로의 응용에 중요한 요소인 핵 자화 반전속도 및 임계 자기장 세기를 보다 효율적으로 조절할 수 있음을 확인하였다.

마지막으로 기존의 2 차원 구조체가 아닌 3 차원 반구 형태에 형성된 자기소용돌이 핵 자화 반전을 연구하였다. 그 결과 독특한 3 차원 구조에 의하여 기존 2 차원 구조체에서의 핵 자화 반전에서 볼 수 없었던

새로운 핵 자화 반전 메커니즘을 확인하였다. 또한 이 경우 핵 자화 뿐만 아니라 자기소용돌이의 회전도도 동시에 반전시킬 수 있음을 확인하였다.

본 연구는 단순히 자기소용돌이 핵 자화 반전의 효율적인 방법 및 그 원리를 제공할 뿐만 아니라 실제 자기소용돌이 기반 정보 저장장치 개발에 필요한 중요한 밑거름을 제시한다는 데 그 의의가 있다 하겠다.